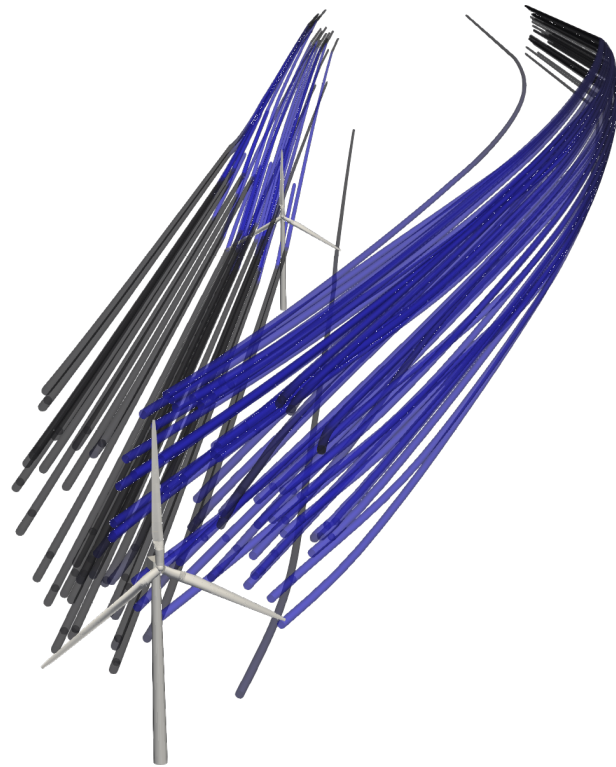




CHALMERS



Neural Network-Guided Active Yaw Control in a Two-Turbine Wind Farm

Master's thesis in Applied Mechanics

VIKTOR ALATALO

MASTER'S THESIS IN APPLIED MECHANICS

Neural Network-Guided Active Yaw Control in a Two-Turbine Wind Farm

VIKTOR ALATALO

Department of Mechanics and Maritime Sciences
Division of Fluid Dynamics
CHALMERS UNIVERSITY OF TECHNOLOGY
Göteborg, Sweden 2022

Neural Network-Guided Active Yaw Control in a Two-Turbine Wind Farm
VIKTOR ALATALO

© VIKTOR ALATALO, 2022

Master's thesis 2022:58
Department of Mechanics and Maritime Sciences
Division of Fluid Dynamics
Chalmers University of Technology
SE-412 96 Göteborg
Sweden
Telephone: +46 (0)31-772 1000

Cover:
Streamlines for the mean velocity magnitude in the wake of a turbine in yaw

Chalmers Reproservice
Göteborg, Sweden 2022

Neural Network-Guided Active Yaw Control in a Two-Turbine Wind Farm
Master's thesis in Applied Mechanics
VIKTOR ALATALO
Department of Mechanics and Maritime Sciences
Division of Fluid Dynamics
Chalmers University of Technology

ABSTRACT

To optimize the power production of wind farms, the wakes can be manipulated and their adverse effects mitigated. A promising wake deflection method is yaw misalignment. By deflecting the wake away from downwind turbines, the yaw-based approach seeks to increase the collective power production of the grouped wind turbines by sacrificing some power output of the upwind turbine in yaw. Using an artificial neural network (ANN), specifically a feedforward neural network, this work aims to develop an active yaw control (AYC) scheme for a two-turbine wind farm. To aid in the development of the AYC, FAST.Farm is utilized, which is a newly developed midfidelity tool by the National Renewable Energy Laboratory (NREL). FAST.Farm is calibrated by comparing several of its predicted wake properties to results of a Large-Eddy Simulation (LES) for which a 1D actuator disk method is used. Subsequently, with the purpose of gathering data to train an ANN, the wind farm is simulated in a multitude of operating conditions. Specifically, the operating conditions are combinations of various turbulence intensities, wind shear exponents, and yaw angles for the upwind turbine. The ANN is then used to predict total power production in the wind farm, which informs the decisions of the AYC. It is shown that, when the turbulence intensity (TI) is low (5 %), the AYC increases wind farm power production by 5-6 %, depending on the wind shear exponent (a smaller wind shear exponent yields a larger gain in power production). As the TI increases, the gain in power production goes to zero. Moreover, it is shown that the AYC increases the structural loads (up to 20 %) on both the upwind turbine and downwind turbine with respect to the blade root out-of-plane bending moment and tower base fore-aft moment. With respect to the yaw bearing moment, the AYC greatly increases it for the upwind turbine (up to 7 times) and slightly lowers it for the downwind turbine (roughly 5 %).

Keywords: FAST.Farm, wind farm, LES, active yaw control, wake steering, artificial neural network

ACKNOWLEDGEMENTS

First and foremost, I would like to express a great gratitude towards my supervisor, Dr. Hamidreza Abedi, who have always been available for discussing the project and any issue thereof I would run into. He has been fully supportive, encouraging and engaged throughout the project. Further, I wholly appreciate the discussions with Professor Sebastien Gros of NTNU and Associate Professor Morteza Haghiri Chehreghani of Chalmers who gave me guiding insights to wind farm control theory and artificial neural networks, respectively. I must thank Dr. Jason Jonkman of NREL, who provided crucial help online for me to overcome a number of obstacles in the process of learning FAST.Farm and its associated software. Finally, I wish to thank my friends and family who have encouraged me during my years as a student of physics.

NOMENCLATURE

Abbreviations

ABL	Atmospheric Boundary Layer
ADM	Actuator Disc Model
ANN	Artificial Neural Network
AYC	Active Yaw Control
BEM	Blade Element Momentum theory
BNN	Biological Neural Network
CFD	Computational Fluid Dynamics
DEL	Damage Equivalent Load
DNS	Direct Numerical Simulation
DWM	Dynamic Wake Meandering
FAST	Fatigue, Aerodynamics, Structures and Turbulence
FFNN	Feedforward Neural Network
HAWT	Horizontal Axis Wind Turbine
LES	Large-Eddy Simulation
MSE	Mean Squared Error
NREL	National Renewable Energy Laboratory
SGS	Subgrid-Scale
TI	Turbulence Intensity
TKE	Turbulent Kinetic Energy

Greek letters

α	Wind shear exponent, angle of attack
β	Pitch angle
δV_r	Radial velocity deficit
δV_x	Axial velocity deficit
Δ	Spatial filter width
δ	Wake width
Δ_{sim}	Calibration error
δ_{ij}	Kronecker's delta
ℓ	Layer index
ϵ	Dissipation rate of turbulent kinetic energy
Γ	Lapse rate
γ	Yaw misalignment angle, adiabatic index
Γ_a	Adiabatic lapse rate
κ	Eddy wavenumber
Λ_K	Turbulence scale parameter of velocity component K
μ_{wake}	Mean radial wake displacement
ν	Kinematic viscosity

ν_{SGS}	Subgrid-scale eddy viscosity
ν_t	Eddy viscosity
Ω	Rotational blade speed
ω	Rotational blade angle
Φ	Flow angle
ϕ	Wake skew angle, arbitrary quantity
ρ	Density
ρ_θ	Potential density
σ_{wake}	Standard deviation of radial wake displacement
σ_K	Standard deviation of velocity component K
τ_{ij}	Subgrid stress tensor component
θ	Potential temperature, azimuthal angle

Other symbols

$'$	Fluctuating quantity
$\bar{\cdot}$	Spatially filtered quantity
$\langle \cdot \rangle$	Temporally averaged quantity

Roman letters

\dot{m}	Mass flow rate
a'	Tangential induction factor
A	Area
a	Axial induction factor, activation output, recursion coefficient
b	Neural network bias, recursion coefficient
B_{uu}^t	Streamwise autocorrelation
C	Cost function
c	Chord length
c_{meander}	FAST.Farm wake parameter
C_S	Smagorinsky constant
C_D	Drag coefficient
C_L	Lift coefficient
C_P	Power coefficient
c_p	Constant pressure specific heat capacity
C_T	Thrust coefficient
c_v	Constant volume specific heat capacity
D	Rotor diameter
E	Spectral energy, AYC threshold parameter
f	Eddy frequency, probability density function
f^{eq}	Damage equivalent load equivalent frequency
f_c	Cutoff frequency
F_D	Drag force
F_L	Lift force
F_n	Axial force
f_V, f_G, f_B	Wake tracking functions
G	Convolution kernel

g	Activation function
k	Turbulent kinetic energy, wake growth rate parameter
L_{int}	Integral length scale
L_K	Turbulent length scale of velocity component K
m	Wöhler coefficient, wake plane index
MOD_{meander}	FAST.Farm wake parameter
n	Fourier node number, radial node index, sample index
P	Wind turbine power output
p	Pressure
r	Radius
S_K	Velocity power spectrum of velocity component K
s_{ij}	Strain-rate tensor component
T	Temperature, elapsed time
T_{int}	Integral time scale
u, v, w	Streamwise, lateral and vertical velocity components
u_{ω}	Blade tangential velocity component
u_{τ}	Rotor plane-lateral velocity component
u_{bulk}	Bulk streamwise velocity
u_{ref}	Reference streamwise velocity
U_{rel}	Relative velocity
u_i	Velocity component in the i :th direction
u_n	Rotor plane-normal velocity component
w	Neural network weight
w_n	Wake plane weight
x, y, z	Streamwise, lateral, and vertical coordinate components
$x_{\text{wake}}, y_{\text{wake}}, z_{\text{wake}}$	Wake centre coordinate components
x_i	Coordinate component in the i :th direction
z_{ref}	Reference height
Vectors	
$\hat{x}, \hat{r}, \hat{\theta}$	Cylindrical unit vectors
$\hat{x}, \hat{y}, \hat{z}$	Cartesian unit vectors
\hat{y}	Output vector
r	Location vector
v	Velocity vector
\mathbf{V}^{Dist}	Disturbed wind field
$\mathbf{V}^{\text{Plane}}$	Wake plane field
v_{∞}	Free stream velocity vector
x	Input vector, location vector
y	Desired output vector
δv	Velocity deficit vector

CONTENTS

Abstract	i
Acknowledgements	i
Nomenclature	iii
Contents	vii
1 Introduction	1
1.1 Literature review	1
1.2 Aim	2
1.3 Limitations	2
2 Theory	4
2.1 Atmospheric Boundary Layer	4
2.1.1 Atmospheric Stability	5
2.2 Computational Fluid Dynamics	5
2.2.1 Governing Equations	6
2.2.2 Large-Eddy Simulations	6
2.2.3 Synthetic Turbulence	8
2.3 Wind Turbine Modelling	9
2.3.1 Actuator Disc Model	9
2.3.2 Blade Element Momentum Theory	9
2.3.3 Damage Equivalent Load	11
2.3.4 Reference Wind Turbine	11
2.4 Wake Dynamics	12
2.4.1 Wake Regions	12
2.4.2 Wake-Turbulence Interaction	13
2.4.3 Wake Deflection	13
2.5 FAST.Farm	14
2.5.1 Wake Dynamics Modelling	15
2.6 Artificial Neural Networks	17
2.6.1 Feedforward Neural Network	18
2.6.2 Backpropagation	18
3 Method	20
3.1 FAST.Farm Computational Domain	20
3.2 TurbSim	21
3.3 Calibration	21
3.3.1 Wake Quantities	22
3.3.2 Wake Tracking Methods	23
3.3.3 Radial Dependence of Velocity Deficits	24
3.4 Artificial Neural Network	25
3.4.1 FAST.Farm Simulations	26
3.4.2 Hyperparameters Grid Search	26
3.5 Active Yaw Control	27
3.5.1 Control Algorithm	27
3.5.2 Low-Pass Filter	27

4 Results	29
4.1 Calibration	29
4.1.1 Wake Tracking Methods	29
4.1.2 Calibration Error and Optimal Parameters	29
4.1.3 Thrust and Torque Comparisons	30
4.1.4 Evolution of Wake Quantities	31
4.2 Steady Uniform Inflow	32
4.3 Artificial Neural Network	33
4.3.1 Structural loads	33
4.3.2 Wind Farm Power Production	35
4.3.3 Optimal Yaw Misalignments	36
4.4 Active Yaw Control	37
4.4.1 Trained Wind Conditions	37
4.4.2 Untrained Wind Conditions	41
4.5 Error Analysis	42
5 Conclusions	43
6 Future work	44
References	45
A Figures and Tables	49
A.1 Method	49
A.1.1 Wake Tracking	49
A.1.2 Low-Pass Filter	49
A.2 Results	50
A.2.1 Calibration	50
A.2.2 Turbulent Length and Time Scales	51
A.2.3 Hyperparameter Grid Search	51
A.2.4 Training and Validation Process	52
A.2.5 Neural Network Power Predictions	53
A.2.6 Structural Loads	53
A.2.7 Wind Shear Exponent and Bulk Velocity	55
B Mathematical Derivations	56
B.1 Atmospheric Stability	56
B.2 Betz' Limit	57
C Ethical considerations	58

1 Introduction

Fossil energy has been paramount to societal prosperity since the dawn of the industrial age [1]. However, due to climate change, which is largely driven by the greenhouse gas emissions associated with the use of fossil fuels, it is clear that a desired level of prosperity can not be sustained with fossil energy for long without large scale environmental degradation [2, 3]. To escape the self-reinforcing fossil fuel dependency of the modern world [4], countries are taking measures to transition to more sustainable energy systems. To reach its national climate goal of net-zero greenhouse gas emission, Sweden is expected to increase its electrical power production by at least 70 % by 2040 [5]. To meet this large demand for electrical energy, wind power is expected to play a crucial role, owing to its low costs, low emissions, and short installation times.

It has been reported that the economically feasible potential of offshore wind power along the long coast of Sweden is 300 TWh of annual electricity production [6], which far exceeds the country's current electricity usage. However, should current economical constraints be overcome, the potential can be increased tenfold. To reduce the associated costs (such as for maintenance and deployment of the turbine and the accompanying electrical grid), wind turbines can be grouped together in so-called wind farms. However, a downside of grouping turbines together is the wake effect [7, 8]. The wake of an upwind turbine can adversely affect the generated power and the structural loads of downwind machines, due to the lower wind speed and intensified turbulence accompanied by the wake, respectively. The increase in structural loads decreases the expected lifetime of the wind turbines, thus costs are increased. Compared to onshore wind farms, the wake effect is more prominent for offshore wind farms, as the length scale for the wake recovery (where free stream conditions are retained) is larger [9].

The wake effect can be mitigated. By yawing an upwind turbine such that the normal of its rotor plane is horizontally misaligned with the mean wind direction, the wake can be deflected away from downwind turbines. This method of wake steering is considered a promising approach to wind farm performance optimization [10]. By sacrificing some performance of the individual upwind turbine in yaw, the collective power output of the grouped wind turbines can be maximized. The focus of this work lies in developing a yaw control protocol for a variety of wind farm operating conditions, with the purpose of maximizing wind farm power production.

1.1 Literature review

The study of wind turbine wakes dates back to the 1970s. Among the early work is that of Lissaman [11, 12] and Faxen [13]. In their work, two distinct wake regions are established, a near-wake region and a far-wake region. In these regions, different mechanisms dictate the wake evolution. In the near-wake region, the turbulence is chiefly generated by the shear layer and viscous effects of the rotor, which diffuses the initially uniform velocity deficit of the wake. In contrast, in the far-wake region, the growth and decay of the wake is governed, to a large degree, by ambient turbulence and the velocity deficit profile is roughly Gaussian.

In 1988, Ainslie [14] observed that the measured velocity deficit in the wakes did not match contemporary theoretical predictions, and he ascribed this discrepancy to something that is called wake meandering, which is the chaotic motion of the wake due to the variability of the ambient wind. He developed an eddy viscosity model for the waked velocity field in the far-wake region, and thus successfully corrected for the wake meandering.

In 2003, Vermeer et al. [15] conducted a large meta study of the wind turbine wake research. The then-current understanding of the near- and far-wake regions was mapped extensively. The study ended by noting that the wake meandering was not yet satisfactorily modelled. In 2008, this was addressed by Larsen et al. [16], who developed a Dynamic Wake Meandering (DWM) model. The underlying assumption of the model was that the wake is advected passively by turbulent eddies larger than two rotor diameters and diffused by the smaller eddies. Since then, many other wake models have been developed [8], and there is a strong agreement within the wind energy community that large scale eddies govern the meandering phenomenon [17].

There have been numerous studies exploring the wake effect. Churchfield et al. [9] showed that unstable ambient conditions and high surface roughnesses are beneficial for the power output of wind farms. Moreover, Barthelmie et al. [18, 19] quantified the power losses and turbulence increases in a wind farm from field measurement. They found that, for an offshore wind farm near Copenhagen, the wakes caused power losses of approximately 10 %. There is also early research demonstrating the increases structural loads for wind turbines operating in wakes, e.g. by Volund [20].

Medici and Alfredsson [21] are probably the first to explore the potential of wake steering by yaw misalignment. In 2005, they conducted wind tunnel experiments and found that the wake can be deflected by yawing a turbine. Following their work, the wake of yawed turbines was researched further [7, 22–25]. It has been shown that the

shape of the wake changes due to yawing [26–29], and atmospheric conditions have been observed to influence the deflection of the wake. In unstable conditions, the wake is difficult to control [8, 30], due to the exaggerated wake meandering. However, this problem is less pronounced in more stable conditions, thus the prospects of increasing wind farm performance by wake steering lead to suggestions for optimal yaw configurations. Using a high fidelity solver, Fleming et al. [10] found that, for two turbines in a row, putting the upwind turbine in a misaligned yaw can increase the power production of the wind farm by several percentages. Numerous subsequent work [31–37] gave results which support the numerical findings of Fleming et al. [10]. Owing to the growing knowledge in yaw-based control schemes, the traditional “greedy” approach of optimizing wind farms with respect solely to individual wind turbine performance is challenged as the optimal wind farm control scheme [34]. In contrast, with active yaw control (AYC), wind farms can be optimized in a holistic approach. By now, there are a multitude of proposed yaw control algorithms, see e.g. [38–40]. Of special interest to this work is an algorithm developed by Gebraad et al. [41], which finds optimal yaw misalignments by utilizing a parametric model to predict power output of a wind farm. A similar algorithm is deployed for this work, but the parametric model is swapped for an artificial neural network.

In 2021, the National Renewable Energy Laboratory (NREL) released the FAST.Farm tool, which is a mid-fidelity tool for estimating the power performance and structural loads in wind farms. It was developed to facilitate wind farm design [42]. It features a DWM model which extends and addresses shortcomings of previous models. Moreover, it features a super controller module which allows for the development of e.g. active yaw control schemes. The performance of FAST.Farm has been explored in previous studies [43, 44]. Of special note are two studies by Shaler et al. [45] and Doubrawa et al. [46] in which a discretization sensitivity study was conducted and the process of calibrating FAST.Farm is explained, respectively.

The novelty of this work lies in utilizing FAST.Farm to generate data for training an artificial neural (ANN) network which, in turn, can inform the decisions of an AYC scheme. This approach is made feasible by the development of computationally cheap tools such as FAST.Farm, which facilitates the simulation of a great number of wind farm operating conditions.

1.2 Aim

This thesis aims to draw conclusions about how the yaw of the wind turbines should be controlled for a given wind farm in a multitude of operating conditions. By utilizing the software FAST.Farm, the power performance and fatigue loading on the wind turbines will be analysed in cases with and without an Active Yaw Control (AYC) protocol. Machine learning will be employed to develop the AYC. The main objective of this thesis is to investigate how to actively control the yaw of individual wind turbines, within wind farms, such that the overall power of the wind farm is maximized.

For this work, a number of issues are to be resolved, which include:

- Calibrate the FAST.Farm tool. FAST.Farm have numerous wake dynamics parameters which should be tuned using a high-fidelity simulation.
- Understand and implement an active yaw control model within FAST.Farm. This is done in the following steps:
 - For a single wind turbine, implement the control strategy.
 - Examine the developed active yaw control model for a two-turbine wind farm.
- Utilize machine learning to further develop the AYC. Specifically, use a Feed-forward Neural Network (FFNN) which can predict the wind farm power output in different operating conditions.

1.3 Limitations

This work is made under a set of limitations which include:

- The simulated wind farm is restricted to two turbines, seven rotor diameters (882 m) apart from each other. The two turbines are lined up with the mean wind direction.
- The simulated operating conditions of the wind farm are restricted to combinations of the yaw misalignment angle of the upwind turbine (γ_1), the ambient turbulence intensity (TI) and the wind shear exponent (α).

- The AYC is developed to predict optimal yaw misalignments only for the upwind turbine.
- To simulate the various operating conditions of the wind farm, no other tool than FAST.Farm is utilized. As an exception, a single Large-Eddy Simulation (LES) is conducted in STAR-CCM+ (a computational fluid dynamics solver) for the purpose of calibration.
- For developing the AYC, only unsteady, turbulent inflow is considered.
- NREL's TurbSim [47] is utilized exclusively for generating synthetic wind.
- Only horizontal axis wind turbines are studied.
- The NREL reference 5 MW wind turbine [48] is used in all simulations.
- The yaw misalignment may not exceed $\pm 30^\circ$ with respect to the mean wind direction.
- No other mean wind speed than 8 m s^{-1} is simulated.
- The simulation time with FAST.Farm will not exceed 40 minutes because of existing computational resources.
- Only the neutral atmospheric boundary layer is considered as the dominant atmospheric stratification during the day.

2 Theory

In the following section, relevant theory for this work is presented. The topics at hand include the atmospheric boundary layer, computational fluid dynamics, wind turbine modelling, wake dynamics, FAST.Farm, and artificial neural networks.

2.1 Atmospheric Boundary Layer

The troposphere, which extends to roughly 11 km above the surface of Earth [49], can be decomposed into different sections, as illustrated in Fig. 2.1. At the bottom of the troposphere resides the Atmospheric Boundary Layer (ABL), in which the flow is turbulent and is influenced by the heating, cooling and geometry of Earth's surface [50]. The ABL thickness can vary dramatically depending on location and time. It is common that the ABL occupies around 10-20 % of the troposphere, but it can range from tens of meters to 4 km [49], depending on stability, which is discussed in Section 2.1.1. Above the ABL, there is a region unaffected by turbulence, which is known as the free atmosphere. Between the ABL and the free atmosphere there is a transition region, which features a so-called capping inversion, as shown in Fig. 2.1. As opposed to a boundary layer above a flat plate which grows proportionally to the square root of downstream distance, the ABL thickness is constrained by the height of the capping inversion [50]. The capping inversion is characterized by a positive temperature gradient. Turbulent motion is inhibited above the capping inversion due to buoyant effects; upwards moving cold air is quickly pushed down again. This effectively traps turbulence within the ABL, and also gives an upper bound on the turbulent eddy length scales within an ABL, which do not exceed the ABL thickness. The eddy length scales which affect wind turbine and farm performance can range from the Kolmogorov scale (order of millimetres) to the ABL integral length scale (order of kilometres). In simulations and modelling, it is challenging to account for this large range of scales [17].

The atmospheric boundary layer can be decomposed into three vertical layers, as shown in Fig. 2.1. Closest to the surface of Earth is the laminar bottom layer, which have a characteristic length called the roughness length (z_0) which can vary between a millimetre to several meters depending on the type of terrain [50, 51]. For instance, the open sea have a very low roughness length, while cities or sparse forests typically have higher roughness lengths. Above the laminar layer is the Prandtl layer (or surface layer) and it usually occupies 5 to 10 % of the ABL [49]. This region is characterized by large gradients. There is a wind velocity gradient because of the no-slip condition at the surface. The evaporation and heat flux from surface-to-air can also give rise to significant humidity and temperature gradients. Moreover, the turbulence is fully developed in the Prandtl layer. The Ekman layer constitutes the topmost and occupies the largest share of the ABL. In it, the Coriolis effect becomes significant, which modulates the wind [17, 52].

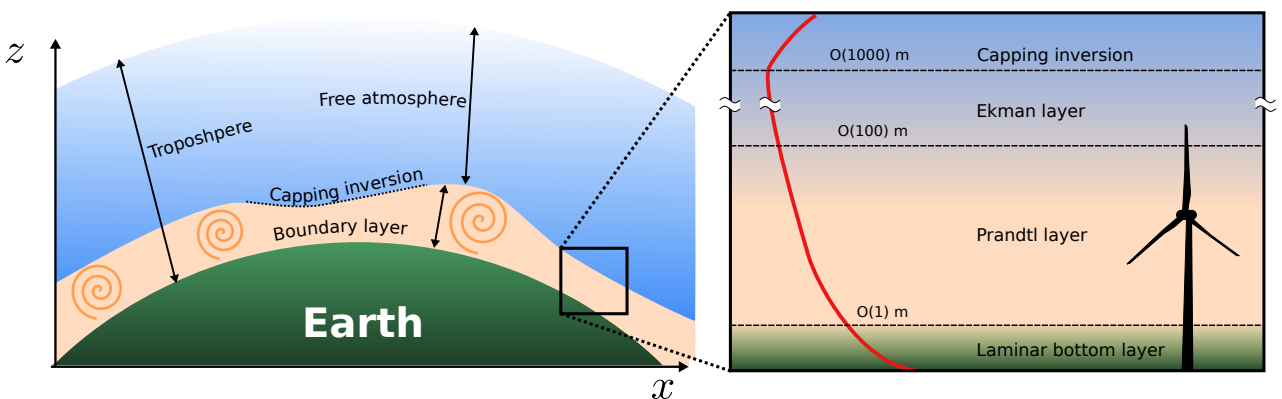


Figure 2.1: Schematic representation of the troposphere (left) and its different regions. Turbulent eddies are indicated by swirls. The three bottommost regions, which together constitute the atmospheric boundary layer, are shown to the right. The (—) graph is a typical temperature profile in the ABL during daytime. Figure inspired by Stull [50].

2.1.1 Atmospheric Stability

As has been mentioned, the length scales of the ABL can vary greatly depending on its stability, which can be described as the tendency of fluid elements to resist turbulent vertical motion [53]. The ABL can be either unstable, stable or neutral. As rules of thumb, unstable conditions are associated with sunny days when the ground is hotter than the air above it, or when cold air advects over warm surfaces [50]. In unstable conditions, turbulence is enhanced and the ABL is thick. Stable conditions are characterized by the ground being cooler than the air, and are typically achieved during night or in light winds. In stable conditions, turbulence is suppressed and the ABL is shallow (20-500 m). In neutral stability, the heat flux from the surface is negligible, and shear forces dominate [52]. Medium to strong winds are typical of a neutrally stable ABL [50]. The reason the stability of the ABL changes throughout the day is due to diurnal cycle of solar heating.

The stability of an ABL can be defined mathematically. The potential temperature (θ) denotes the temperature attained by a fluid element brought adiabatically to a standard pressure (p_0). The derivative of θ with respect to the height (z) can be expressed as [54]:

$$\frac{T}{\theta} \frac{d\theta}{dz} = \Gamma - \Gamma_a, \quad (2.1)$$

where T , Γ , and Γ_a denotes the temperature, lapse rate and adiabatic lapse rate, respectively. The adiabatic lapse rate is the rate at which temperature can decrease in an isentropic atmosphere without causing instability, and is typically $-10^\circ\text{C km}^{-1}$ in Earth's atmosphere [54]. Hence, the ABL is stable, unstable, or neutrally stable if the gradient of θ is positive, negative, or zero, respectively. Another useful property is the potential density (ρ_θ) which is the density attained by a fluid element brought isentropically to p_0 . Its derivative with respect to height is

$$-\frac{1}{\rho_\theta} \frac{d\rho_\theta}{dz} = \frac{1}{\theta} \frac{d\theta}{dz} = \frac{\Gamma - \Gamma_a}{T}, \quad (2.2)$$

where Eq. (2.1) was used in a step of the derivation. By the same logic as for the potential temperature, it is understood that the ABL is stable, unstable, or neutrally stable if $d\rho_\theta/dz$ is negative, positive or zero, respectively. For full derivations of Eqs. (2.1) and (2.2), see Section B.1.

By studying a fluid element, Eq. (2.2) can help explain why turbulence is attenuated or amplified, depending on the atmospheric stability. In stable conditions, if the fluid element is isentropically displaced upwards, before reaching equilibrium, it is surrounded by other fluid elements more dense than it. Buoyant forces thus push it downwards to its original position. This suppresses turbulent motion. In contrast, for unstable conditions, any upward displacement is amplified by a lifting buoyant force. This enhances turbulent motion. In neutrally stable conditions, buoyancy neither attenuates nor amplifies turbulent motion [54, 55].

Depending on the atmospheric stability and the surface roughness length (z_0) the wind profile in the surface layer is typically sheared to various degrees [52], as shown in Fig. 2.2. In stable conditions, the wind profile is notably sheared over a large distance above ground. In contrast, in unstable conditions, the wind profile is quite sheared close to the ground, but is almost uniform at greater heights. A quantity which can be used to describe the shear (at least locally within the Prandtl layer) is the shear exponent (α), which is used in the empirical power law defined as

$$u(z) = u_{\text{ref}} \left(\frac{z}{z_{\text{ref}}} \right)^\alpha, \quad (2.3)$$

where u is the streamwise velocity component. The subscript ref refers to a reference height, e.g. the hub height of a wind turbine.

2.2 Computational Fluid Dynamics

Constitutive assumptions (for viscous forces and heat conduction) together with conservation principles for mass, energy and momentum yields equations which can be solved to predict fluid flow [54]. However, in most cases, the complexity of such equations renders analytical solutions difficult to obtain. In fact, gaining further understanding of the Navier-Stokes equations (which govern continuum fluid motion) is one of the Millennium Problems selected by the Clay Mathematics Institute [56], which include six important unsolved problems in mathematics, spanning a wide range of topics. To cope with the absence of analytical solutions, the field of Computational Fluid Dynamics (CFD) emerged in the late 1950s [54], thanks to the development of computers. CFD is the method of finding numerical solutions to the equations which govern fluid flow. Today, CFD is an

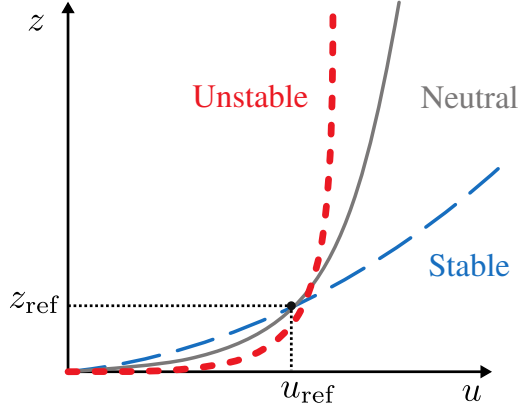


Figure 2.2: Typical wind profiles in different atmospheric stabilities. Figure modified from [52].

integral tool for analysis and design processes involving fluid flows, heat transfer and turbulence. It is utilized in a variety of industries, including the biomedical, automotive, aerospace, and HVAC industries.

2.2.1 Governing Equations

The flow in an atmospheric boundary layer is governed, in part, by the Navier-Stokes equations, which express the conservation of momentum for a Newtonian fluid [55]. For a neutrally stable ABL, as is studied in this work, the energy equation can be omitted from the governing equations, because the energy transfer is assumed to be negligible. Moreover, wind speeds within the ABL are typically low enough to treat the flow as incompressible. For an incompressible flow with constant viscosity, the Navier-Stokes equations are given as

$$\frac{\partial u_i}{\partial t} + \frac{\partial u_j u_i}{\partial x_j} = -\frac{1}{\rho} \frac{\partial p}{\partial x_i} + \nu \left(\frac{\partial^2 u_i}{\partial x_j^2} \right) + f_i, \quad (2.4)$$

where u_i , x_i , ν , p , ρ , and f_i denotes the velocity, the spatial coordinate, the kinematic viscosity, the pressure, the density, and an external force, respectively. The external force acting on the fluid element can be e.g. gravity. The Navier-Stokes equations are coupled with the continuity equation, which states that mass is conserved. For an incompressible flow, it is defined as

$$\frac{\partial u_i}{\partial x_i} = 0. \quad (2.5)$$

2.2.2 Large-Eddy Simulations

In a Direct Numerical Simulation (DNS), the Navier-Stokes equations are solved for the instantaneous field at all temporal and spatial scales. DNS is often prohibitive expensive in terms of computational resources. For wind farms, the range of scales needed to be resolved is too large for DNS to be a feasible approach. Instead, to reduce computational requirements and still yield accurate results, a Large-Eddy Simulation (LES) can be viable an option.

In CFD, a common approach to solve the Navier-Stokes equations is by decomposing quantities in two parts, an averaged part and a fluctuating part. In LES, the field quantities are filtered such that the effect of the large eddies is resolved, and the effect of the smaller eddies is modelled [15, 55]. Generally, small eddies behave isotropically, in contrast to large eddies, which behave anisotropically. Hence, smaller eddies are easier to model.

A spatially filtered quantity can be expressed as the convolution of the quantity multiplied with a filter convolution kernel (G) [55]. Mathematically, the filtered quantity is found as

$$\bar{\phi}(\mathbf{x}) = \int_{-\infty}^{\infty} G(\mathbf{x} - \mathbf{r}) \phi(\mathbf{r}) \, d\mathbf{r}, \quad (2.6)$$

where $\phi = \bar{\phi} + \phi'$ for which the bar and the prime denote a spatially filtered part and a subfiltered part, respectively. \mathbf{x} and \mathbf{r} are location vectors. In finite volume methods, a box filter is always utilized [55], for

which the convolution kernel (G) have the following properties:

$$G(\mathbf{r}) = \begin{cases} \frac{1}{\Delta}, & |\mathbf{r}| \leq \frac{\Delta}{2} \\ 0, & |\mathbf{r}| > \frac{\Delta}{2} \end{cases}, \quad (2.7)$$

where Δ is the box side length. With the box filter, the filtered quantity is simply a cell volume average, and the subfiltered quantity is a subgrid-scale (SGS) part which corresponds to eddies of length scales smaller than the box.

The eddy wavenumber (κ) is inversely proportional to the eddy length scale. Eddies of wavenumbers higher than the cutoff wavenumber $\kappa_c = \pi/\Delta$ are modelled, while eddies with smaller wavenumbers are resolved. Hence the LES can be understood as a way of low-pass filtering the Navier-Stokes equations. In Fig. 2.3 the spectrum of turbulent kinetic energy is shown, where the area under the graph corresponds to the turbulent kinetic energy (k). In the figure, three regions are indicated as I, II, and III. Region I contains large anisotropic eddies which carry a large share of the energy, and they extract kinetic energy from the mean flow. In region II, called the inertial subrange, energy is transported from larger eddies to smaller eddies in a process called the energy cascade. In this region, the eddies are isotropic. The dissipation subrange, region III, contains small isotropic eddies. These eddies are largely responsible for the dissipation of turbulent kinetic energy (TKE), such that TKE is converted to thermal energy at a rate of dissipation (ϵ) [55].

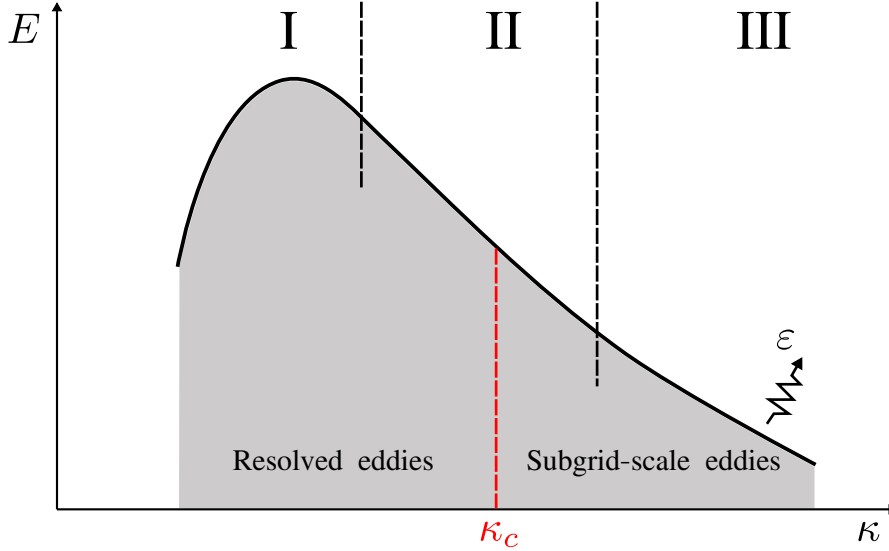


Figure 2.3: The spectral energy (E) as a function of wavenumber (κ). The area under the curve corresponds to the turbulent kinetic energy (k) of the flow. Figure inspired by [55].

By filtering the incompressible Navier-Stokes equations, the corresponding equations which are solved for in LES are given as [55]:

$$\frac{\partial \bar{u}_i}{\partial x_i} = 0, \quad (2.8)$$

and

$$\frac{\partial \bar{u}_i}{\partial t} + \frac{\partial \bar{u}_j \bar{u}_i}{\partial x_j} = -\frac{1}{\rho} \frac{\partial \bar{p}}{\partial x_i} + \nu \frac{\partial^2 \bar{u}_i}{\partial x_j \partial x_j} - \frac{\partial \tau_{ij}}{\partial x_j}, \quad (2.9)$$

where Eqs. (2.8) and (2.9) express the conservation of mass and momentum, respectively. The subgrid stress tensor (τ_{ij}) is defined as

$$\tau_{ij} = \overline{u_i u_j} - \bar{u}_i \bar{u}_j, \quad (2.10)$$

and can be modelled, with e.g. the Smagorinsky SGS model, which is an eddy viscosity model, such that

$$\tau_{ij} - \frac{1}{3} \delta_{ij} \bar{\epsilon} = -\nu_{\text{SGS}} \left(\frac{\partial \bar{u}_i}{\partial x_j} + \frac{\partial \bar{u}_j}{\partial x_i} \right) = -2\nu_{\text{SGS}} \bar{s}_{ij}, \quad (2.11)$$

where δ_{ij} , ν_{SGS} and \bar{s}_{ij} is the Kronecker delta, the subgrid-scale eddy viscosity and the spatially filtered strain-rate tensor, respectively. Further, ν_{SGS} can be defined as

$$\nu_{\text{SGS}} = (C_S \Delta)^2 |\bar{s}_{ij}|, \quad (2.12)$$

where C_S is the Smagorinsky constant. It is a flow dependent coefficient, commonly on the order of 0.1.

2.2.3 Synthetic Turbulence

To generate turbulent flows or turbulent boundary conditions without restrictive computational costs, synthetic turbulence is an option to e.g. precursor large-eddy simulations. The main idea is to produce stochastic time series of velocity fields which share known characteristics of real turbulence, such as the slope of the curve in region II of the energy spectrum shown in Fig. 2.3. To do this, the velocity fluctuations (\mathbf{v}') are described in wavenumber space as Fourier series, such that [55]:

$$\mathbf{v}' = 2 \sum_{n=1}^N \hat{u}^n \cos(\boldsymbol{\kappa}^n \cdot \mathbf{x} + \psi^n) \boldsymbol{\sigma}^n, \quad (2.13)$$

where n , N , $\boldsymbol{\kappa}$, \mathbf{x} , ψ , $\boldsymbol{\sigma}$, \hat{u} is the Fourier node number, number of such nodes, the wavenumber vector, position vector, the phase angle, direction in wave number space, and amplitude respectively. The phase angles are generated randomly, while the amplitude is modelled as a function of frequency (f) or wavenumber (κ). There is a relation between wavenumber and frequency, defined mathematically as

$$f = \frac{2\pi}{\kappa}. \quad (2.14)$$

A model for the power spectrum of the velocity components is the IEC Kaimal model [47, 57], which is suitable for a neutrally stable ABL. For a velocity component $K = u, v, w$, the spectrum is defined as

$$S_K(f) = \frac{4\sigma_K^2 L_K / \langle u \rangle_{\text{hub}}}{(1 + 6f L_K / \langle u \rangle_{\text{hub}})^{5/3}}, \quad (2.15)$$

where $S(f)$, σ , $\langle u \rangle_{\text{hub}}$, denotes the spectrum, the standard deviation of the velocity component K , and the mean velocity at hub height ¹, respectively. L_K is an integral scale parameter, which is found as

$$L_k = \begin{cases} 8.1\Lambda_u, & K = u \\ 2.7\Lambda_u, & K = v \\ 0.66\Lambda_u, & K = w \end{cases}, \quad (2.16)$$

where Λ_u is a turbulence scale parameter defined as

$$\Lambda_u = 0.7 * \min(30 \text{ m}, z_{\text{hub}}), \quad (2.17)$$

where z_{hub} is the hub height. Lastly, the model produce anisotropic turbulence such that

$$\sigma_v = 0.8\sigma_u \quad (2.18)$$

$$\sigma_w = 0.5\sigma_u, \quad (2.19)$$

where σ_u denote the standard deviation of the streamwise velocity component.

By using synthetic turbulence, turbulent wind fields can be generated at low computational costs. By generating time series of synthetically turbulent wind in a plane, a full three-dimensional wind field can be constructed by propagating those planes with the mean wind. The underlying assumption of this approach is Taylor's frozen turbulence hypothesis, which states that turbulent properties (e.g. turbulent fluctuations of the velocity field) are transported by the mean flow [55]. The hypothesis holds better for low turbulence intensities. Turbulence intensity (TI) is a way of quantifying the level of turbulence in a flow and it is a central quantity for this work. Here, it is defined as

$$TI = \frac{\sigma_u}{\langle u \rangle}. \quad (2.20)$$

¹In this work, the notation for a temporally averaged quantity is $\langle \phi \rangle$, where ϕ is an arbitrary quantity.

2.3 Wind Turbine Modelling

The presence of a wind turbine affects the surrounding flow. Kinetic energy of the wind is extracted by the turbine and converted to rotational energy and subsequently to electrical power by a generator. Hence, the wind speed must decrease downstream of the turbine. In this section, methods to predict the power output, aerodynamic forces, and structural loads are presented. Specifically, the actuator disc model, the blade element momentum theory, the damage equivalent load and various properties of the reference wind turbine studied in this work are described.

2.3.1 Actuator Disc Model

The Actuator Disc Model (ADM) is a useful model for understanding the energy extraction process of Horizontal Axis Wind Turbines (HAWTs). The model treats the rotor of the HAWT as an infinitesimal thin disc. There are a number of assumptions accompanied by the model: the flow immersing the disc is incompressible; the flow is steady and uniform upwind of the disc; the disc exerts no torque on the flow; the flow can be contained in a stream tube [58]. Figure 2.4a show the actuator disc and its surrounding stream tube. In the figure, the far upwind and far downwind quantities are denoted by the subscripts ∞ and $-\infty$, respectively.

The mass flow rate is constant in the stream tube and is defined mathematically as

$$\dot{m} = \rho A_{\infty} u_{\infty} = \rho A_D u_D = \rho A_{-\infty} u_{-\infty}, \quad (2.21)$$

where A and u denotes the cross-section area and streamwise velocity, respectively. The D subscript relates to the disc. Because the disc extracts kinetic energy from the flow, the downwind streamwise velocity ($u_{-\infty}$) must be lower than its upwind counterpart (u_{∞}). Due to the constant mass flow rate and the decrease in u , the cross-section area of the stream tube must increase along the streamwise direction. Hence $A_{-\infty} > A_{\infty}$.

In Appendix B.2 the so-called Betz limit is derived using ADM theory. The power coefficient (C_P) is the ratio of extracted power (P) and available kinetic energy in the wind (P_0). Betz limit expresses a theoretical maximum of C_P , such that

$$C_P = P/P_0 = 4\bar{a}(1 - \bar{a})^2, \quad (2.22)$$

where \bar{a} is the axial induction factor, defined as

$$\bar{a} = (u_{\infty} - u_D)/u_{\infty}. \quad (2.23)$$

The power coefficient takes a maximum value of $C_{P,max} = 16/27$ when $\bar{a} = 1/3$ [58], which suggests that a wind turbine can not extract more than 59% of the kinetic power available in the wind.

The axial force exerted on the disc by the fluid (F_n) can be expressed as

$$F_n = A_D(p_D^+ - p_D^-) = \frac{1}{2}\rho A_D u_{\infty}^2 \bar{a}(1 - \bar{a}), \quad (2.24)$$

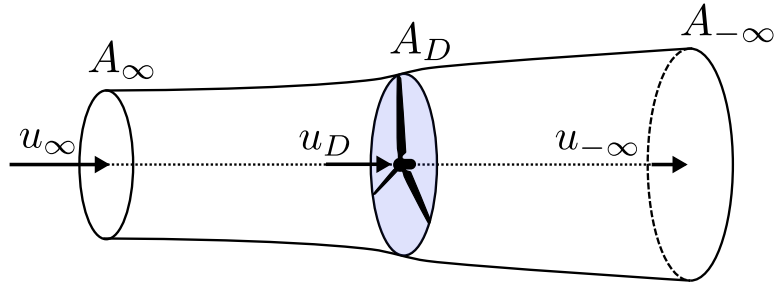
where p_D^{\pm} denote the pressure upwind and downwind of the disc, respectively, as seen in Fig. 2.4b. Similarly to the power coefficient, the thrust coefficient (C_T) can be defined as the ratio of axial force (F_n) exerted on the disc and the dynamic pressure at the disc (in unperturbed flow) [58]:

$$C_T = \frac{F_n}{1/2\rho A_D u_{\infty}^2} = 4\bar{a}(1 - \bar{a}), \quad (2.25)$$

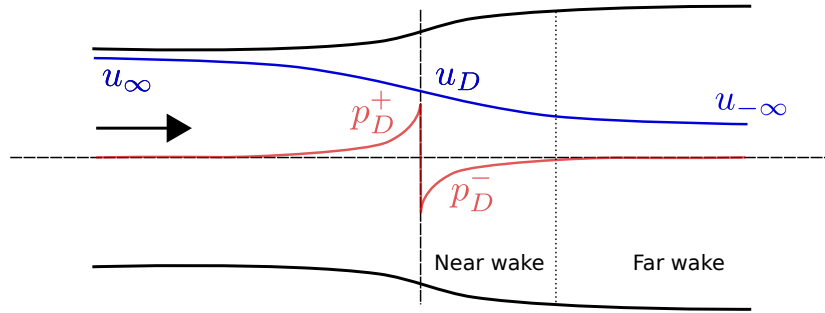
which has a maximum of unity at $\bar{a} = 1/2$, at which point the downwind velocity becomes zero, i.e. the flow is stopped completely downwind of the disc (as is understood from Eqs. (B.15) and (2.23)). For $\bar{a} < 1/2$, an increase in C_T decreases the downwind velocity ($u_{-\infty}$) thus the area $A_{-\infty}$ must increase, due to the conservation of mass. Hence, an increase in C_T expands the wake [15].

2.3.2 Blade Element Momentum Theory

The blade element theory is a method to derive expressions for the aerodynamic forces exerted on a radial blade element of infinitesimal radial length [59]. The blade element momentum theory (BEM) combines momentum theory (conservation of linear and angular momentum) and the blade element theory. It is a widely used method to analyse wind turbine rotor behaviour and rotor design [53]. For instance, it is used in one of



(a) A stream tube containing the actuator disc and the flow passing through it



(b) Qualitative velocity and pressure profiles along the stream tube. The pressure drops discontinuously across the disc, but recovers to ambient levels further downstream.

Figure 2.4: Associated velocity and pressure profiles of the actuator disc model (bottom), along with the encompassing stream tube (top)

FAST.Farm submodules, AeroDyn, which calculates the aerodynamic forces exerted on the rotor. For the ADM, it assumed that the wake is irrotational downwind of the rotor. This is not the case for the BEM, in which the torque exerted on the flow is accounted for. Moreover, for the BEM, the axial flow induction factor (a) varies with radial distance. For the ADM, it was taken as a mean value (\bar{a}) along the blade. Figure 2.5a illustrate the location of a blade element situated between r and $r + dr$ from the rotor centre. Figure 2.5b displays the relevant forces acting on that blade element. It can be shown that the lift and drag force are defined mathematically as

$$F_L = \frac{\rho c}{2} U_{\text{rel}}^2 C_L(\alpha) \quad (2.26)$$

$$F_D = \frac{\rho c}{2} U_{\text{rel}}^2 C_D(\alpha), \quad (2.27)$$

where c , α , U_{rel} , C_L , C_D is the chord length, angle of attack, flow velocity in the blade element's moving frame of reference, lift coefficient and drag coefficient, respectively.

The angle of attack can be found with trigonometry (see Fig. 2.5b) such that

$$\alpha = \Phi - \beta, \quad (2.28)$$

where β and Φ is the local blade pitch angle and the angle between the relative velocity direction and the blade element tangential direction, respectively. With velocity components directed as in Fig. 2.5b, the relative velocity is found as

$$U_{\text{rel}} = \sqrt{(u_\omega + \Omega r)^2 + u_n^2}, \quad (2.29)$$

where Ω , u_ω , and u_n is the rotational speed of the blade (such that $\Omega = \dot{\omega}$), the tangential and the rotor plane-normal flow velocity components, respectively. The blade element momentum theory revolves around

finding the blade forces through an iterative process of finding a correct pair of a and a' [58], where the latter is the tangential flow induction factor.

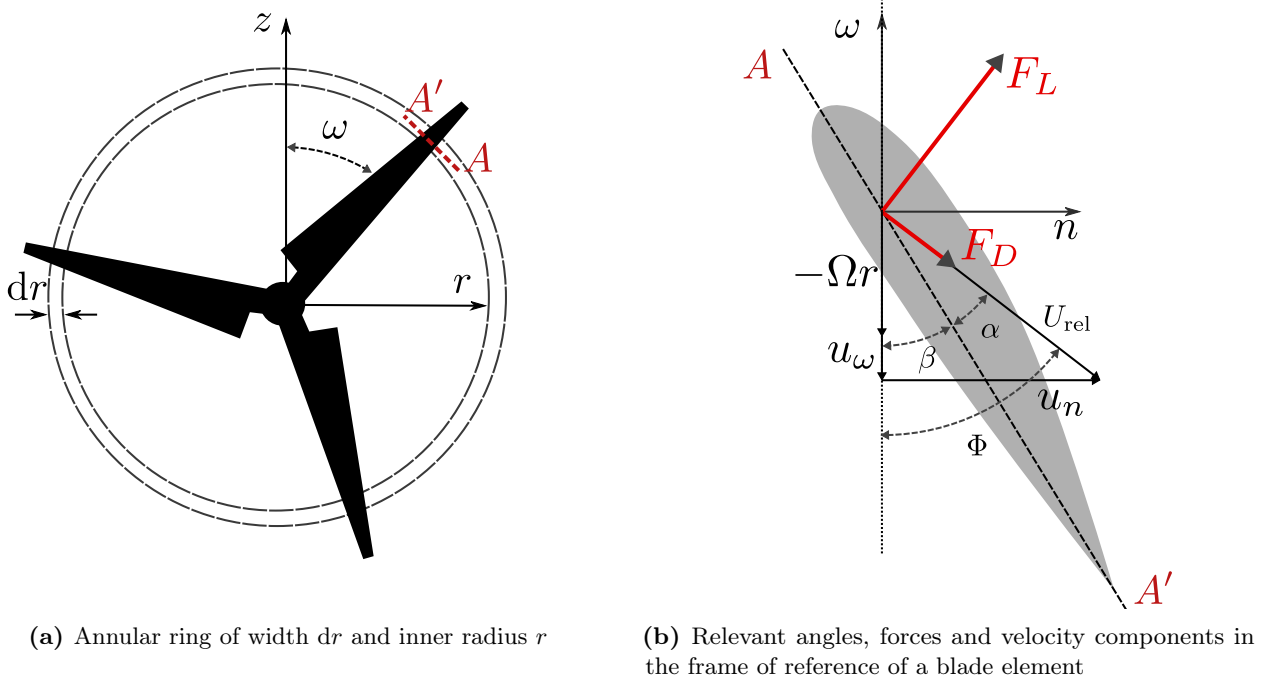


Figure 2.5: Schematic of the discretization of the rotor in the blade element theory with the annular ring (left), which comprises the rotor, and a corresponding blade element at radius r (right). Figure inspired by Kleusberg [60].

2.3.3 Damage Equivalent Load

A standard metric of fatigue damage is the short term damage equivalent load (DEL). It is defined mathematically as

$$\text{DEL} = \left(\frac{1}{T f^{\text{eq}}} \sum_{i=1} n_i (\Delta F_i)^m \right)^{(1/m)}, \quad (2.30)$$

where T , f^{eq} , and m denote the elapsed time of the load time series, the DEL equivalent frequency (e.g. the time series sampling frequency), and the Wöhler coefficient, respectively. n_i and ΔF_i refer to the number of load cycles and the corresponding load range, respectively [61]. Regarding the Wöhler coefficient, it is a material constant and is taken as $m = 3$ for the steel tower and the yaw bearing. For the composite material of the blades, it is taken as $m = 10$ [62]. The DEL represents the constant-amplitude sinusoidal load that produces the same fatigue damage as the original load sequence [40].

2.3.4 Reference Wind Turbine

For this work, only one type of wind turbine is studied, namely the reference wind turbine defined by National Renewable Laboratory (NREL). A few of its properties are defined in Tab. 2.1. The rated properties of the turbine are achieved in wind conditions for which the maximal generated power is achieved. The cut-in and cut-out wind speeds defines an interval within which the turbine can extract energy from the wind. The shaft tilt of the turbine means that its rotor plane meets the horizontal wind obliquely.

In Fig. 2.6 various steady state responses of the reference wind turbine are shown as functions of the wind speed. In a steady state, the generator torque increases quadratically until rated conditions are achieved, where it stagnates. To achieve a high energy extraction efficiency in Region 2, the tip speed is held constant while the rotor speed increases up to its rated speed. The blade pitch angle is controlled above rated, Region 3, as to keep the generator torque constant and limit the structural loads on the blades. For this work, the most relevant properties are those corresponding to a wind speed of 8 m s^{-1} .

Table 2.1: Properties of the NREL 5 MW reference wind turbine [48]

Rating	5 MW
Rotor orientation, configuration	Upwind, 3 blades
Control	Variable Speed, Collective Pitch
Rotor, Hub Diameter	126 m, 3 m
Hub Height	90 m
Cut-In, Rated, Cut-Out Wind Speed	3 m s^{-1} , 11.4 m s^{-1} , 25 m s^{-1}
Cut-In, Rated Rotor Speed	6.9 rpm, 12.1 rpm
Maximal Chord Length	4.7 m
Maximal Natural Frequency	2.9 Hz
Rated Tip Speed	80 m s^{-1}
Overhang, Shaft Tilt, Precone	5 m, 5° , 2.5°

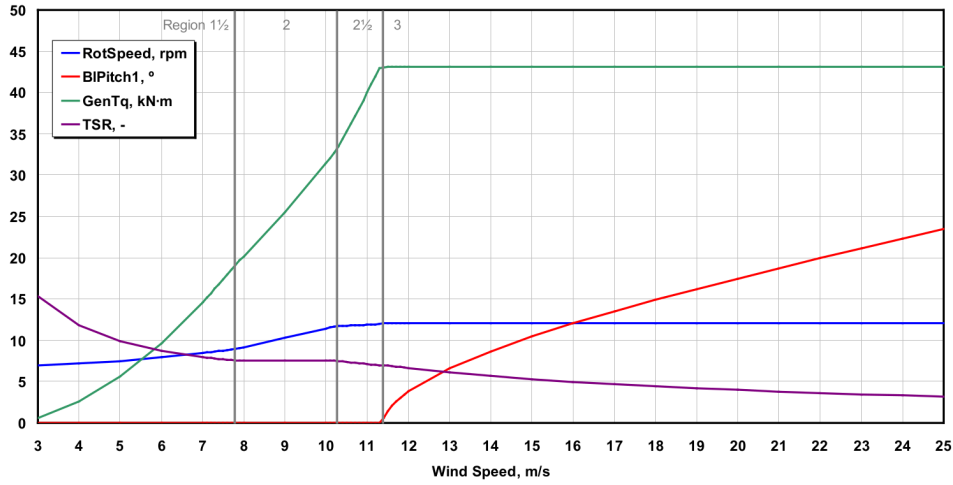


Figure 2.6: Steady state behaviour of NREL’s 5 MW reference wind turbine. Figure taken from [48].

2.4 Wake Dynamics

In the following section, some aspects of the relevant wake dynamics are covered, namely the wake regions, wake-turbulence interaction, and wake deflection.

2.4.1 Wake Regions

As mentioned in Section 1.1, the wind turbine wake can be divided into two distinct regions, namely the near- and far-wake region [17]. Their locations are marked schematically in Fig. 2.4b. The near-wake region typically stretches 2-4 rotor diameters downstream of the wind turbine, in which the wind turbine specific properties has a large impact on the complex flow behaviour. The near-wake is influenced by blade, nacelle and hub geometry [17], and large pressure gradients [14, 16]. In this region, the wake centreline velocity deficit reaches a minimum and the flow features helical vortex structures [17].

Downstream of the near-wake region is the far-wake region, in which the flow is less complex, where the pressure gradients have relaxed, and the wake profile is approximately Gaussian [14]. The flow characteristics in this region are not dictated by the specific wind turbine properties, rather general parameters such as the thrust and power coefficients and the inflow wind conditions are sufficient for predicting the far-wake region flow [17]. In most wind farms, the wind turbine spacing is 3 to 10 rotor diameters, meaning most wake effects are within the far-wake region. Thus, understanding the far-wake region is crucial for modelling and predicting the performance of waked turbines.

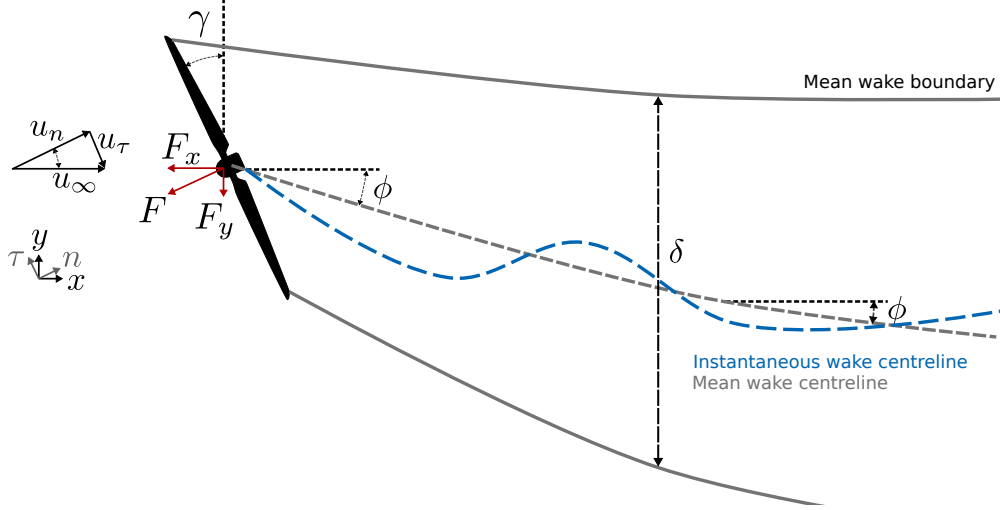


Figure 2.7: Forces and velocity components relevant for wake deflection caused by the turbine with a yaw misalignment angle (γ). The wake skew angle (ϕ) can be estimated at the rotor and in the far-wake region.

2.4.2 Wake-Turbulence Interaction

The turbulence in the ambient flow dictates much of the behaviour of the wake, e.g. how it moves, expands, and decays. There is an annular shear layer between the ambient flow and the wake. In the shear layer, turbulence is generated which, together with the ambient turbulence, diffuses and expands the wake [14, 16]. Moreover, the shear-generated turbulence interacts with the core of wake, influencing its velocity deficit and thus recovery to ambient wind conditions. At the wake centreline, in the far wake region, the velocity deficit decays monotonically and at a rate depending on the ambient turbulence intensity.

As opposed to in a typical wind tunnel, the atmospheric boundary layer features a wide range of turbulent eddy length scales. Because of this, the instantaneous wake centreline meanders, as shown in Fig. 2.7. This is said to be due to the large scale eddies. Larsen et al. [16] modelled the wake meandering phenomenon as a velocity deficit being advected by the mean wind and displaced in a plane perpendicular to the mean wind direction by the large eddies. The length scales of the eddies responsible for the wake meandering are comparable to the wake diameter which often, prior to wake expansion, is equal to the rotor diameter [16]. Due to the importance of turbulence for wake meandering, the atmospheric stability influences the tendency of wake meandering, with unstable conditions enhancing it [30].

2.4.3 Wake Deflection

Figure 2.7 shows a wind turbine with a yaw misalignment angle (γ), such that the normal of its rotor plane is no longer horizontally aligned with the mean wind direction. Thus, it exerts a mean thrust force (F) on the flow such that a cross wind component is induced, which deflects the mean wake centreline away from the streamwise direction (the x -axis). By the actuator disc theory introduced in Section 2.3.1, the streamwise and lateral components of the thrust force F can be expressed as

$$F_x = -C_T \rho A u_n^2 \cos \gamma \quad (2.31)$$

$$F_y = -C_T \rho A u_n^2 \sin \gamma \quad (2.32)$$

where A , ρ , u_∞ is the swept area of the rotor blades, the density of air, and the free stream velocity respectively. The lateral force (F_y) induces the cross wind velocity component, which causes the wake deflection. Its definition suggests that the thrust coefficient (C_T) plays a crucial role in deflecting the wake. Indeed, Jiménez, et al. [7] developed an analytical tool for predicting the wake skew angle (ϕ) which increases linearly with the thrust coefficient. The skew angle is indicated in Fig. 2.7 and is defined mathematically as

$$\phi = \left(\frac{D}{\delta} \right)^2 \frac{C_T}{2} \cos^2(\gamma) \sin(\gamma), \quad (2.33)$$

where δ is the wake width and grows with downwind distance (x). It can be approximated as [7]:

$$\delta = D + kx, \quad (2.34)$$

where k is a wake growth parameter, typically within the range 0.09 to 0.125 [7].

The skew angle as defined in Eq. (2.33) suggest that deflection is symmetrically dependent on the yaw angle. However, in practice this is rarely the case, due to the rotation of the blades [37]. As will be shown here, the angle of attack (α) depends on the yaw angle (γ) and the angle of rotation (ω), as defined in Fig. 2.5a. From Fig. 2.7, it is clear that the normal and lateral velocity components of the rotor plane can be expressed as,

$$u_n = u_\infty \cos \gamma \quad (2.35)$$

$$u_\tau = -u_\infty \sin \gamma, \quad (2.36)$$

respectively. The blade tangential velocity (u_ω) can be expressed as a function of the rotor plane-lateral velocity (u_τ), such that

$$u_\omega = -u_\tau \cos \omega. \quad (2.37)$$

If u_ω is positive (it is negative in Fig. 2.5b), it is clear to see that the flow angle (Φ) is

$$\tan \Phi = \frac{u_n}{r\Omega - u_\omega}. \quad (2.38)$$

Combining Eqs. (2.36) and (2.37), Φ can instead be expressed as

$$\tan \Phi = \frac{u_\infty \cos \gamma}{\Omega r - u_\infty \sin \gamma \cos \omega}. \quad (2.39)$$

An expression for the angle of attack is found by combining Eqs. (2.28) and (2.39), such that

$$\alpha = \arctan \left(\frac{u_\infty \cos \gamma}{\Omega r - u_\infty \sin \gamma \cos \omega} \right) - \beta. \quad (2.40)$$

In a uniform inflow, such that u_∞ is constant across the rotor, the angle of attack (averaged over a full rotation of the blades) has a symmetric dependence on γ . However, in the more realistic case of a sheared inflow, the average α has an asymmetric dependence on the yaw angle. As a consequence, the thrust coefficient also gets an asymmetric dependence on γ , hence, the wake should deflect differently, depending on whether γ is positive or negative.

2.5 FAST.Farm

FAST.Farm is a nonlinear time-domain multi-physics engineering tool composed of multiple submodules, which represent different physics domains of a wind farm [42]. It is an open-source mid-fidelity tool for predicting the power production and structural loads on wind turbines in wind farms. It is developed by the National Renewable Energy Laboratory (NREL) and is an extension of the software OpenFAST, which solves the aero-hydro-servo-elasto dynamics of individual turbines. The submodule hierarchy of FAST.Farm is illustrated in Fig. 2.8. It is shown that it has four submodules: The Super Controller module which allows for farm-wide logic to be employed, such as active yaw control; OpenFAST; Wake-Dynamics which models the advection, deflection, meandering and of the wakes; Ambient wind and wake merging are submodels of the Ambient Wind and Array Effects (AWAE) model. For each wind turbine included in a FAST.Farm simulation, there is one instance of the OpenFAST and Wake-Dynamics modules.

It must be emphasized that FAST.Farm is not a CFD tool, it does not resolve the governing equations for the flow. Rather, it inputs time-series of an already established wind field and superimposes the effect of the wind turbine wake upon that field. The input wind field may be generated with CFD, or by e.g. synthetic methods. This approach of superimposing wakes on wind fields renders FAST.Farm computationally inexpensive. However, it also means that FAST.Farm should preferably be calibrated on a case-by-case basis, using high-fidelity simulations, such as a LES. FAST.Farm has twenty tunable wake dynamics parameters. In this work, two of them will be calibrated, namely c_{meander} and MOD_{meander} which influence the deflection and meandering properties of the wakes.

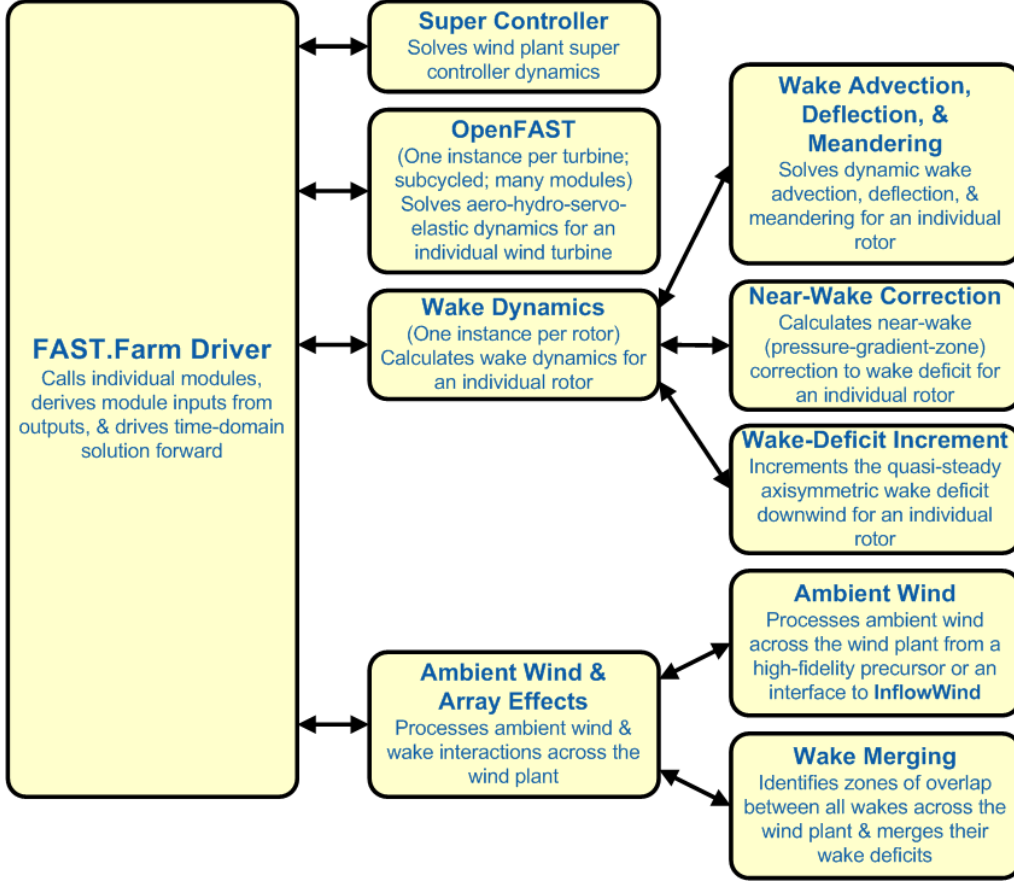


Figure 2.8: The hierarchy modules associated to FAST.Farm. Figure taken from [42].

2.5.1 Wake Dynamics Modelling

The wake dynamics model in FAST.Farm features a Dynamic Wake Meander (DWM) model which builds on previous models [42]. It addresses limitations of the previous DWM models, for example: wake deficit profile not being distorted by skewed inflow to the rotor; lack of deflection due to yaw misalignment; wake merging not accounted for; wakes not allowed to meander axially, to name a few. Figure 2.9 illustrate several key features of the wake dynamics in FAST.Farm. The blue lines in parallel with the corresponding rotor plane indicate the wake planes in which wake properties are solved. The blue dots and arrows show the wake centres and orientations, respectively. The grey lines indicate the wake centrelines. In areas of wake plane overlap, the wake merging is accounted for by summing their weighted contributed velocity deficits, which in turn affects individual wake behaviour (e.g. their advection speed). As in the DWM model developed by Larsen et al. [16], FAST.Farm models the wake meandering by treating the velocity deficit as a passive tracer, which is affected by eddies larger than two wake diameters [42]. The smaller eddies (less than two wake diameters) affect the evolution of the wake velocity deficit.

In the far-wake region, the so-called thin shear-layer approximation can be utilized, which is based on the Reynolds-Averaged Navier-Stokes equations² under quasi-steady-state and axisymmetric conditions. Under the assumption that radial velocity gradients are much larger than their axial counterparts, and that effects of pressure gradients and viscosity can be neglected, the Navier-Stokes equations can be expressed as:

$$V_x \frac{\partial V_x}{\partial x} + V_r \frac{\partial V_x}{\partial r} = \frac{1}{r} \frac{\partial}{\partial r} \left(r \nu_T \frac{\partial V_x}{\partial r} \right), \quad (2.41)$$

²The Reynolds-Averaged Navier-Stokes equations are time averaged Navier-Stokes equations with quantities (such as velocity and pressure) decomposed into a temporally averaged part and a fluctuating part. The so-called Reynolds decomposition leads to a closure problem involving the symmetric Reynolds stress tensor, which introduces six additional unknown variables. Various turbulence models handle the closure problem differently [55].

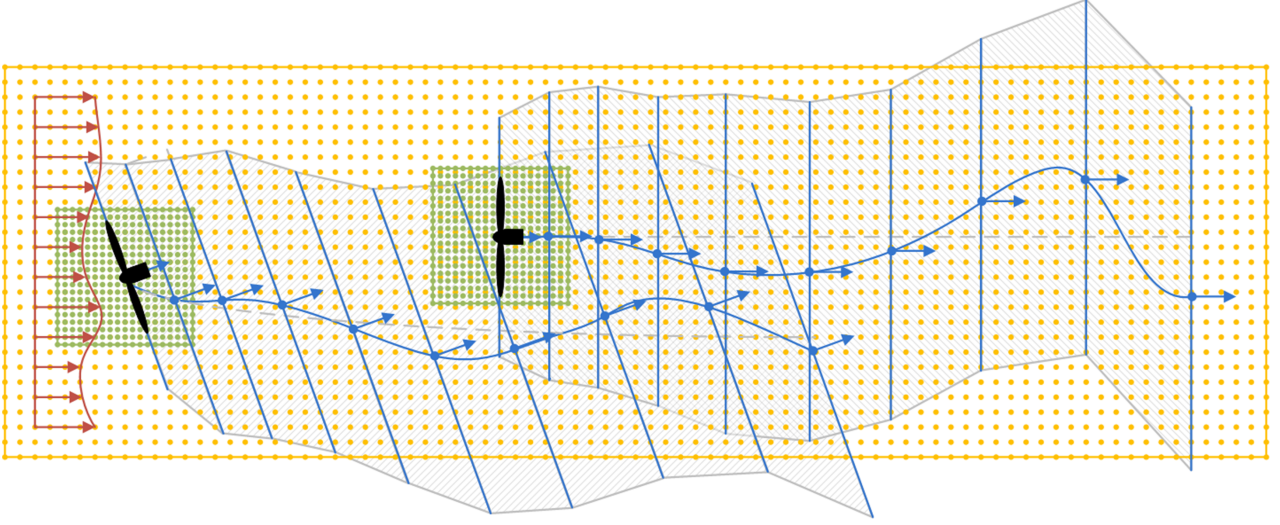


Figure 2.9: Schematic representation of the wake dynamics in FAST.Farm. The blue straight lines, dots and arrows represent radial wake planes, wake centres, and wake direction, respectively. The inflow wind profile is shown in red. The upwind turbine feels a skewed inflow due to its yaw angle. Figure taken from [42].

and

$$\frac{\partial V_x}{\partial x} + \frac{1}{r} \frac{\partial(rV_r)}{\partial r} = 0, \quad (2.42)$$

where Eqs. (2.41) and (2.42) represent the conservation of momentum and conservation of mass, respectively [42]. V_x , V_r , and ν_t is the axial and radial velocity components, and the eddy viscosity, respectively. In FAST.Farm, the eddy viscosity increases linearly with the ambient turbulence intensity. That implies that a highly turbulent ambient wind diffuses the wake to free stream conditions more rapidly than a low turbulent wind. In FAST.Farm, the momentum and mass conservation equations are solved in a finite difference approach.

The (blue) wake planes displayed in Fig. 2.9 indicate axisymmetric cross-sections of the wake, with properties defined at discrete radial nodes (n). The velocity of a wake plane m ($\mathbf{V}_m^{\text{Plane}}$) is taken as a weighted sum of the local disturbed wind (\mathbf{V}^{Dist}), which depends on the ambient wind and velocity deficits introduced by the wakes. Mathematically, it is defined as

$$\mathbf{V}_m^{\text{Plane}} = \frac{\sum_n w_n \mathbf{V}_n^{\text{Dist}}}{\sum_n w_n}, \quad (2.43)$$

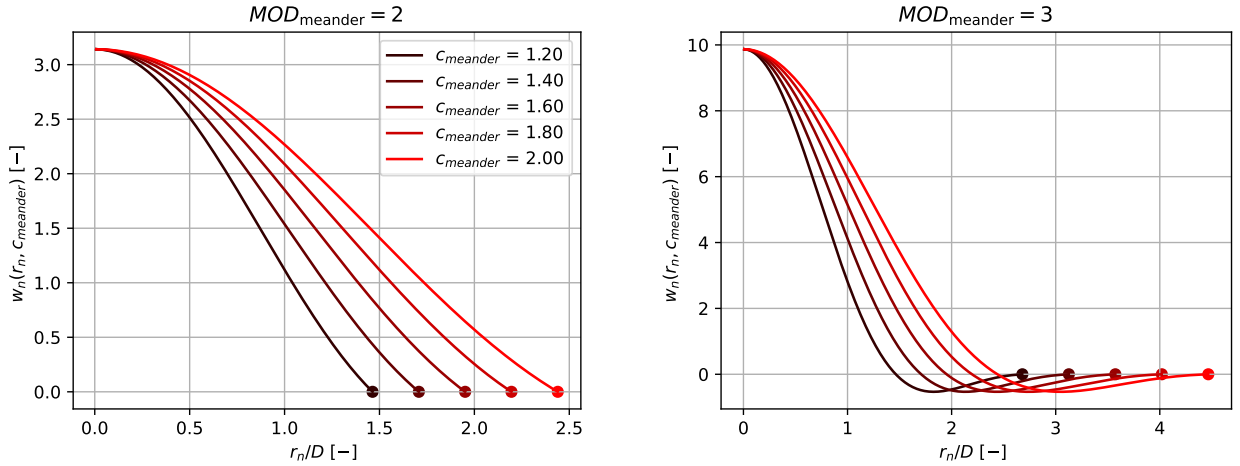
where w_n is a weight defined as

$$w_n = \begin{cases} 1 & \text{if } MOD_{\text{meander}} = 1, \\ jinc\left(\frac{r_n}{c_{\text{meander}}\delta}\right) & \text{if } MOD_{\text{meander}} = 2, \\ jinc\left(\frac{r_n}{c_{\text{meander}}\delta}\right)jinc\left(\frac{r_n}{2c_{\text{meander}}\delta}\right) & \text{if } MOD_{\text{meander}} = 3 \end{cases} \quad (2.44)$$

where MOD_{meander} and c_{meander} are wake dynamics parameters in FAST.Farm. The wake width is denoted by δ . The *jinc* function is defined as

$$jinc(r) = \frac{2 \cdot J_1(\pi r)}{r}, \quad (2.45)$$

where J_1 is a Bessel function of the first kind [42]. Figure 2.10 displays the weight function (w_n) for various values of c_{meander} and MOD_{meander} . For c_{meander} , an increase means that a larger area of the disturbed wind field will be weighted into the calculation of $\mathbf{V}_m^{\text{Plane}}$. Hence, the effect of increasing c_{meander} is a wake plane which moves more similarly to the ambient wind, which means that the wake will not meander and deflect as easily. In contrast, for low c_{meander} , the movement of the wake plane is to a larger degree dictated by the velocity field close to the core of the wake, meaning that wake deflecting and meandering tendencies of the wake are intensified. By the same reasoning, for $MOD_{\text{meander}} = 2$, the weight is less concentrated near the wake centre, as compared to for $MOD_{\text{meander}} = 3$, hence a lower MOD_{meander} should yield less exaggerated wake meandering and deflection.



(a) The radial dependence of w_n for $MOD_{\text{meander}} = 2$ (b) The radial dependence of w_n for $MOD_{\text{meander}} = 3$

Figure 2.10: Curves for the weight w_n as a function of the two wake parameters MOD_{meander} and c_{meander} , and the radial distance from the wake plane centre (r_n). The subscript n denotes the radial node number. The dots (●) indicate the points of truncation for w_n , which corresponds to $1.21967c_{\text{meander}}\delta$ and $2.23313c_{\text{meander}}\delta$ for $MOD_{\text{meander}} = 2$ and $MOD_{\text{meander}} = 3$, respectively. Note that r_n is shown as continuous here, while it is discrete in FAST.Farm.

2.6 Artificial Neural Networks

The 10^{11} neurons in our brains are connected in tree-like networks. Each neuron is connected with hundreds to thousands of other neurons by synapses [63]. Despite a single neuron performing computations around a million times slower than a silicon semiconductor, due to the complex connections of the brain, it is able to perform complicated tasks much faster rate than any computer can. For a biological neural network (BNN), e.g. the human brain, complex tasks such as locomotion and face recognition are quickly executed in a greatly parallelized manner, a feature which is enabled by the architecture of the network [64], i.e. the ways in which the synapses connect different neurons.

Artificial neural networks (ANNs) are mathematical structures which are inspired by their biological counterparts and are able to approximate any function [65]. With simplified abstractions of the neurons (nodes) and synapses (weights) in a biological neural network, the ANN seeks to mimic certain aspects of the BNN, namely their parallelized computing, robustness, flexibility, and ability to generalize [64, 66]. An obstacle to overcome when constructing an ANN is finding a suitable structure of nodes and weights which can represent the function at hand.

An early model of the neuron is the McCulloch-Pitts neuron. They described the state of the neuron as binary. It is either firing or not firing, depending on inputs from other neurons and their mutual synapse strength. A generalization of the model is shown schematically in Fig. 2.11. The output (a_i) of neuron i is defined mathematically as [64]:

$$a_i = g \left(\sum_j w_{ij} a_j + b_i \right), \quad (2.46)$$

where w_{ij} , a_j , b_i , t denotes the weight (synapse strength) between node (neuron) i and j , the output of node j , the bias of node i , respectively. g is the activation function, of which there are many, but a commonly used one is the Hyperbolic tangent, defined as:

$$g(x) = \tanh(x) = \frac{e^x - e^{-x}}{e^x + e^{-x}}. \quad (2.47)$$

In the generalized case, the state of the neuron is no longer necessarily binary, rather it is continuous.

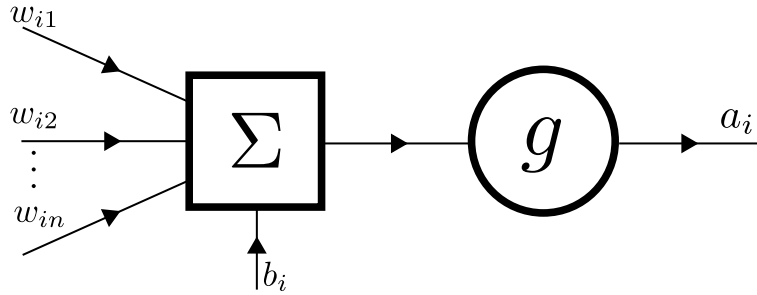


Figure 2.11: The generalized McCulloch-Pitts model of neuron i

2.6.1 Feedforward Neural Network

There are many types of ANNs, and they differ in how the outputs of neurons are handled. The type most commonly used is the Feedforward Neural Network (FFNN), in which information propagates only forward, from the input nodes to the output nodes [63]. The FFNN usually consists of layers of neurons, which are categorized in three types. As seen in Fig. 2.12, there is an input layer and an output layer. Between them, there can be any number of hidden layers. Each layer consist of a varying amount of neurons, each of which operate as the generalized McCulloch-Pitts neuron shown in Fig. 2.11.

Given an input vector (\mathbf{x}), the output of an FFNN with L layers ($\hat{\mathbf{y}}$), excluding the input layer, can be found as the function composition [66]:

$$\hat{\mathbf{y}} = g^L(\mathbf{W}^L g^{L-1}(\mathbf{W}^{L-1} \dots g^2(\mathbf{W}^2 g^1(\mathbf{W}^1 \mathbf{x} + \mathbf{b}^1) + \mathbf{b}^2) \dots + \mathbf{b}^{L-1}) + \mathbf{b}^L), \quad (2.48)$$

where \mathbf{W}^l , \mathbf{b} , and g^l denotes a matrix of weights between layer $l - 1$ and l , a vector of biases to each neuron in layer l , the activation function at layer l , respectively. A key point to understand from Eq. (2.48) is that the output of any layer is used as input in the next layer. Information is fed forward.

2.6.2 Backpropagation

To construct the ANN such that it approximates a given function sufficiently well, the strength of its synapses (weights) have to be adjusted such that the ANN produces the desired outputs for a given input. The process of adjusting the weights and biases in the neural network is called training, a process in which the ANN learns how it should best handle inputs. One category of learning is called supervised learning. In supervised learning, for any input vector (\mathbf{x}) the ANN is given a desired output vector (\mathbf{y}) [63]. Hence, the weights of the ANN can be optimized such that its outputs ($\hat{\mathbf{y}}$) are as close to \mathbf{y} as possible. To optimize the weights, some measure to evaluate the ANN is needed. This is the role of the cost function (C). There are various cost functions, but the one used in this work is the mean squared error (MSE), defined mathematically as:

$$C(\mathbf{y}^m, \hat{\mathbf{y}}^m) = \frac{1}{M} \sum_m (\mathbf{y}^m - \hat{\mathbf{y}}^m)^2, \quad (2.49)$$

where M is the number of input-output pairs \mathbf{x}^m , \mathbf{y}^m and $m = 1, 2, \dots, M - 1, M$. To train the ANN is to minimize C . By studying the gradient of C with respect to the weights, the optimal weights can be found e.g. by gradient descent optimization algorithm. The backpropagation method exploits the chain rule to avoid duplicate calculations, thus speeding up the training of the neural network considerably. The weight optimization is done iteratively and incrementally at some learning rate. Each such iteration is called an epoch.

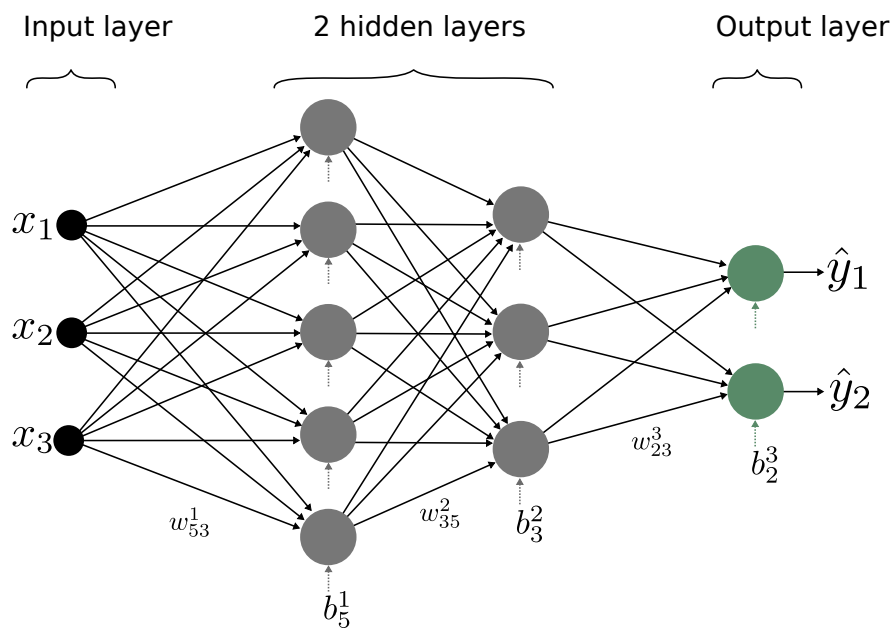


Figure 2.12: A feedforward neural network with two hidden layers. The first layer has 5 neurons, the second layer has 3 neurons. Each neuron operate as a generalized McCulloch-Pitts neuron, shown in Fig. 2.11. The last elements of the weights matrices \mathbf{W}^l ($l = 1, 2, 3$) are marked. Likewise, the last elements of the bias vectors (\mathbf{b}^l), corresponding to each layer, are shown. All other elements are implied by solid and dotted arrows for the weights and biases, respectively.

3 Method

In the following sections, descriptions are given for the methodology of calibrating FAST.Farm, training the Artificial Neural Network (ANN), and developing the Active Yaw Control (AYC). Figure 3.1 shows the general workflow of the project. First, a calibration of FAST.Farm is conducted using results from a Large-Eddy Simulation (LES). In this stage, only LES data is used for generating wind fields in FAST.Farm. In the later stages, only synthetic ambient wind is utilized.

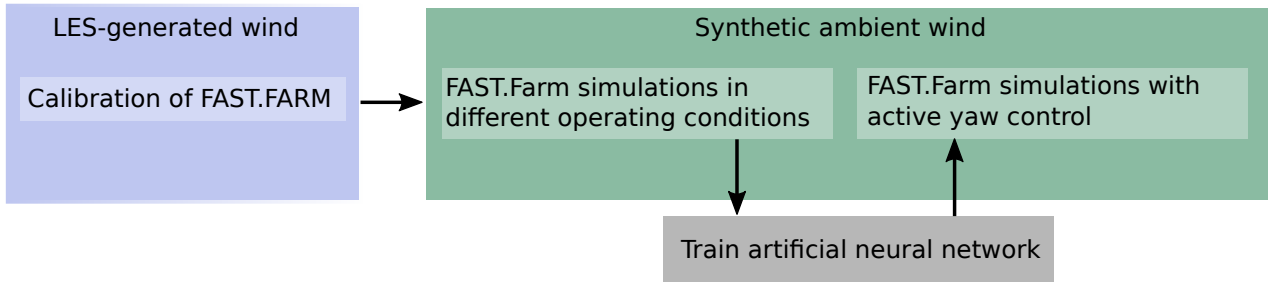


Figure 3.1: Project work flow chart. Large-Eddy Simulation data is used for the calibration of FAST.Farm. Synthetic turbulence generated with TurbSim is used for all other steps of the work.

3.1 FAST.Farm Computational Domain

For all FAST.Farm simulations, the discretization and choice of domain dimensions are informed by the guidelines given by the FAST.Farm manual [42] and a discretization sensitivity study by Shaler et al. [45]. Figure 3.2 illustrates both a FAST.Farm domain and a 3D structured grid which represents its discretization. The blue-tinted zones indicate high-resolution domains which encompass the two turbines, which are situated a distance of $l_2 = 7D$ away from each other. Both high resolution domains have the same dimensions. The low-resolution domain and the high-resolution domains are discretized as three-dimensional structured grids, shown schematically in Fig. 3.2. The subscripts "low" and "high" and denote properties of the low- and high-resolution domains, respectively. The values of the dimensional parameters shown in Fig. 3.2 are indicated

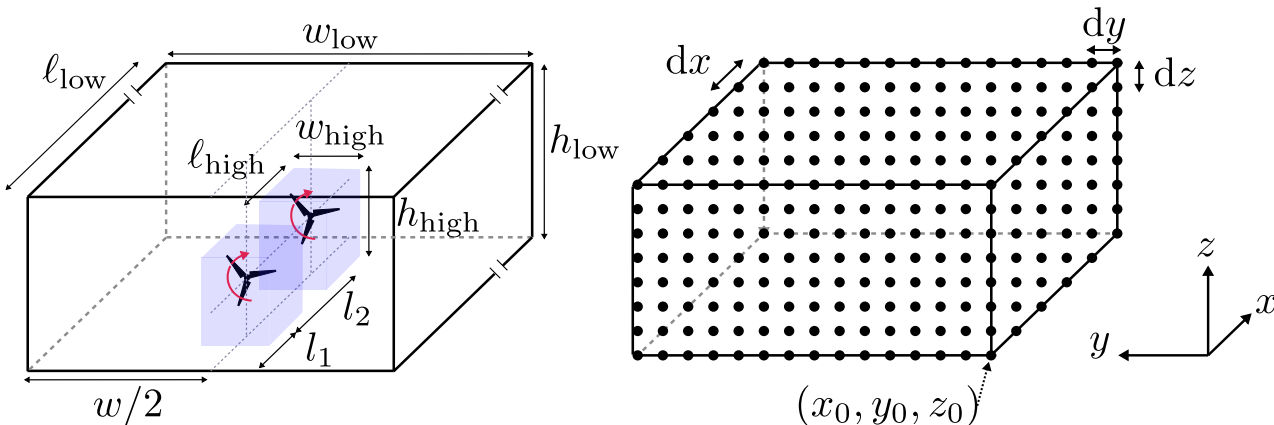


Figure 3.2: Schematic view of the FAST.Farm domain (left) and its discretization (right)

in Tab. 3.1. It should be noted that the listed values are the desired values and can differ slightly from what is actually implemented, as the lengths have to coincide with the number of nodes and discretization, i.e. the dimensional parameters are taken as integer multiples of the discretization lengths (e.g. dx_{low} and dy_{high}). Moreover, most parameters are set to constants for the FAST.Farm simulations. However, some of them varies, e.g. the streamwise discretization length (dx_{low}) which depends on the inflow, which is described in more detail in Section 3.2.

Table 3.1: Dimensional and discretization parameter values. The turbine rotor diameter is denoted by $D = 126$ m.

Property	Expression	Value
dt_{low}	$c_{\text{meander}}D/(10\langle u \rangle_{\text{hub}})$	-
dt_{high}	$1/(2f_{\text{max}})$	0.1 s
ℓ_{low}	$25D$	3150 m
w_{low}	$6D$	756 m
h_{low}	$2.233c_{\text{meander}}D$	-
$\ell_{\text{high}}, w_{\text{high}}, h_{\text{high}}$	$1.4D$	180 m
l_1	$3D$	378 m
l_2	$7D$	882 m
dx_{low}	$V_{\text{advect}}dt_{\text{low}}$	-
$dy_{\text{low}}, dz_{\text{low}}$	$2c_{\text{max}}$	10 m
dx_{high}	$dx_{\text{low}}/c_{\text{max}}$	-
$dy_{\text{high}}, dz_{\text{high}}$	c_{max}	5 m

3.2 TurbSim

TurbSim is a tool developed by NREL which can be used to generate time series of 2D wind fields. Using Taylor’s frozen turbulence hypothesis, those 2D planes can be advected at a mean wind speed (V_{advect}). This effectively creates a 3D wind field, as illustrated in Fig. 3.3. Turning 2D wind fields into 3D fields is done in FAST.Farm through a submodule called InflowWind.

The generated wind fields are 1200 s long, and their dimensions match the FAST.Farm lateral and vertical dimensions, i.e. $6D \times 2.233c_{\text{meander}}D$. The time length of the TurbSim-generated flows (20 min) is chosen as to let the wake fully develop and be at least long enough to capture correlated turbulent patterns. An account of the relevant turbulent length and time scales for the Atmospheric Boundary Layer (ABL) is discussed further in Appendix A.2.2. The spatial resolution of the turbulent planes is $10 \text{ m} \times 10 \text{ m}$. The temporal resolution is 0.1 s, matching dt_{high} in FAST.Farm.

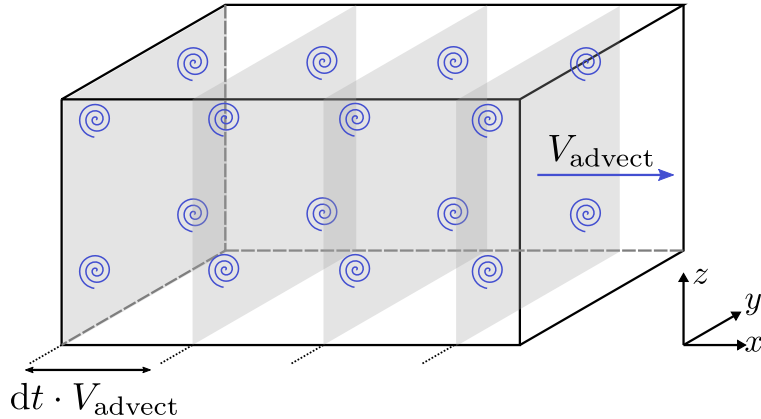


Figure 3.3: TurbSim-generated 2D planes of turbulent wind fields propagating at an advection speed (V_{advect}) in a FAST.Farm domain. In one time step (dt) the plane travels a distance of $dt \cdot V_{\text{advect}}$.

3.3 Calibration

In this section, the method of calibrating FAST.Farm is described, for which a set of derived quantities is compared from the results of a LES and twenty FAST.Farm simulations, each with a unique combination of parameters. The topics at hand include the definition of the wake quantities and how to identify and track the wake in planes downwind of the turbines.

FAST.Farm can be calibrated to high-fidelity simulations, such as large-eddy simulations. For this purpose, FAST.Farm have 20 adjustable parameters which control the wake dynamics. Default values for these parameters

have been found by Doubrawa et al. [46], who performed numerous large-eddy simulations in an extensive calibration process. However, as the wind farm conditions for this study differ slightly from those in the work by Doubrawa et al., a new calibration is performed here. Two parameters are optimized in a grid search, namely c_{meander} and MOD_{meander} , which affect the meandering and deflected behaviour of the wake [42], as discussed in Section 2.5.1. These two parameters are calibrated because the wake deflection is crucial for wake steering, which is what the active yaw control is designed to do. The considered values for these parameters are shown in Tab. 3.2. The thrust and torque for both turbines for the FAST.Farm and LES results are also compared, as

Table 3.2: All the parameter values for the calibration. n denotes the number of values tested and implies what those values are, as the respective parameter values are equally spaced.

Parameter	[min, max]	n
c_{meander}	[1.2, 2.1]	10
MOD_{meander}	[2, 3]	2

to not sacrifice accuracy in other turbine responses in favour of wake prediction.

The LES is made by Dr. Hamidreza Abedi, using 1D actuator disc models for the two wind turbines, situated on a row, 7D apart. Instantaneous wind velocity data is extracted in planes at the same distances (relative to the turbines) as in the FAST.Farm simulations, as shown in Fig. 3.4. The specified inflow conditions for the LES are listed in Tab. 3.3.

Table 3.3: Inflow conditions for the Large-Eddy Simulation

Property	Symbol	Value
Turbulence intensity	TI	10 %
Wind shear exponent	α	0.109
Mean wind speed at hub height	$\langle u \rangle_{\text{hub}}$	8 m s^{-1}

As indicated by Tab. 3.2, twenty FAST.Farm simulations are made, each with a unique combination of c_{meander} and MOD_{meander} . Extracted wind velocity field from the LES is used to generate inflows for FAST.Farm. To fulfil the FAST.Farm discretization guidelines [42], three different inflows are generated. One for the low-resolution domain, and two for the turbine-encompassing high-resolution domains. The three wind fields are spatio-temporally synchronized. Using numerous inflows is done to alleviate computational constraints. It is computationally costly to generate an inflow which fulfils the high-resolution discretization requirements for the whole low-resolution domain. As a solution, the low- and high-resolution inflows are discretized differently.

3.3.1 Wake Quantities

The calibration is done by finding the set of values for c_{meander} and MOD_{meander} which yields the lowest calibration error (Δ_{sim}). The error depends on a set of derived wake quantities which are listed here:

- $\langle \delta V_x(r, x) \rangle$ - temporal mean of axial velocity deficit.
- $\langle \delta V_r(r, x) \rangle$ - temporal mean of radial velocity deficit.
- $\mu_{\text{wake}}(x)$ - temporal mean of the wake centre’s radial displacement.
- $\sigma_{\text{wake}}(x)$ - standard deviation of the wake centre’s radial displacement.

A central quantity is the velocity deficit ($\delta \mathbf{v}$), which is defined here as:

$$\delta \mathbf{v}(t, x, y, z) = \mathbf{v}(t, x, y, z) - \mathbf{v}_{\infty}(z), \quad (3.1)$$

where $\mathbf{v}(t, x, y, z)$ and $\mathbf{v}_{\infty}(z)$ is the instantaneous wind velocity field and a free stream velocity field, respectively. The latter is estimated using the power law defined in Eq. (2.3) for $\alpha = 0.109$ and $u_{\text{ref}} = \langle u \rangle_{\text{hub}} = 8 \text{ m s}^{-1}$ and $z_{\text{ref}} = z_{\text{hub}} = 90 \text{ m}$. Using $\delta \mathbf{v}$, the relevant velocity deficits ($\langle \delta V_x \rangle$ and $\langle \delta V_r \rangle$) can be calculated. Note that both $\langle \delta V_r \rangle$ and $\langle \delta V_x \rangle$ have a radial dependence, which is with respect to the wake centre. This is discussed in more detail in Section 3.3.3

The four quantities listed above are readily available outputs from FAST.Farm. However, for LES, they have to be derived by first identifying the wake and its centre. In this work, the wake is tracked in 10 so-called

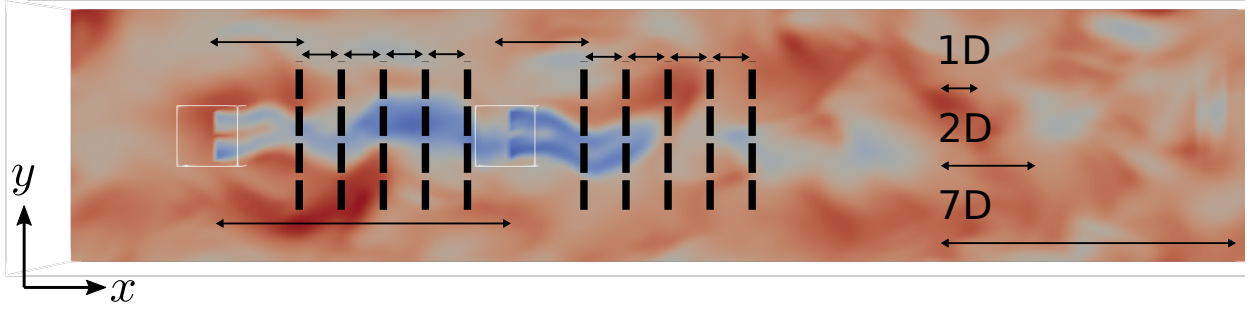


Figure 3.4: Waked velocity magnitude field in the FAST.Farm domain. Blue and red regions indicate low and high velocity areas, respectively. Positions of the data extraction planes are shown by the bold dashed lines. White areas highlight the high resolution domains.

data extraction planes, which are indicated by the bold dashed lines in Fig. 3.4. Once the derived quantities are found from the LES wind fields, the calibration error (Δ_{sim}) can be calculated as [46]:

$$\Delta_{\text{sim}} = \Delta\langle\delta V_r\rangle + \Delta\langle\delta V_x\rangle + \Delta\mu_{\text{wake}} + \Delta\sigma_{\text{wake}} \quad (3.2)$$

$$\Delta\langle\delta V_r\rangle = \sum_{1T}^{2T} \sum_{2D}^{6D} \left(\frac{\|\langle\delta V_r\rangle_{\text{FF}}(r, x) - \langle\delta V_r\rangle_{\text{LES}}(r, x)\|}{\|\langle\delta V_r\rangle_{\text{LES}}(r, x)\|} \right) \quad (3.3)$$

$$\Delta\langle\delta V_x\rangle = \sum_{1T}^{2T} \sum_{2D}^{6D} \left(\frac{\|\langle\delta V_x\rangle_{\text{FF}}(r, x) - \langle\delta V_x\rangle_{\text{LES}}(r, x)\|}{\|\langle\delta V_x\rangle_{\text{LES}}(r, x)\|} \right) \quad (3.4)$$

$$\Delta\mu_{\text{wake}} = \sum_{1T}^{2T} \sum_{2D}^{6D} \left(\frac{\|\mu_{\text{wake,FF}}(x) - \mu_{\text{wake,LES}}(x)\|}{\|\mu_{\text{wake,LES}}(x)\|} \right) \quad (3.5)$$

$$\Delta\sigma_{\text{wake}} = \sum_{1T}^{2T} \sum_{2D}^{6D} \left(\frac{\|\sigma_{\text{wake,FF}}(x) - \sigma_{\text{wake,LES}}(x)\|}{\|\sigma_{\text{wake,LES}}(x)\|} \right) \quad (3.6)$$

where the subscripts *LES* and *FF* denotes the wake quantities from the LES and the FAST.Farm simulations, respectively. *T* and *D* denotes the wind turbine and downstream distance from said turbine, respectively. That is to say, Δ_{sim} is the sum of normalized errors in 5 planes downwind of both wind turbines. A reason why data extraction planes closer to the turbines are excluded (e.g. at 1D downwind of any turbine) is that the wake behaviour is expected to be inaccurate in the very near-wake region [44]. The norms in Eqs. (3.3)-(3.6) are Frobenius norms, defined mathematically as [67]

$$\|A\|_F = \sqrt{\sum_{i=1}^m \sum_{j=1}^n |a_{ij}|^2}, \quad (3.7)$$

where *A* is a matrix and a_{ij} its element in row *i* and column *j*.

3.3.2 Wake Tracking Methods

The lateral and vertical position of the wake centre (denoted by y_{wake} and z_{wake} , respectively) in the data extraction planes shown in Fig. 3.4 can be found by wake tracking techniques. To identify the wake, the Simulated And Measured Wake Identification and CHaracterization (SAMWICH) toolbox [68] is utilized, which has been used in previous studies by NREL [46, 69]. For later comparisons, three different wake tracking techniques are utilized to identify the wake and calculate the wake quantities described in Section 3.3.1. In this work, the three techniques are referred to as "Vollmer", "Gaussian", and "Bastankhah". They are shown together in Fig. 3.5. At each time step, the different methods try to find a region in the data extraction plane which best match an expected waked velocity field. The rest of this section is devoted to explaining how the individual methods work.

The method called Vollmer is based on the work by Vollmer et al. [30]. It attempts to find an area in the waked flow equal in size to the rotor-swept area ($\pi D^2/4$) which corresponds to the minimum available mean specific power of a hypothetical downwind turbine. Mathematically, it can be defined as minimizing the function f_V under certain constraints, specifically:

$$f_V = \frac{1}{2} \int_{y_1}^{y_2} \int_{z_1}^{z_2} u^3 dy' dz', \quad (3.8)$$

where y' and z' are dummy variables under the constraint

$$(y' - y_{\text{wake}})^2 + (z' - z_{\text{wake}})^2 \leq (D/2)^2. \quad (3.9)$$

Hence, the coordinate pair $y_{\text{wake}}, z_{\text{wake}}$ which minimizes Eq. (3.8) under the constraint given by Eq. (3.9) is said to be the centre of the wake.

The Gaussian method is quite straightforward. It attempts to fit (in a least-square sense) the following function (f_G) to the axial velocity deficit field (δV_x):

$$f_G = -u_a \exp \left[-\frac{1}{2} \frac{4}{D^2} ((y - y_{\text{wake}})^2 + (z - z_{\text{wake}})^2) \right], \quad (3.10)$$

where u_a is the minimum velocity deficit at the current time step [68]. The pair $y_{\text{wake}}, z_{\text{wake}}$ which provides the fit with the lowest least square error is taken as the wake centre.

The technique named Bastankhah is based on the work by Bastankhah et al. [70]. It is similar to the Gaussian method, but attempts to account for the expansion of the wake with downwind distance (and among the three methods, it is the only one to do so). As in the case of the Gaussian methods, a pair of $y_{\text{wake}}, z_{\text{wake}}$ is searched for, such that a function (f_B) is fitted to the axial velocity deficit field in a least-square sense. Mathematically is is defined as

$$f_B = -u_a \left(1 - \sqrt{1 - \frac{C_T}{8\eta^2}} \right) \exp \left[-\frac{1}{2\eta^2} \frac{1}{D^2} ((y - y_{\text{wake}})^2 + (z - z_{\text{wake}})^2) \right], \quad (3.11)$$

where

$$\eta = k \cdot x/D + \sqrt{\beta}/5 \quad (3.12)$$

where $k = 0.03$ and x denotes a wake growth parameter and the downwind distance, respectively. β is a function of the thrust coefficient (C_T), such that

$$\beta = \frac{1 + \sqrt{1 - C_T}}{2\sqrt{1 - C_T}}. \quad (3.13)$$

The Gaussian and Bastankhah methods will always fit their respective functions to the waked velocity field and thus find a wake centre, regardless of validity. This is not the case for the Vollmer method, which may fail, and in fact does so quite often. This is a perk of the Vollmer method.

3.3.3 Radial Dependence of Velocity Deficits

In FAST.Farm, the wakes are treated as axisymmetric. To compare the results of the LES and the FAST.Farm simulations, the LES-derived velocity deficits have to be calculated in a cylindrical coordinate system with its origin at the wake centre ($y_{\text{wake}}, z_{\text{wake}}$). The following coordinate transformation is used for this purpose:

$$\begin{bmatrix} \hat{\mathbf{x}} \\ \hat{\mathbf{y}} \\ \hat{\mathbf{z}} \end{bmatrix} = \begin{bmatrix} 1 & 0 & 0 \\ 0 & -\sin \theta & -\cos \theta \\ 0 & \cos \theta & -\sin \theta \end{bmatrix} \begin{bmatrix} \hat{\mathbf{x}} \\ \hat{\mathbf{r}} \\ \hat{\boldsymbol{\theta}} \end{bmatrix}, \quad (3.14)$$

where $\hat{\boldsymbol{\theta}}$ and $\hat{\mathbf{r}}$ denotes the azimuthal and radial unit vectors, respectively. $\hat{\mathbf{x}}, \hat{\mathbf{y}}$ and $\hat{\mathbf{z}}$ denotes the streamwise, lateral, and vertical unit vectors (in a Cartesian coordinate system), respectively. The radius from the wake centre (r) is defined as

$$r = \sqrt{(z - z_{\text{wake}})^2 + (y - y_{\text{wake}})^2} \quad (3.15)$$

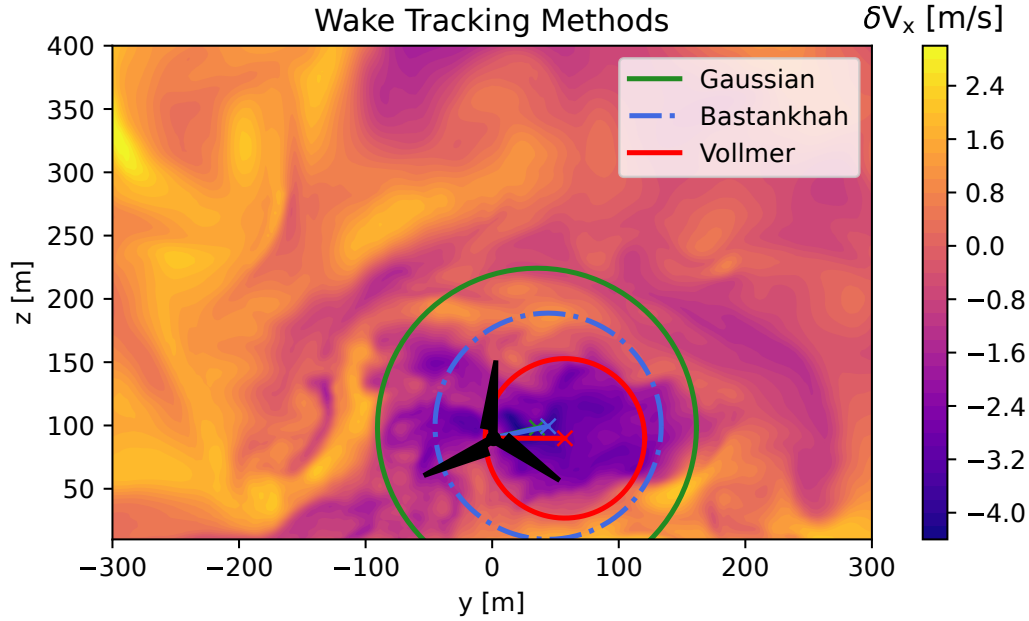


Figure 3.5: Three wake tracking methods at the plane 4D downstream of the upwind turbine (WT1), which is represented by the black blades. The contours indicate the axial velocity deficit field. The circle contours denote the predicted wake regions, and the cross markings the wake centres. The lengths of the lines between the turbine hub and wake centres indicate the radial displacement of the wake centre.

and θ is the polar angle defined as

$$\theta = \arctan \left(\frac{-(y - y_{\text{wake}})}{z - z_{\text{wake}}} \right). \quad (3.16)$$

A vector field (\mathbf{A}) can be described in both a Cartesian and a polar coordinate system, such that the following relation holds,

$$\mathbf{A} = A_x \hat{\mathbf{x}} + A_r \hat{\mathbf{r}} + A_\theta \hat{\boldsymbol{\theta}} = A_x \hat{\mathbf{x}} + A_y \hat{\mathbf{y}} + A_z \hat{\mathbf{z}}, \quad (3.17)$$

where the A_i denotes the vector component in the direction. By applying the coordinate transformation defined in (3.14) to the right-hand side of Eq. (3.17), an expression for the radial component can be found as:

$$A_r = -A_y \sin \theta + A_z \cos \theta. \quad (3.18)$$

Hence the radial velocity deficit is determined from the Cartesian velocity deficit components such that

$$\delta V_r(t, x, r, \theta) = -\delta v \sin \theta + \delta w \cos \theta, \quad (3.19)$$

where δv and δw are the lateral and vertical velocity deficit components of $\delta \mathbf{v}$, which is given by Eq. (3.1).

In FAST.Farm, the velocity deficits have no azimuthal dependence, only radial, hence the LES derived velocity deficits are azimuthally averaged. This averaging is done by sampling the velocity deficit at 40 equidistant radial positions, for 12 different values of θ , and then averaging with respect to θ . The sampling points can be viewed superimposed on a waked velocity field in Fig. A.1.

3.4 Artificial Neural Network

In this section, the method of selecting a suitable Artificial Neural Network (ANN) and training it to data is described. The purpose of the neural network is to predict the mean wind farm power production ($\langle P \rangle_{\text{tot}}$), given the turbulence intensity (TI), wind shear exponent (α) and the yaw angle of the upstream wind turbine (γ_1).

When training the ANN, the mean squared error (MSE) is used as a loss function, as defined in Eq. (2.49). The Adam algorithm is chosen as the optimizer, which is a stochastic gradient descent algorithm with a unique and adaptive learning rate for each parameter (weights and biases) [71]. PyTorch [72] is used as framework to build and train the ANN.

3.4.1 FAST.Farm Simulations

To produce data to be used in training the neural network, 504 FAST.Farm simulations are made. For each such simulation, a combination of the operating conditions listed in Tab. 3.4 is selected. There are 72 possible combinations. For each combination, 6 turbulent realization are made (TurbSim is run with 6 different random seeds). For all operating conditions, the inflow is such that $\langle u \rangle_{\text{hub}} = 8 \text{ m s}^{-1}$

Table 3.4: All operating conditions for training the ANN. n denotes the number of values tested and implies what those values are, as the respective parameter values are equally spaced.

Variable	[min, max]	n	Unit
γ_1	[-15, 30]	7	deg
α	[0.1, 0.2]	3	-
TI	[5, 20]	4	%

3.4.2 Hyperparameters Grid Search

To make a neural network generalize well (i.e. to adequately predict correct outputs for unseen inputs), a common approach is to split the measurement data into a training set and a validation set, a method which is called hold-out validation. The optimization of the weights in the neural network is done with respect to the training set, but its performance is evaluated using the validation set. This approach can prevent overfitting, which is when the ANN fits to the noise in measurements and thus fails to capture the trends in the data, which is what is generally desired [63]. An ANN which performs well on a validation set does not necessarily generalize well, e.g. because the ANN can perform well by chance. A remedy to this problem is K-Fold cross validation, which is a technique used to evaluate the performance of a particular ANN architecture in a robust way [73]. The K-fold procedure is illustrated in Fig. 3.6 for $K = 5$. The dataset is split into five subsets ("folds") of approximately equal size. In a process which is repeated 5 times, one fold is chosen as the validation set, and the remaining four folds are taken as training sets. The performance of the model is measured as the mean across all the validation sets. If an ANN performs well in a K-Fold cross validation, it is thought to generalize well.

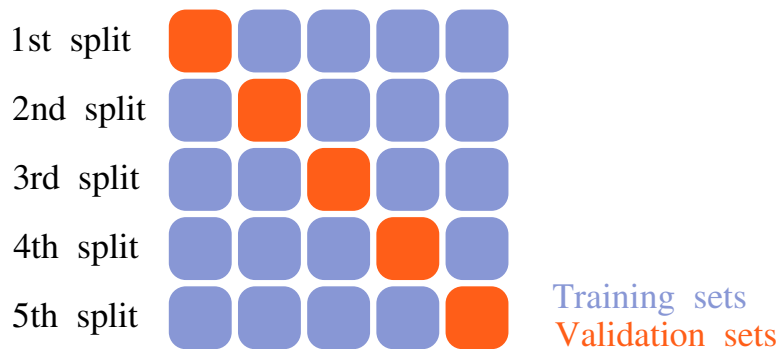


Figure 3.6: Schematic representation of the K-Fold cross validation process

A hyperparameter is a parameter used to control the ANN learning process. Examples of hyperparameters include: the number of hidden layers (the depth); the number of nodes (the width); the type of layer activation function (g^ℓ); the number of epochs; and the learning rate. An optimal ANN architecture can be found through a process of hyperparameter tuning [74]. To determine apt hyperparameters for this work, a grid search is done, such that all possible combinations of the hyperparameter values listed in Tab. 3.5 are explored. Details of the procedure are given in Section A.2.3. The optimal hyperparameters are found as Width = 3, Depth = 3, Number of epochs = 40000. The ANN architecture ultimately used is shown schematically in Fig. 3.7.

Table 3.5: The different ranges of hyperparameters changed for the neural network in a grid search for optimal parameters.

Hyperparameter	Values
Width	3,4,5
Depth	1,2,3
Number of epochs	20000, 40000, 80000

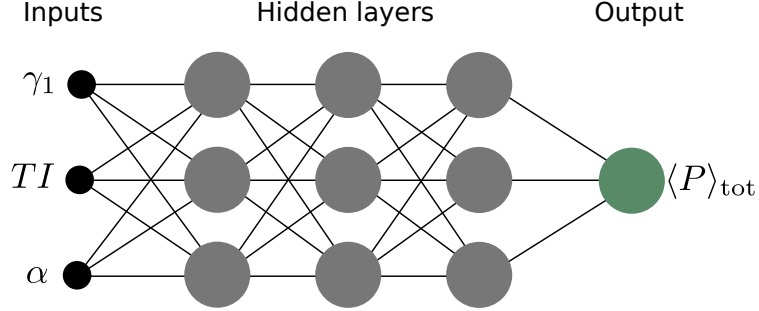


Figure 3.7: The architecture for the chosen neural network

3.5 Active Yaw Control

The Active Yaw Control (AYC) is the logic implemented into FAST.Farm’s super controller module. It aims to increase the mean wind farm power production ($\langle P \rangle_{tot}$) by dynamically yaw misaligning the upwind turbine. Thus, the power output of the upwind turbine is decreased, but by wake deflection the loss of power output can be more than compensated by the increase in power output of the downwind turbine. To evaluate the AYC, a number of FAST.Farm simulations are made with and without the AYC for later comparisons of the wind farm performance (e.g. wind farm power production). Each of the 12 unique combinations of α and TI listed in Tab. 3.4 are simulated for 6 turbulent realizations. Furthermore, to evaluate the AYC in operating conditions for which the ANN has not been trained, 6 turbulent realization of an interpolated case ($\alpha = 0.12$ and $TI = 8\%$) and an extrapolated case ($\alpha = 0.17$ and $TI = 25\%$) are simulated in FAST.Farm. Thus, a total of $6 \cdot (12 + 2) = 84$ FAST.Farm simulations are conducted with the AYC enabled.

3.5.1 Control Algorithm

To increase $\langle P \rangle_{tot}$, the artificial neural network is used to predict the wind farm power production for random yaw angles (for the upwind wind turbine). In each calling of the control algorithm, the wind farm power is predicted at the current operating condition (given the turbulence intensity, wind shear exponent, and the yaw angle). If a random yaw angle (γ_1^*) is found such that the corresponding predicted total power exceeds the power output at the current operating condition, the upwind turbine is given instructions to change its yaw angle to γ_1^* . Only positive yaw angles are searched for due to the negative angles being associated with higher loads and hence increased costs [24]. Pseudocode for the algorithm is shown below in Algorithm 1. The control scheme is loosely based on the work by Gebraad et al. [41], who uses a parametric model to predict steady state power production and to optimize the yaw angles of six wind turbines comprising a wind farm. In contrast, the control strategy for this study revolves around the artificial neural network predicting wind farm power outputs. Opting for the game-theoretic approach of Algorithm 1 has two apparent perks. It is straight-forward to implement, and due to its stochastic nature, its search for an optimum will not get stuck by finding a local optima.

3.5.2 Low-Pass Filter

Because the ANN is trained with temporally averaged data, there is a need to filter the input signals to the ANN during runtime, as the instantaneous data fluctuates. This need is met by using a four-stage cascaded recursive low-pass filter. Mathematically, the filter is defined as [75]:

$$y_n = a_0 x_n + b_1 y_{n-1} + b_2 y_{n-2} + b_3 y_{n-3} + b_4 y_{n-4}, \quad (3.20)$$

Algorithm 1 Pseudocode for the yaw control algorithm. The algorithm uses the artificial neural network to predict the mean wind farm power production at the estimated current operating condition (TI, α, γ_1) and at a potentially better operating condition (TI, α, γ_1^*) . The E parameter dictates how often to use the optimization algorithm. k denotes the number of random yaw angles to try. The random values are picked from uniform distributions.

```

loop
   $t \leftarrow t + \Delta t$ 
   $r \leftarrow$  random value  $\in [0, 1]$ 
  Estimate current turbulence intensity,  $TI$ 
  Estimate current wind shear exponent,  $\alpha$ 
  Estimate current yaw angle of upwind turbine,  $\gamma_1$ 
  if  $r < E$  then
    Predict actual power production,  $\langle P \rangle_{tot} = \text{ANN}(\gamma_1, TI, \alpha)$ 
    loop
       $k \leftarrow k + 1$ 
       $\gamma_1^* \leftarrow$  random value,  $\in [0^\circ, 30^\circ]$ 
      Predict power production at  $\gamma_1^*$ ,  $\langle P \rangle_{tot}^* = \text{ANN}(\gamma_1^*, TI, \alpha)$ 
      if  $\langle P \rangle_{tot}^* > \langle P \rangle_{tot}$  then
        Move upwind turbine towards yaw angle  $\gamma_1^*$ 
      end if
    end loop
  end if
end loop

```

Table 3.6: The coefficients in the four stage cascaded low pass filter. The parameter s is defined as $s = \exp(-f_c \Delta t)$, where $f_c = 0.01$ Hz and $\Delta t = 21.6$ s, respectively.

Coefficient	Expression	Value
a_0	$(1 - s)^4$	1.4×10^{-3}
b_1	$4s$	3.2
b_2	$-6s^2$	-3.9
b_3	$4s^3$	2.1
b_4	$-s^4$	-4.2×10^{-1}

where y , x , and n denotes the output signal, input signal, and sample index, respectively. The coefficients a_0 and b_i are called recursion coefficients and their values are listed in Tab. 3.6. Typical filter responses are shown in Appendix A.1.2.

4 Results

In this chapter, the results are presented and discussed. First, the results from the calibration are addressed, where the aim is to tune the FAST.Farm solver such that it mimics the results of a Large-Eddy Simulation (LES). Afterwards, results from FAST.Farm are given for a steady and uniform flow, showing the potential of wake steering in ideal conditions. For the Artificial Neural Network (ANN), results from several FAST.Farm simulations are treated, mainly regarding the structural loads and wind farm total power output. These results are then used to train the ANN, and that process is described. Further, the success and challenges of using the ANN in Active Yaw Control (AYC) is demonstrated. An error analysis regarding all results is given as a final remark.

In all figures, the error bars signify a standard deviation with respect to a quantity measured in six turbulent realizations. The upwind turbine and the downwind turbine are referred to as WT1 and WT2, respectively.

4.1 Calibration

In this section, the results from twenty FAST.Farm simulations with varied parameters are systematically compared to the results from LES. The preferred wake tracking method is chosen and the optimal set of parameters are identified. Chiefly, FAST.Farm’s ability to mimic the LES predicted wake behaviour is prioritized. However, two structural responses are analysed as well, namely the torque and thrust exerted on the two wind turbines by the air.

4.1.1 Wake Tracking Methods

The three different wake tracking methods described in Section 3.3.2 are discussed here. Figure 4.1 displays the mean radial wake centre displacement (μ_{wake}) with respect to the hub position of the upstream wind turbine (WT1). For all three methods, it is shown that the radial displacement increases with downwind distance (x) with respect to the nearest upwind turbine. The increase in μ_{wake} is most likely due to the wake meandering, the wake centre position oscillates with time.

By comparing μ_{wake} at positions which differ $7D$ in distance (equal to the distance between WT1 and WT2), e.g. $x = 2D$ and $x = 9D$, it is clear that the mean radial wake centre displacement is greater downwind of WT2 than of WT1. A possible explanation for this is the merging of the two wakes. The zone of the greatest velocity deficits downwind of WT2 is influenced by the wake of WT1.

Regarding the three models, they predict similar results, however, Vollmer’s technique consistently predicts the lowest displacements. The fact that its predicted displacement is lower than that of the Gaussian method is consistent with the findings by Vollmer et al. [30]. Bastankhah’s model predicts almost an identical displacement as Vollmer’s model for the wake between WT1 and WT2 ($x \in [0D, 7D]$). However, downwind of WT2 ($x > 7D$), it predicts a greater μ_{wake} than any of the other models. This may be due to how the model is used. The magnitude of estimated velocity deficit according to the model decreases with x [70]. This distance is taken with respect to WT1. A more accurate use of the model may be to use the distance to the nearest upwind turbine.

Ultimately, the chosen wake tracking method is the Gaussian model, justified by the time series of the radial wake displacement (results omitted here). For Vollmer’s and Bastankhah’s respective model, the radial wake displacement fluctuates unrealistically. The position of the wake centre is expected to change continuously. Compared to the other models, this is captured to a greater degree by the Gaussian model, hence it is the preferred wake tracking method.

4.1.2 Calibration Error and Optimal Parameters

The wake quantities described in Section 3.3.1 are calculated for the LES, with the Gaussian wake tracking method, and given directly as outputs by FAST.Farm. As previously described, a calibration error Δ_{sim} is calculated for the 20 different sets of parameters listed in Tab. 3.2. As shown in Fig. 4.2, the set of parameters which correspond to the lowest Δ_{sim} is $MOD_{\text{meander}} = 3$ and $c_{\text{meander}} = 1.2$. The value of MOD_{meander} corresponds to FAST.Farm’s default value. However, the c_{meander} value is quite low as compared to the default value of 1.9. Lowering the c_{meander} increases the wake meandering effect in FAST.Farm.

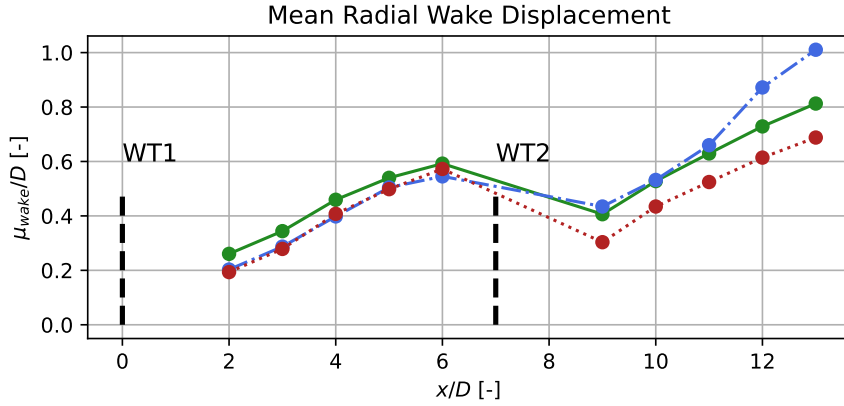


Figure 4.1: The temporally averaged radial displacement of the wake centre with respect to the upstream wind turbine’s hub position, as predicted by the three different wake tracking methods. (---) Position and radial blade span of wind turbines (WT) 1 and 2; (●---): Bastankhah; (●...): Vollmer; (●—): Gaussian.

As mentioned previously, the default parameter values in FAST.Farm have been derived from an extensive calibration procedure by Doubrawa et al. [46], for which the wake downwind of one wind turbine was studied. Compared to their study, the magnitude of Δ_{sim} in this work is roughly twice as high. One explanation for this discrepancy is the use of more extraction planes in this work.

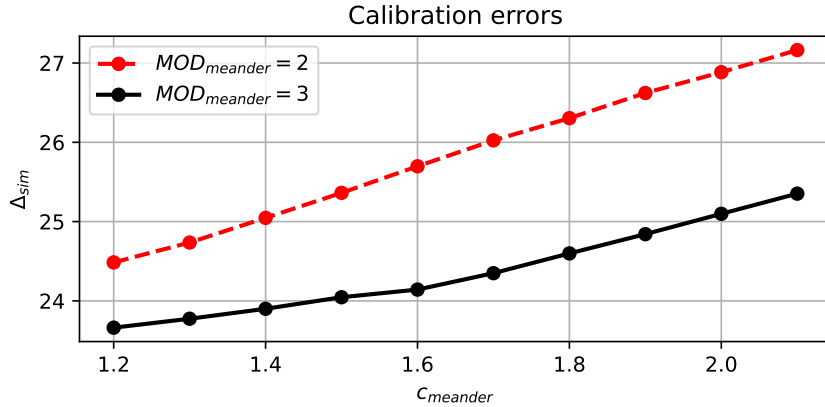


Figure 4.2: The calibration error (Δ_{sim}) as a function of the FAST.Farm parameters $c_{meander}$ and $MOD_{meander}$ which affect the wake dynamics calculations

Returning to the rather low value of $c_{meander}$, the discrepancy of it and the default value may be attributed to the wake merging downwind of WT2. As illustrated by LES results in Fig. 4.1, the wake merging seem to yield a positive offset in μ_{wake} . To account for this, $c_{meander}$ can be lowered (or $MOD_{meander}$ can be increased), as that will yield an increase in wake meandering and thus increase the radial wake centre displacement.

By excluding data downwind of WT2 and using data only from the planes at $2D \leq x \leq 6D$, i.e. the region where only WT1 affects the wake, the optimal $c_{meander}$ becomes 1.6, as shown in Fig. A.3a. This further suggests that it is the wake merging which cause the low value of $c_{meander}$.

4.1.3 Thrust and Torque Comparisons

As to not sacrifice FAST.Farm’s ability to predict other important quantities, in favour of accurately predicting wake behaviour, the temporally averaged torque and thrust exerted on the two wind turbines are compared to the LES results. As shown in Tab. 4.1, for both turbines, the thrust matches well for FAST.Farm and the LES. FAST.Farm predicts a slightly higher thrust, around 2% and 3% higher for WT1 and WT2, respectively. In contrast, there is substantial difference in predicted torque by FAST.Farm and the LES. According to

FAST.Farm, the torque is 9% and 16% higher than the LES results, for WT1 and WT2, respectively. This inconsistency may be, in part, due to the actuator disk model used in the LES. For both actuator disks, a constant rotor rotational speed is assumed, corresponding to a wind speed of 8 m s^{-1} . For the upwind turbine, this assumption is most likely valid. However, averaged over the WT2 rotor, the wind speed is lower, due to the wake. This leads to an erroneous estimation of the power coefficient (thus also the torque) and may contribute to the inconsistency observed between the LES and FAST.Farm results.

Table 4.1: The thrust and torque extracted from the LES and the FAST.Farm simulations. Turbine no. 1 and 2 denotes the upstream and downstream wind turbine, respectively.

Turbine no.	Solver	Torque (kN m)	Thrust (kN)
1	LES	1711	3624
	FAST.Farm	1864	3699
2	LES	1183	2824
	FAST.Farm	1375	2920

4.1.4 Evolution of Wake Quantities

The following is a description of the differences and similarities in how FAST.Farm and the LES predicts the wake quantities $\langle \delta V_x(x, r) \rangle$, $\langle \delta V_r(x, r) \rangle$, μ_{wake} , and σ_{wake} . For the LES results, the Gaussian wake tracking method is used exclusively.

Figure 4.3 illustrates the downwind evolution of the Probability Density Function (PDF) of the wake centre radial displacement, $f(r_{\text{wake}})$. From it, the mean and standard deviation of radial displacement (μ_{wake} and σ_{wake} , respectively) can be understood. As the downwind distance increases, so does μ_{wake} . This is exactly what was shown in Fig. 4.1. Likewise, σ_{wake} increases with x , as is understood from the widening of the fitted normal distributions. What is interesting to note is how well the FAST.Farm and LES results match. For the extraction planes at $2D \leq x \leq 6D$, the results are similar. However, for the planes downstream of WT2, ($x \geq 7D$), the predictions match poorly. There are two possible causes for the differences. First, the Gaussian wake tracking method might not be suitable for tracking merged wakes. For the Gaussian method, assumptions are made with regard to wake width and velocity deficits. These assumptions may have to be revised for the merged wake. Second, FAST.Farm may have some limitations in how the wake merging is modelled. As of writing, the wake merging is accounted for by adding velocity deficits in zones of wake overlaps [42]. Although velocity deficits are accounted for, it seems as if the wake centre position is not affected to a great degree by the wake merging.

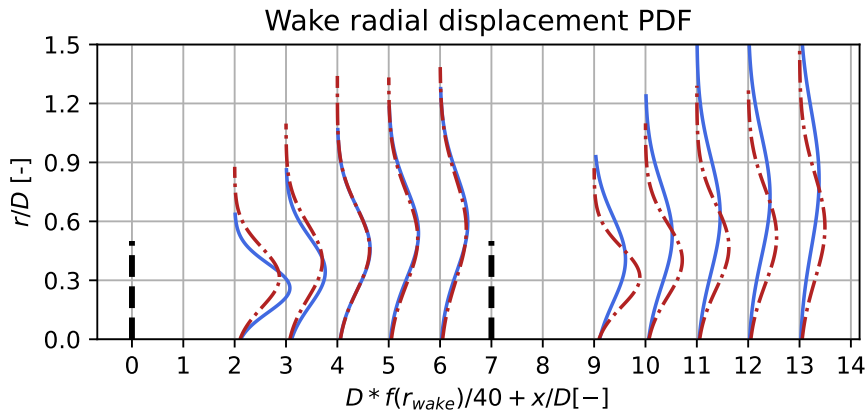


Figure 4.3: Streamwise evolution of fitted histograms of the radial wake centre displacement, relative to the hub position of WT1. (—): LES; (-.-): FAST.Farm; (-.-): Wind turbine positions and radial blade span.

In Fig. 4.4 the evolution of mean axial velocity deficit ($\langle \delta V_x \rangle$) is displayed. It is shown that the velocity

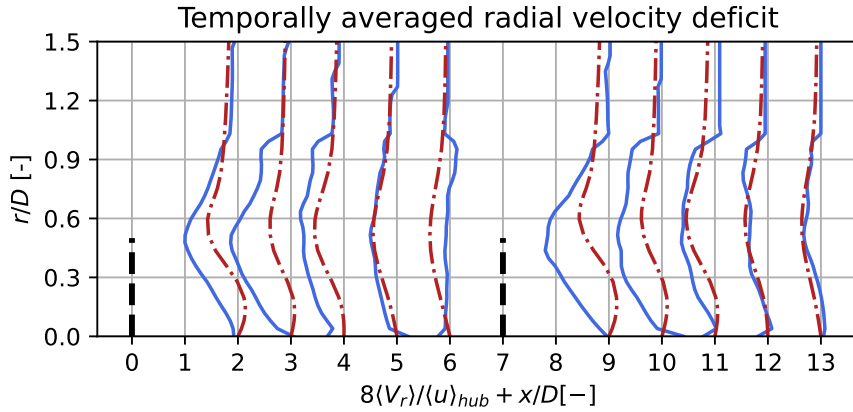


Figure 4.5: Streamwise evolution of the mean radial velocity deficit $\langle \delta V_r \rangle$. The radial distance (r) is with respect to the wake centre ($y_{\text{wake}}, z_{\text{wake}}$). (—): LES; (-.-): FAST.Farm; (- - -): Wind turbine positions and radial blade span.

any ambient turbulence to decay the velocity deficit of the wake or meander the wake, this wind condition should be ideal for wake steering and thus serve as an illustrative case for the potential of an active yaw controller. The results are from 13 FAST.Farm simulations, with WT1 in different yaw misalignments. As shown in Fig. 4.6a, the generated power by the individual wind turbines WT1 and WT2 depends on the yaw configuration of the upwind turbine. As the yaw angle of WT1 (γ_1) takes non-zero values, the power production of WT1 (P_1) decreases. The reason for this is, in part, that the swept area of the rotor decreases. As P_1 decreases, P_2 increases due to a smaller wake overlap with the WT2 rotor. As $|\gamma_1| \gtrsim 15^\circ$, P_2 stagnates, which likely means that the wake is completely deflected, as indicated by Fig. 4.7. Because of the stagnation in P_2 and continued decline in P_1 , there is a peak wind farm power production ($P_{\text{tot}} = P_1 + P_2$) to be gained by balancing the sacrifice in P_1 in favour of P_2 . Making such decisions is the main purpose of an active yaw control scheme. The ratio of P_{tot} at its peaks and at $\gamma_1 = 0^\circ$ is roughly 9%, which represents a potential gain in power production to be had from an AYC strategy.

In previous studies, it has been observed that the power coefficient (C_P) of a non-waked turbine depends on its yaw angle (γ) such that:

$$C_P(\gamma) = C_P(\gamma = 0^\circ)(\cos \gamma_1)^n, \quad (4.1)$$

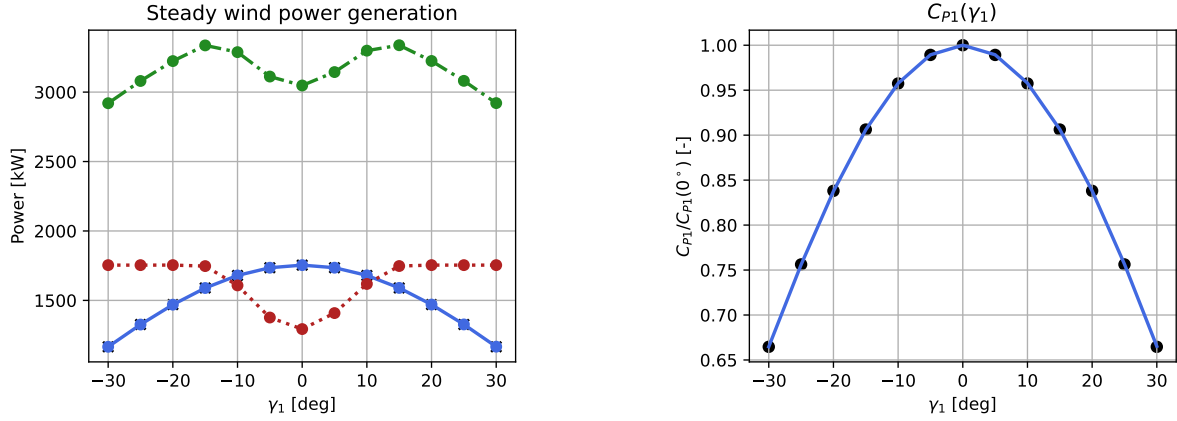
where it is shown in Fig. 4.6b that $n = 2.84$ fits the normalized power curve for WT1. The value of n corresponds fairly well with previous studies, which report exponents between $1.8 \leq n \leq 3$ [28, 41, 76].

4.3 Artificial Neural Network

The section below describes the results related to the Artificial Neural Network (ANN). The results are from 504 FAST.Farm simulations of different combinations of wind shear exponents, turbulence intensities, and WT1 yaw misalignments, using the calibrated parameters found in Section 4.1.2. First, the structural loads on the upwind wind turbine are presented. Second, the wind farm power production data which is used to train the neural network is shown. Finally, ANN predictions of optimal yaw angles and peak wind farm power production is presented. Results concerning the training of the neural network are covered in Sections A.2.4 and A.2.5.

4.3.1 Structural loads

Figures 4.8, 4.9, and 4.10 display the Damage Equivalent Load (DEL) for the blade root Out-Of-Plane (OOP) bending moment, yaw bearing moment, and tower base fore-aft bending moment, respectively, for the upwind turbine. In all figures, the error bars denote the standard deviation in DEL, using the results from 6 different turbulent realizations of each combination of α , TI , and γ_1 . For all load signals, it is shown that both the



(a) The individual and combined power output for the two wind turbines in steady and uniform flow, as predicted by FAST.Farm. (—●—): P_1 ; (●...●): P_2 ; (---●---): P_{tot}

(b) The dependence of C_{P1} on the yaw misalignment γ_1 . (—●—): C_{P1} ; (●...●): $(\cos(\gamma_1))^{2.84}$

Figure 4.6: Results from the simulations with steady uniform flow where the free stream velocity is $u_\infty = 8 \text{ m s}^{-1}$ and $\alpha = TI = 0$

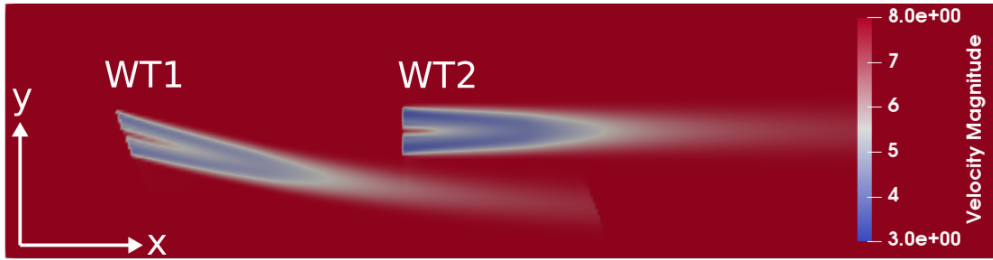


Figure 4.7: The two turbine case in steady uniform flow. WT1 is in the misaligned yaw $\gamma_1 = 20^\circ$, hence its wake is deflected from the downwind turbine, WT2.

turbulence intensity and wind shear increases the various damage equivalent loads. The corresponding loads for WT2 are found in Section A.2.6.

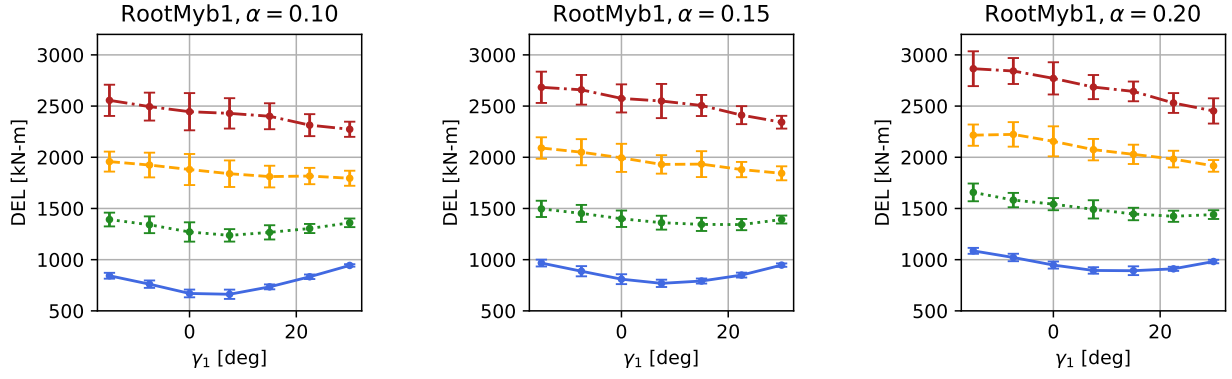
In terms of the yaw misalignment (γ_1) its impact on the DEL is of importance for this work. It is suggested by the results of Figs. 4.8a-4.8c, for the blade root OOP bending moment, that the DEL decreases with as the yaw misalignment increases. This is the main argument for why only positive yaw misalignments are optimized for in the proposed control algorithm 1. It is less costly to wake steer with a positive yaw misalignment than a negative, with respect to structural loads.

The observed trend of decreasing DEL is also quite consistent with the findings of Fleming et al. [10, 24]. However, there are deviations. In their work, they show that all positive yaw misalignments decrease the DEL for the blade root OOP bending moment, as compared to the case of $\gamma_1 = 0^\circ$. However, it is clear from the figures, FAST.Farm predicts an increase in the DEL for the positive yaw angles at low turbulence intensities. This may further suggest that FAST.Farm has issues with simulating low turbulence intensity cases.

Regarding the yaw bearing moment, similar observations can be made as of the blade root OOP bending moment, with regard to how well the results match existing literature. As seen in Figs. 4.9a-4.9c, the yaw misalignment dependency shifts as TI increases. For $TI = 5\%$, the DEL increases with γ_1 , but for $TI \geq 15\%$, it decreases. The latter case is consistent with previous work by Fleming et al. [24], but not the former.

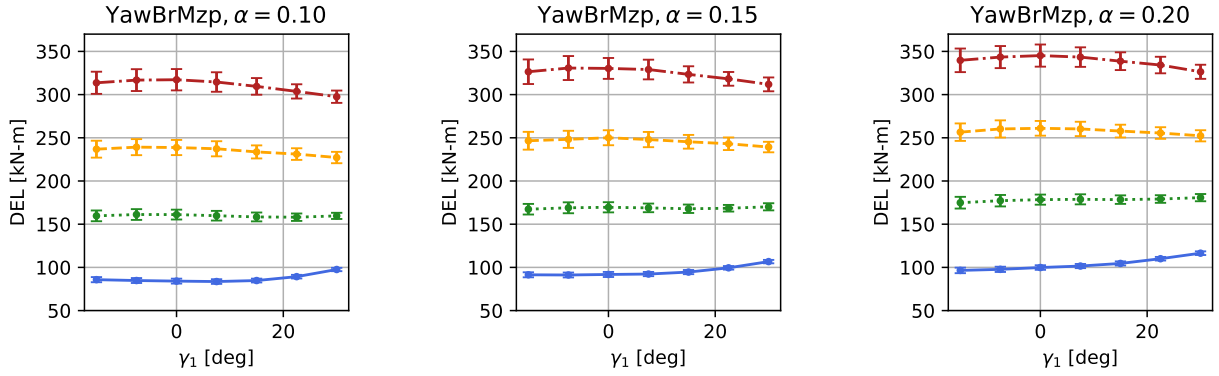
Lastly, the tower base fore-aft bending moment stays largely constant for $-15^\circ \leq \gamma_1 \leq 15^\circ$, but increases substantially for higher yaw misalignments. This is unexpected, and for which the reasons are unclear.

A striking feature of Figs. 4.8 -4.10, is the growth of the error bars as the turbulence intensity is increased. The error bars denote the standard deviation with respect to the relevant load (or quantity). As the loads are to a large degree affected by the fluctuations of the wind speed, it is natural that the error bars grow as the



(a) Blade root OOP bending moment for wind shear exponent $\alpha = 0.10$ (b) Blade root OOP bending moment for wind shear exponent $\alpha = 0.15$ (c) Blade root OOP bending moment for wind shear exponent $\alpha = 0.20$

Figure 4.8: The blade Out-Of-Plane (OOP) bending moment DEL for WT1, as a function of the upwind turbine's yaw (γ_1) for different wind shear exponents (α) and turbulence intensities (TI). (—): $TI = 5\%$; (····): $TI = 10\%$; (---): $TI = 15\%$; (-·-·): $TI = 20\%$.



(a) Yaw bearing moment for wind shear exponent $\alpha = 0.10$ (b) Yaw bearing moment for wind shear exponent $\alpha = 0.15$ (c) Yaw bearing moment for wind shear exponent $\alpha = 0.20$

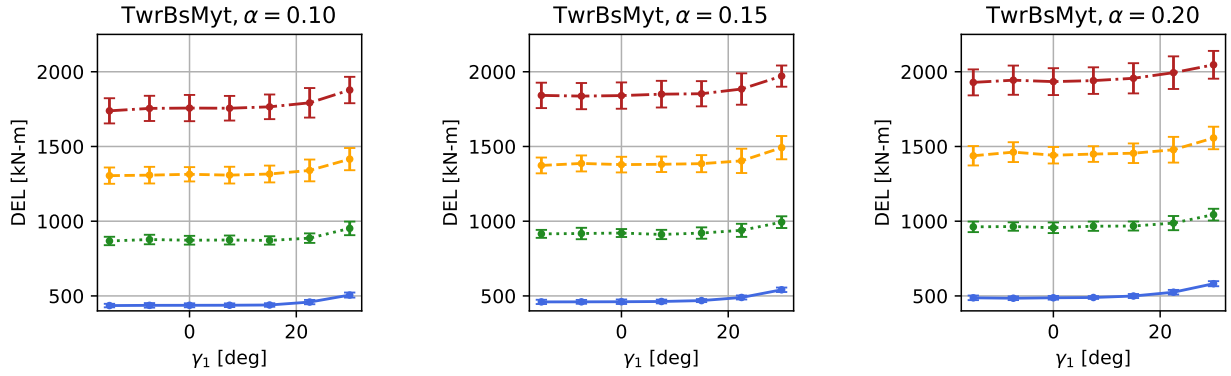
Figure 4.9: The yaw bearing moment DEL for WT1, as a function of the upwind turbine's yaw (γ_1) for different wind shear exponents (α) and turbulence intensities (TI). (—): $TI = 5\%$; (····): $TI = 10\%$; (---): $TI = 15\%$; (-·-·): $TI = 20\%$

turbulence intensity is increased.

4.3.2 Wind Farm Power Production

Figures 4.11a-4.11c show the temporally averaged wind farm power output ($\langle P \rangle_{\text{tot}}$) as a function of α , TI , and γ_1 . The error bars denote the standard deviation in $\langle P \rangle_{\text{tot}}$ with respect to the turbulent random seeds. For the low turbulence intensity case of $TI = 5\%$, the power production curve is similar to that of the steady uniform case shown in Fig. 4.6a, with peaks in $\langle P \rangle_{\text{tot}}$ for $15^\circ \leq \gamma_1 \leq 22.5^\circ$, depending on the wind shear exponent. On the whole, $\langle P \rangle_{\text{tot}}$ seem to decrease only slightly as α is increased. The likely explanation for this is that the bulk velocity decreases marginally with wind shear, as shown in Fig. A.10.

With regard to the turbulence intensity, as it is increased, the prospects of wake steering diminish, as the yaw angle corresponding to the peak power production shifts towards $\gamma_1 = 0^\circ$. For the high turbulence case of $TI = 20\%$, any attempt to wake steer by yaw misalignment should reduce $\langle P \rangle_{\text{tot}}$. Qualitatively, these results are consistent with those of Vollmer et al. [30], who uses Large-Eddy Simulations to show that the horizontal wake deflection is dependent on atmospheric wind conditions such as turbulence intensity, and suggests that yaw misalignment may not be a feasible approach for high TI . The same conclusions can be made here. The



(a) Tower base fore-aft moment for wind shear exponent $\alpha = 0.10$ (b) Tower base fore-aft moment for wind shear exponent $\alpha = 0.15$ (c) Tower base fore-aft moment for wind shear exponent $\alpha = 0.20$

Figure 4.10: The tower base fore-aft bending moment DEL for WT1 as a function of the upwind turbine’s yaw (γ_1) for different wind shear exponents (α) and turbulence intensities (TI). (—): $TI = 5\%$; (····): $TI = 10\%$; (---): $TI = 15\%$; (-·-·): $TI = 20\%$.

reasons why are likely that the high ambient turbulence exaggerates the wake meandering to such a degree that wake deflection becomes meaningless and that the wake recovers to free stream conditions more quickly.

Regarding the optimal γ_1 , corresponding to the maximum $\langle P \rangle_{\text{tot}}$, its value is slightly lower than expected. In their work, Fleming et al. [10] show that for $TI \approx 5\%$, the optimal yaw misalignment is $\gamma_1 = 25^\circ$. A possible explanation for this inconsistency is the lack of a wake curl model in the current version of FAST.Farm. The curling of the wake has been shown to cause the observed kidney-shape of the mean wake [26]. It is possible that such a shape would increase the wake overlap with the downwind turbine as compared to an elliptical shape, which is the wake profile in FAST.Farm [42]. Furthermore, the low value of c_{meander} could influence the optimal γ_1 , as lowering the parameter increases the wake deflection, i.e. a lower yaw misalignment can cause a sufficient wake deflection to maximize power production.

In the case of $\langle P \rangle_{\text{tot}}$, previous work have shown that it has an asymmetric dependence on γ_1 [10, 41], such that it increases and decreases with positive and negative yaw angles, respectively. For low TI , this type of dependence is seemingly absent, as shown in Figs. 4.11a-4.11c. An explanation may be the low c_{meander} , which allows the wake to be more easily deflected, such that it overcomes the deflection caused by the torque exerted on the air by the rotor blades, which is the cause of the asymmetry [29]. However, for higher TI (15-20%), there is indeed a slight asymmetry. Again, this could suggest that FAST.Farm provides more reliable results for high turbulence cases.

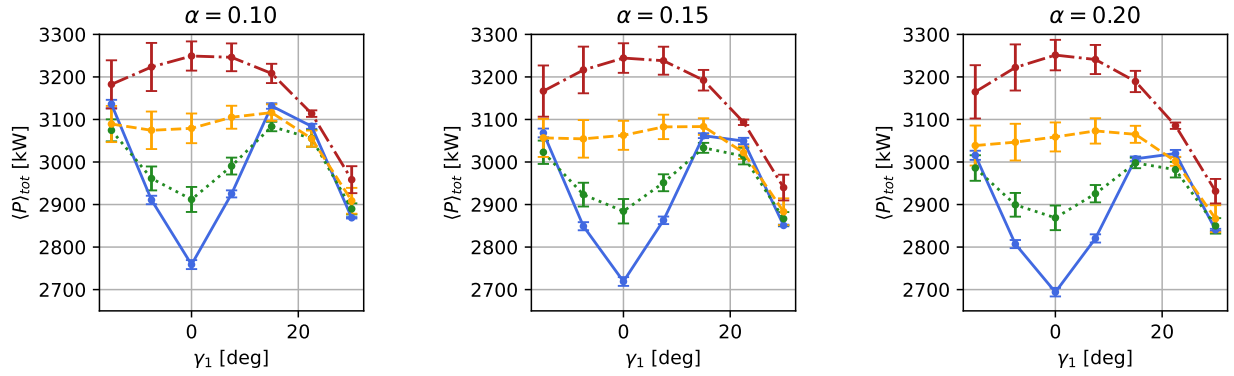
The ratio of the peak $\langle P \rangle_{\text{tot}}$ and $\langle P \rangle_{\text{tot}}(\gamma_1 = 0^\circ)$ can be seen as the potential power production gain to be had from implementing an active yaw controller. In Tab. 4.2 the potential gains for all wind conditions are compiled. It is calculated as

$$Q_{\text{potential}} = \frac{\text{mean}(\langle P \rangle_{\text{tot, peak}}) \pm \text{std}(\langle P \rangle_{\text{tot, peak}})}{\text{mean}(\langle P \rangle_{\text{tot, 0}}) \mp \text{std}(\langle P \rangle_{\text{tot, 0}})} - 1, \quad (4.2)$$

where $\langle P \rangle_{\text{tot, 0}}$ denotes the total power at $\gamma_1 = 0^\circ$, and $\langle P \rangle_{\text{tot, peak}}$ the peak total power. As seen in Fig. 4.11, the potential power gains are the largest in low turbulence conditions. What is interesting to note is that the $Q_{\text{potential}}$ decreases as the wind shear (α) increases, which suggests that uniform wind is a beneficial condition for yaw controlled wake steering.

4.3.3 Optimal Yaw Misalignments

The output of the trained ANN is the mean total power of the wind farm, i.e. $\langle P \rangle_{\text{tot}} = \langle P_1 \rangle + \langle P_2 \rangle$. Figure 4.12a displays the ANN-predicted peak power ($P_{\text{tot, peak}}$) as a function of the shear exponent (α) and the turbulence intensity (TI). In Fig. 4.12b, the corresponding optimal yaw ($\gamma_{1, \text{peak}}$) is shown. By comparing Fig. 4.12 to Fig. 4.11, it is suggested that the ANN successfully captures the trends in the training data. For instance, as is understood from Fig. 4.11, increasing α slightly decreases $\langle P \rangle_{\text{tot}}$. Likewise, this is predicted by the ANN, as shown in 4.12b. Moreover, as has been previously discussed, the prospect of wake steering



(a) Wind farm power output for shear exponent $\alpha = 0.10$ (b) Wind farm power output for shear exponent $\alpha = 0.15$ (c) Wind farm power output for shear exponent $\alpha = 0.20$

Figure 4.11: The temporally averaged wind farm power output ($\langle P \rangle_{\text{tot}} = \langle P_1 \rangle + \langle P_2 \rangle$) as a function of the upwind turbine's yaw (γ_1) for different wind shear exponents (α) and turbulence intensities TI (—): $TI = 5\%$; (····): $TI = 10\%$; (- - -): $TI = 15\%$; (- · - ·): $TI = 20\%$.

Table 4.2: The relative potential wind farm power production gain ($Q_{\text{potential}}$) for twelve different wind conditions.

α	TI	$Q_{\text{potential}}$
[-]	[%]	[%]
0.10	5.0	13.7 ± 0.8
	10.0	5.9 ± 1.5
	15.0	1.2 ± 1.8
	20.0	0.0 ± 2.1
0.15	5.0	12.8 ± 0.8
	10.0	5.2 ± 1.5
	15.0	0.7 ± 1.8
	20.0	0.0 ± 2.1
0.20	5.0	12.1 ± 0.7
	10.0	4.5 ± 1.5
	15.0	0.5 ± 2.1
	20.0	0.0 ± 2.2

decreases as turbulence intensity is increased. This is indeed reflected by Fig. 4.12b, as the optimal yaw goes to zero for high TI .

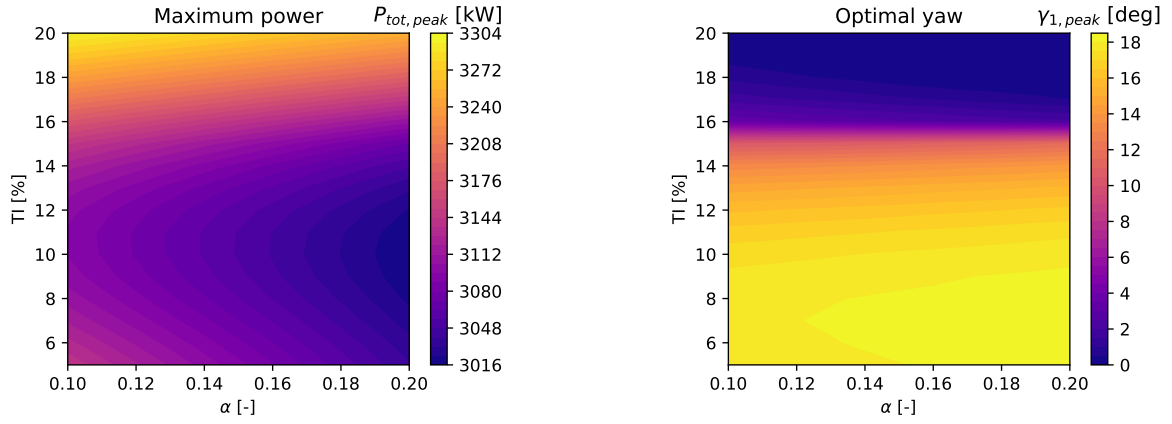
It is interesting to note that the peak power in Fig. 4.12a is slightly higher than the corresponding peaks in Fig. 4.11. This discrepancy may be due to how the neural network is ultimately chosen and which data it is trained with. The chosen neural network is the one which yielded the lowest validation error. It is plausible that the validation set in question contained data points with unusually high $\langle P \rangle_{\text{tot}}$ values.

4.4 Active Yaw Control

In the following section, the results from 144 FAST.Farm simulations are presented, of which half are made with the active yaw controller (AYC) described in Section 3.5. In the other half of simulations, a greedy control algorithm is employed, in which both wind turbines seek to maximize individual power production, i.e. their rotor planes are perpendicular to the mean wind direction, such that $\gamma_1 = \gamma_2 = 0^\circ$.

4.4.1 Trained Wind Conditions

Below are ratio comparisons of the AYC scheme to the greedy control scheme in wind conditions for which the artificial neural network is trained, i.e. those introduced in Section 4.3.2.



(a) The ANN predicted maximum power

(b) The ANN predicted optimal yaw misalignment

Figure 4.12: The predicted maximum wind farm generated power ($\langle P \rangle_{tot, peak}$) (left) and the corresponding optimal yaw misalignment for the upwind wind turbine ($\gamma_{1, peak}$) (right) as functions of the wind shear exponent (α) and turbulence intensity (TI)

Figure 4.13 illustrates the ratio of temporally averaged wind farm power production for the AYC case ($\langle P \rangle_{tot, AYC}$) and the greedy control scheme case ($\langle P \rangle_{tot, greedy}$). The error bars indicate the standard deviation, with respect to 6 turbulent seeds. It is shown that, for $TI = 5\%$, the increase in wind farm power production can be increased by roughly 5%-6%, depending on α . Moreover, as turbulence intensity is increased, the benefit of using the active yaw controller is lessened. At $TI = 10\%$, there is a mean increase in power production of around 1%, however, as is indicated by the error bars, there is a risk that using the AYC decreases the wind farm power production, relative to the corresponding case with the greedy control scheme. In fact, when $TI = 15\%$ the active yaw controller reduces the wind farm power production. However, the error bars suggest that the AYC can be beneficial even then. Lastly, for $TI = 20\%$, the AYC yields a very slight reduction in power production.

Regarding the wind shear (α) it is seen in Fig. 4.13 that the benefit of using an AYC decreases as α increases. The reasons for this have previously been discussed regarding Tab. 4.2. A reason for why the AYC does not yield the full potential power gain (which are listed in Tab. 4.2) is that the mean power is calculated from the moment that the AYC is activated, as is indicated by the black dashed line in Fig. 4.14. This includes an interval in time when the upwind turbine yaws its rotor and the wake subsequently adapts to the new yaw misalignment. In Fig. 4.14b it is seen that it is not until $t \approx 1600$ s that the AYC seems to yield an increase in power. That suggests that it takes roughly 400 s for the rotor to yaw and for the wake to subsequently develop. This wake development time is roughly twice as high compared to findings of previous work [10, 41]. A likely reason for this inconsistency is the default value of a FAST.Farm wake dynamics parameter called f_c which affects the wake development time. Since the release of FAST.Farm, the default value of f_c has been found (by NREL) to be much too low, and it has been observed that increasing it can give wake development times more in line with previous studies.

Moving on to consider the effect of turbulence intensity, it is suggested by Tab. 4.2 that there is indeed a potential for increasing the wind farm power production by employing an AYC, even for high turbulence intensities such as $TI = 15\%$. Regardless, as has been shown here, and contrary to the preferred outcome, the AYC instead decreases power production at $TI = 15\%$. A likely explanation for this is the way that the TI is estimated within the AYC. The estimated TI is a low-pass filtered signal and depends on the low-pass filtered horizontal wind velocity. As such, it has been observed to vary significantly with time. To understand why no gain in wind farm power is achieved, see Fig. 4.12b, which shows the ANN-predicted optimal yaw misalignments. In the interval $10\% \leq TI \leq 18\%$, there is a rapid transition of the optimal yaw, from $\gamma_{1, best} = 18^\circ$ to $\gamma_{1, best} = 0^\circ$. For example, if the low-pass filtered estimation of $TI = 15\%$ fluctuates with, e.g. $\Delta TI = 5\%$, the AYC commands WT1 to a suboptimal yaw misalignment. In contrast, if the same fluctuations happen when e.g. $TI = 5\%$, the ANN prediction of the optimal yaw misalignment remains unchanged.

To further support the claim that the estimated TI fluctuates, see Fig. 4.15a which shows the time series of

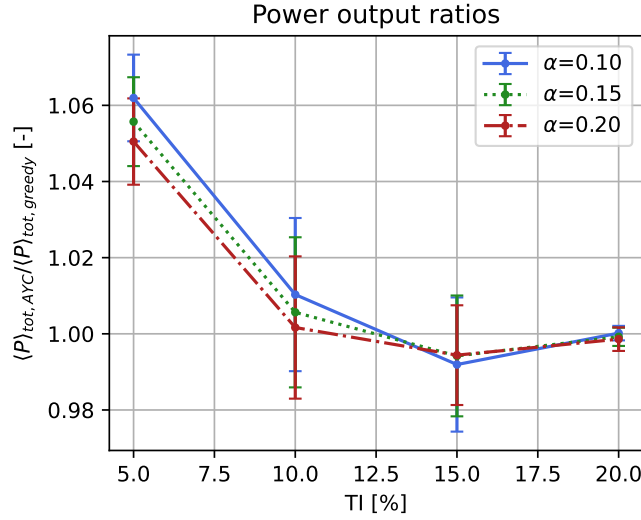


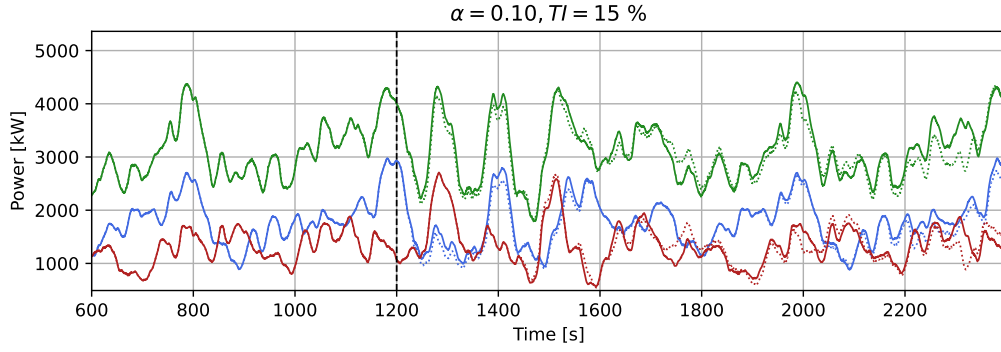
Figure 4.13: The ratio of mean wind farm power production in various wind conditions, utilizing two different control schemes. $\langle P \rangle_{\text{tot,AYC}}$ and $\langle P \rangle_{\text{tot,greedy}}$ denotes the mean power production for the wind farm with an active yaw controller, and for the wind farm utilizing the greedy control scheme, respectively.

yaw misalignment for a $TI = 15\%$ case. The corresponding power production time series is seen in Fig. 4.14a, which illustrates clearly that the wind farm power production does not increase with the activation of the AYC, and the γ_1 time series show that the yaw misalignment changes with time, despite the wind conditions being unchanged. This suggests that the estimation of TI varies, otherwise the output of the ANN would not vary. Further, because γ_1 changes repeatedly, the wake likely never fully develops, and thus can not be steered away from the downwind turbine to increase the wind farm power production.

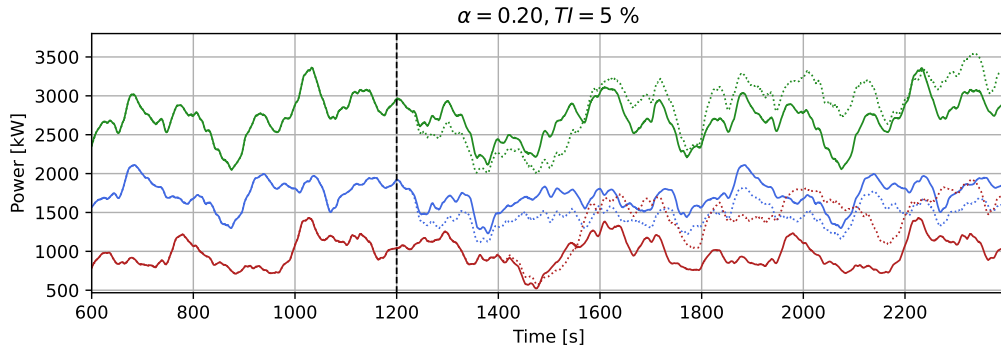
To investigate the AYC's effect on structural loads, ratios are calculated for the blade root Out-Of-Plane (OOP), yaw bearing, and tower base fore-aft bending moments. The ratios are with respect to the damage equivalent loads corresponding to cases with and without the AYC. Figures 4.16 and 4.17 show the ratios for the upwind and downwind turbine, respectively. For the case of upwind turbine, it is suggested that the AYC increases the three loads at hand in cases of low turbulence ($TI = 5\%$), but not in higher turbulence. As seen in Fig. 4.16a, the increase for the blade root OOP loads varies quite a bit depending on α and reaches up to 20% for low wind shear ($\alpha = 0.10$). Figure 4.16c show that, for the tower base fore-aft moment, the increase is roughly 10% in low turbulence, but it quickly goes to zero as TI increases. As shown by Fig. 4.16b, the yaw bearing moment DEL is greatly increased with the use of the AYC. Depending on the wind shear exponent, it is roughly 5-7 times higher when the AYC is used, as compared to cases without the AYC. This large increase in loads is likely due to the AYC-demanded yaw manoeuvring, and the optimal yaw angles are larger in low turbulence than in cases of high turbulence (as indicated by Fig. 4.12b).

For the downwind turbine (WT2), the damage equivalent load, with respect to the blade root OOP bending moment, increases roughly the same as for WT1, with the AYC, as shown by Fig. 4.17a. However, in contrast to the corresponding results for WT1 (see Fig. 4.16a), the wind shear exponent dependency is different. For WT2, larger wind shear cause greater loads, which is not the case for WT1. Regarding the yaw bearing moment, the use of the AYC seems to slightly decrease the DEL in cases of low turbulence, as shown by 4.17b. Figure 4.17c shows that the DEL for the tower base fore-aft bending moment is increased with roughly 20% when $TI = 5\%$ for the three wind shear exponents.

Except for the yaw bearing moment DEL for WT2, the above observations indicate that the structural loads generally increase with the use of the AYC for both wind turbines in cases of low turbulence. For higher turbulence, there is hardly any difference in loads with and without the AYC. It is expected that the use of the AYC reduces the loads for WT2, as the wake will be deflected away from it and thus reduce the associated increased turbulence of the wake. This is only observed for the yaw bearing moment, but not for the tower base fore-aft and blade root OOP bending moments. A likely explanation for this discrepancy is that FAST.Farm does not currently incorporate the wake-added turbulence [42]. For the upwind turbine, as was discussed in

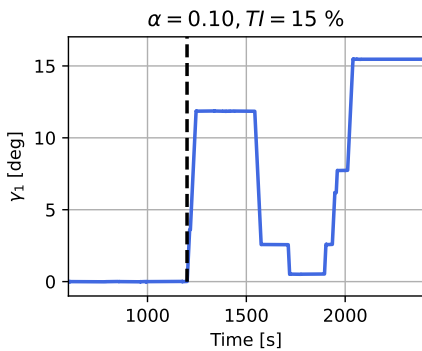


(a) The power production time series for a high turbulence intensity case. The AYC yields no increase in power production.

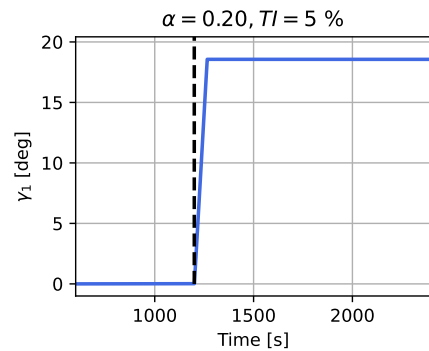


(b) The power production time series for a low turbulence intensity case. The AYC successfully increases power production.

Figure 4.14: The individual and summed turbine power production time series in two different wind conditions. For both wind conditions, the power is plotted for a greedy yaw control scheme ($\gamma_1 = 0^\circ$) and an active yaw control scheme. In the low turbulence intensity case, the AYC seems to increase power, but not in the higher turbulence intensity case. (---): Yaw control activation time; (—): $P_{\text{tot,greedy}}$; (····): $P_{\text{tot,AYC}}$; (—): $P_{1,\text{greedy}}$; (····): $P_{1,\text{AYC}}$ (—): $P_{2,\text{greedy}}$; (····): $P_{2,\text{AYC}}$



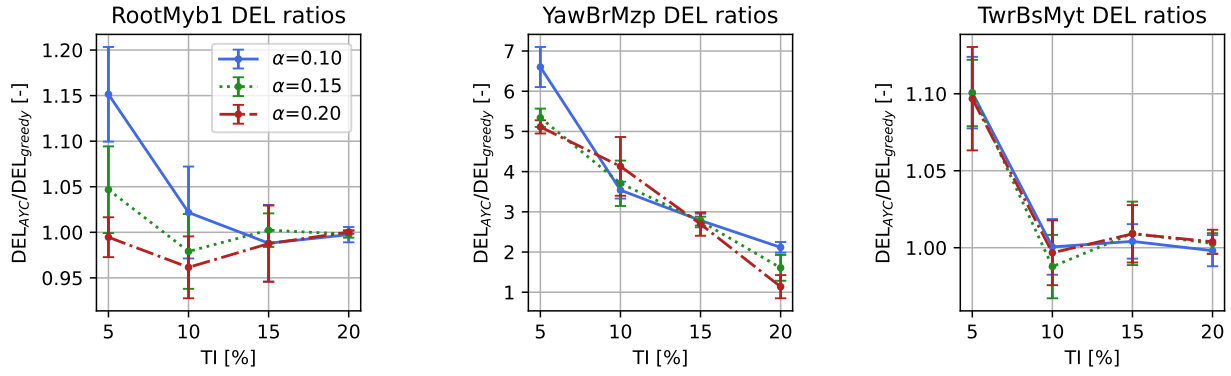
(a) Unwanted yaw misalignment response. Medium turbulence intensity case.



(b) Ideal yaw misalignment response. Low turbulence intensity case.

Figure 4.15: The time series for the AYC-commanded yaw misalignment (γ_1) corresponding to the cases presented in Fig. 4.14. (---): Yaw control activation time; (—): $\gamma_1(t)$

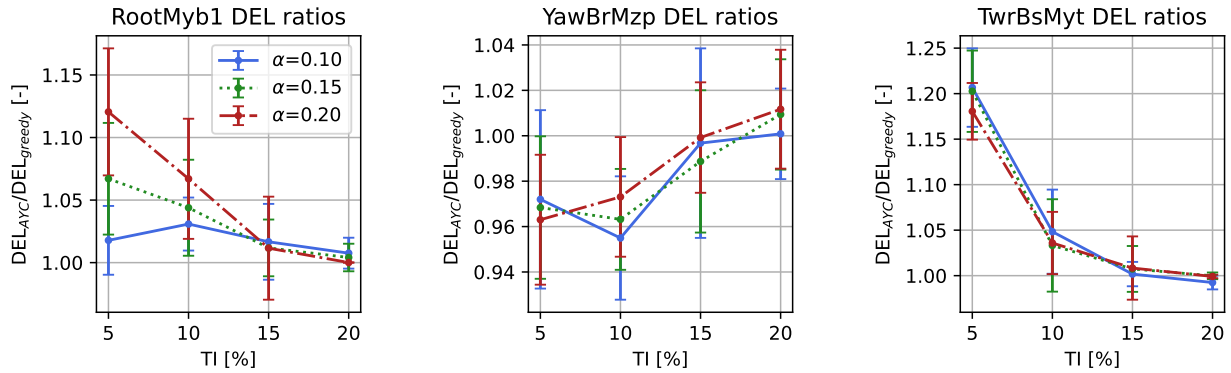
Section 4.3.1, the loads are expected to decrease, as the AYC commands yaw misalignments for WT1. This is not observed, and can be due to FAST.Farm's suspected suboptimal performance in low turbulence conditions.



(a) Load ratios for WT1 with respect to the blade root out-of-plane bending moment (b) Load ratios for WT1 with respect to the yaw bearing moment (c) Load ratios for WT1 with respect to the tower base fore-aft bending moment

Figure 4.16: The ratio of various damage equivalent loads for WT1 (the upwind turbine) in cases with and without active yaw control, denoted by DEL_{AYC} and DEL_{greedy} respectively.

In summary, for both turbines, the results regarding the yaw bearing moment match prior expectations better than the results regarding tower base fore-aft and blade root OOP bending moments.



(a) Load ratios for WT2 with respect to the blade root out-of-plane bending moment (b) Load ratios for WT2 with respect to the yaw bearing moment (c) Load ratios for WT2 with respect to the tower base fore-aft bending moment

Figure 4.17: The ratio of various damage equivalent loads for WT2 (the downwind turbine) in cases with and without active yaw control, denoted by DEL_{AYC} and DEL_{greedy} respectively.

4.4.2 Untrained Wind Conditions

As a final demonstration, it is of interest to see how the AYC performs when the ANN have to interpolate and extrapolate $\langle P \rangle_{tot}$ for wind conditions it has not been trained with. The results are based on 12 simulations for two wind conditions, with 6 turbulent realizations each. In the interpolated case, $\alpha = 0.12$ and $TI = 8\%$. In the extrapolated case, $\alpha = 0.17$ and $TI = 25\%$. Table 4.3 lists the ratio of various quantities for the wind farm with AYC enabled, and those with a greedy control scheme. Similar observations can be made as in Section 4.4.1. In low turbulence, total wind farm power can be gained from the AYC, with the cost of increased yaw bearing moment and root blade OOP bending moment. Tower base-fore aft bending moment remains essentially constant. For the high turbulence case, the AYC tries to mimic the greedy case, but some loads are increased, likely because the AYC induce manoeuvring due to erroneous TI estimations. These results suggest that the AYC can indeed be used in both interpolated and extrapolated wind conditions.

Table 4.3: Mean ratios of various quantities for the upwind turbine with and without the AYC. $Q_{\langle P \rangle}$, Q_{RootMyb1} , Q_{YawBrMzp} , Q_{TwrBsMyt} denote the ratio of total wind farm power production, blade root OOP bending moment DEL, yaw bearing moment DEL, tower base fore-aft bending moment DEL, respectively. The uncertainties indicate the standard deviations in the calculated ratios.

α	TI	$Q_{\langle P \rangle}$	Q_{RootMyb1}	Q_{YawBrMzp}	Q_{TwrBsMyt}
[-]	[%]	[-]	[-]	[-]	[-]
0.12	8	1.0355 ± 0.0041	1.0561 ± 0.0459	4.1799 ± 0.9951	1.0050 ± 0.0828
0.17	25	0.9981 ± 0.0035	1.0020 ± 0.0026	1.1985 ± 0.2062	0.9993 ± 0.0062

4.5 Error Analysis

There are a number of decisions and aspects of this work which require scrutiny to assess the reliability of the results. First, the spatial discretization of the TurbSim-generated synthetic inflow may have influenced the results. For all FAST.Farm simulations, the available spatial resolution of the synthetic inflow was equal to the low-resolution FAST.Farm domains. A discretization sensitivity study made by Shaler et al. [45] show quantitatively the effect of using a coarser grid than recommended. By their findings, it is suggested that the spatial resolution used for this study does not yield errors greater than 1% for the blade root OOP bending moment, the generated power, and the yaw bearing moment. However, for the tower base fore-aft bending moment (see Fig. 4.10), the chosen spatial resolution can not guarantee errors lower than 2%. In contrast, for the low-resolution domains, the spatio-temporal resolutions are in accordance with the guidelines provided in [42] and [45], thus there is no reason to suspect any discretization-related errors larger than 1% for the FAST.Farm-predicted wake dynamics.

An impactful decision of this work was the choice of planes to use in the calibration of c_{meander} . The inclusion of the downwind planes of WT2 means that FAST.Farm was calibrated such that the wake quantities (radial wake centre displacement and velocity deficits) downwind of both turbines are as close to the LES results as possible. However, because a focus of this study is the wake effect between the two turbines and its impact on wind farm power production and structural loads, the wake behaviour between the turbines is arguably more important than the wake behaviour downwind of WT2. It has been shown that excluding the WT2 downwind planes from the calibration procedure changes the optimal c_{meander} (see Fig. A.3a). Without a c_{meander} sensitivity study, it is difficult to quantify its effect. Regardless, various observations throughout this work (omitted in this report) suggests that tuning the parameter has indeed an effect on the wake deflection, and thus the choice of c_{meander} likely have an effect on the subsequent results based on the FAST.Farm simulations. In hindsight, better results would likely have been achieved with the exclusion of the WT2 downwind extraction planes.

Continuing on the note of the calibration, the reliability of the results could have been improved by a more extensive calibration procedure. In this work, a LES was performed with the following wind farm conditions: $\alpha = 0.109$; $TI = 10\%$; and $\gamma_1 = 0^\circ$. In contrast, in training the ANN, FAST.Farm was used to simulate 84 unique operating conditions. A more comprehensive calibration, including results from numerous LES with a wide range of wind farm conditions, could yield other parameter values for c_{meander} and MOD_{meander} . Moreover, FAST.Farm have 20 tunable parameters, it is likely that the results could have been improved if more of them were included in the calibration. The inclusion of more parameters could have relaxed the need to lower c_{meander} to accommodate the apparent wake centre displacement offset speculated to be caused by the wake merging. As has been already discussed, the choice of parameters have ramifications for the FAST.Farm results, but it is difficult to assess exactly how the results would change with a more extensive calibration.

The use of synthetic ambient wind is also something that may have influenced the results. It has drawbacks, such as not being able to capture wind farm-wide turbulent length scales. And it is unclear what impact on the results the specific choice of synthetic turbulence method (IEC Kaimal) has.

5 Conclusions

In this work, it has been shown that an Artificial Neural Network (ANN) can be used in conjunction with an Active Yaw Control (AYC) scheme to enhance the power production of a two-turbine wind farm. The data generation and subsequent training of the ANN was made feasible with FAST.Farm, which allows for a wide range of wind farm operating conditions to be simulated due to its low computational cost.

With regard to the calibration of FAST.Farm, it has been shown that the optimal parameters depend on what approach is taken. In this work, the wake of the downwind turbine was included in the calibration, and this decision was shown to yield a lower c_{meander} than if that wake had been excluded. This is likely because the wake centres are unaffected by the merging of the two wakes in FAST.Farm. In contrast, the wake centre, as derived from the LES results with the SAMWICH wake tracking toolbox, is affected by the merging of the wakes. The low c_{meander} likely affected the results by exaggerating the deflection of the wakes, for any given yaw angle. On the note of wake tracking methods, the results suggest that the three models here called Vollmer, Gaussian, and Bastankhah yields similar predictions of the mean wake centre radial displacement, which was seen to increase with downwind distance with respect to the closest upwind turbine due to wake meandering. The Gaussian wake tracking method was preferred due to it predicting a more continuous time series of wake centre displacement compared to the other models. It was suggested that Bastankhah's model may have been improperly applied to the wake of the downwind turbine, causing it to predict too large displacements. Further, it is thought that the use of a 1D actuator disk in the LES had some impact, mainly on qualitative behaviour of the mean axial velocity deficit. Lastly, the radial velocity deficit was shown to be the main contributor of the calibration error.

Considering the artificial neural network, it was demonstrated that it can be used to predict the wind farm power production by training it with temporally averaged data from FAST.Farm simulations. Results suggest that the chosen ANN may slightly overestimate $\langle P \rangle_{\text{tot}}$ for some operating conditions. However, this minor flaw was thought not to cause any issues in its application. Regarding the data which was used to train the ANN, it was shown to qualitatively agree better with previous studies in cases of high turbulence intensity (TI). For instance, certain expected asymmetries with respect to the yaw angle were either absent or less prominent at low TI , as compared to high TI . Specifically, $\langle P \rangle_{\text{tot}}$ did not show a clear asymmetry, and neither did the blade root out-of-plane bending moment Damage Equivalent Load (DEL). It is believed that FAST.Farm's lack of accuracy in low TI cases coupled with the low value of c_{meander} could explain these deviations from previous studies. On the other hand, in accordance with previous work, the ratio of peak power production and power production with $\gamma_1 = 0^\circ$ ($Q_{\text{potential}}$) decreased as TI increased, suggesting that free stream conditions are retained more quickly in cases of high turbulence. In high turbulence, the prospect of wake steering is diminished, which is thought to be due to the intensified wake meandering. Moreover, the potential power gain to be had from an AYC was shown to decrease with increases in the wind shear exponent (α), for any given level of TI . With respect to various DELs on the upwind turbine, it was observed to increase with increases in both TI and the wind shear α .

Regarding the AYC, its implementation was partially successful. It was shown that it can be used to increase $\langle P \rangle_{\text{tot}}$ by 5-6 % when the turbulence intensity is low. However, there are unsolved issues regarding its performance when $10 \leq TI \leq 15\%$. It was argued that this is due to the current inability to maintain a stable estimation of the mean TI in such cases. The estimated TI is a low-pass filtered signal and thus varies in time. This varying leads the AYC to take suboptimal decisions because the ANN predicts power production for operating conditions which are not precisely estimated. Moreover, it is shown that in cases of low turbulence, the AYC increases the damage equivalent loads on both the upwind turbine and downwind turbine with respect to the blade root out-of-plane bending moment and tower base fore-aft moment up to 20 %, depending on the wind shear. Regarding the yaw bearing moment, the AYC greatly increases the DEL for the upwind turbine (up to 7 times) and slightly lowers it for the downwind turbine (roughly 5 %).

6 Future work

There are many aspects of this work which can be improved or extended. For instance, to make the FAST.Farm results more reliable, efforts should be directed towards enhancing the calibration procedure. The most straightforward way to do this is to simply include more FAST.Farm wake dynamics parameters in the grid search of optimal parameters. For instance, there are parameters which control the offset of the wake centre's radial displacement downwind of the turbines. Tuning such parameters are thought to better match the FAST.Farm results to the LES results. Moreover, the wake tracking process may be enhanced by running a precursor high fidelity simulation (e.g. a LES) of the atmospheric boundary layer, without the influence of any wind turbines. Doing this would allow the velocity deficits to be more accurately calculated, which, as of now, are calculated using a power law estimation of the free stream velocity. With a precursor run, it is thought that the wake properties can be more readily identified, as the comparison of waked and non-waked flow will be more accurate. Furthermore, a precursor can facilitate the process of generating the FAST.Farm inflow, and can also be used as boundary conditions in a subsequent LES including the wind turbines. As to further enhance the calibration, additional high fidelity simulations could be conducted to cover a wider range of operating conditions. In addition, to capture more complex wake phenomena, such simulations could utilize an actuator line model, rather than the selected actuator disk model. However, the downside of performing high fidelity precursor runs is their added computational costs.

Regarding the FAST.Farm results, and mainly those relating to the wind turbine structural responses which are sensitive to the discretization of the high-resolution domains, improvements can be made. It is straightforward to increase the spatial resolution of the inflow wind, and this would suffice as a solution. However, due to high computational costs, it is often not feasible to generate inflows (with TurbSim) which fulfils both FAST.Farm's domain dimension recommendations and discretization guidelines simultaneously. To circumvent this problem, separate inflows can be generated for the low- and high-resolutions domains. This was done for the calibration procedure, but not for any other FAST.Farm results, due to the number of simulated wind conditions being too numerous. To do it efficiently with respect to time, the somewhat lengthy process of spatio-temporally synchronizing the low- and high-resolutions inflows should be automated with a script, such that the process can be handled by e.g. a computational cluster.

For the artificial neural network, it is likely that there are more optimal architectures to represent the FAST.Farm data. Further effort can be put into optimizing the ANN. Although, a more interesting prospect of the ANN is the possibility to quite easily increase its number of inputs, such that it predicts total wind farm production based on a wider and more complex range of operating conditions. For example, wind direction, wind speed, spatial configurations of the wind turbines, number of wind turbines, transient wind behaviour (e.g. wind gusts), these properties can likely be included as inputs in a modified ANN. Likewise, its number of outputs can be increased, such that its predictions cover more wind farm responses, in addition to $\langle P \rangle_{tot}$. For instance, structural loads may be a desired output, which would enable more advanced active yaw control strategies, with decisions based on a plethora of ANN predictions. Despite its advantageous outlooks, there are limitations to what is achievable with an ANN. For this work, a relatively limited range of operating conditions was studied. To train the ANN, many operating conditions were simulated. As more inputs are added to the ANN, more operating conditions have to be simulated. At some point, it might no longer be feasible to conduct enough FAST.Farm simulations to adequately train the ANN, due to computational cost constraints.

Concerning the active yaw control, to enhance its performance in medium turbulence intensity cases, the input signals to the artificial neural network must be as close to their corresponding temporally averaged values as possible, which is what the ANN is trained with. There are several ways to address this issue. The source code of either FAST.Farm or the OpenFAST module can be modified such that the AYC has direct access to inflow-specified properties such as turbulence intensity, wind shear etc. Another solution would be to utilize a rolling mean within the AYC. It has been observed that such an approach would need to average over quite a long period for the signal to not fluctuate too much. As an alternative to that option, a higher order low pass filter could perhaps suffice to generate stable signals, for instance, a higher order Butterworth or Chebyshev filter could be used. The aim would be to acquire a better roll-off than that of the low pass filter used in this study. A low pass filter is arguably preferable over the rolling mean approach, as it typically requires fewer numerical operations. Finally, it is possible that training the ANN with time series data (rather than with mean data) could eliminate the problem of trying to produce a stable enough signal.

References

- ¹V. Smil, *Energy and civilization*, The MIT Press (MIT Press, London, England, Oct. 2018).
- ²C. Bellard, C. Bertelsmeier, P. Leadley, W. Thuiller, and F. Courchamp, “Impacts of climate change on the future of biodiversity”, *Ecology Letters* **15**, 365–377 (2012).
- ³C. D. Thomas, A. Cameron, R. E. Green, M. Bakkenes, L. J. Beaumont, Y. C. Collingham, B. F. N. Erasmus, M. F. de Siqueira, A. Grainger, L. Hannah, L. Hughes, B. Huntley, A. S. van Jaarsveld, G. F. Midgley, L. Miles, M. A. Ortega-Huerta, A. T. Peterson, O. L. Phillips, and S. E. Williams, “Extinction risk from climate change”, *Nature* **427**, 145–148 (2004).
- ⁴G. C. Unruh, “Understanding carbon lock-in”, *Energy Policy* **28**, 817–830 (2000).
- ⁵Energimyndigheten, *Nationell strategi för en hållbar vindkraftsutbyggnad* (Eskilstuna, Sweden, 2021).
- ⁶F. Ståhle, P. Edström, R. Walsh, E. Edfeldt, G. Nilsson, M. Bergman, S. B. Lauritsen, L. B. Jørgensen, S. Granström, T. Brandt, S. Tiedemann, and I. Kielichowska, *Havsbase rad vindkraft potential och kostnader*, tech. rep. (Sweco, Jan. 2017).
- ⁷Á. Jiménez, A. Crespo, and E. Migoya, “Application of a les technique to characterize the wake deflection of a wind turbine in yaw”, *Wind Energy* **13**, 559–572 (2010).
- ⁸S. Boersma, B. Doekemeijer, P. Gebraad, P. Fleming, J. Annoni, A. Scholbrock, J. Frederik, and J.-W. van Wingerden, “A tutorial on control-oriented modeling and control of wind farms”, in 2017 american control conference (acc) (2017), pp. 1–18.
- ⁹M. J. Churchfield, S. Lee, J. Michalakes, and P. J. Moriarty, “A numerical study of the effects of atmospheric and wake turbulence on wind turbine dynamics”, *Journal of Turbulence* **13**, N14 (2012).
- ¹⁰P. Fleming, P. M. Gebraad, S. Lee, J.-W. van Wingerden, K. Johnson, M. Churchfield, J. Michalakes, P. Spalart, and P. Moriarty, “Simulation comparison of wake mitigation control strategies for a two-turbine case”, *Wind Energy* **18**, 2135–2143 (2015).
- ¹¹P. B. S. Lissaman, *Energy effectiveness of arrays of wind energy collection systems*, tech. rep. (National Swedish Board for Energy Source Development, 1976).
- ¹²P. B. S. Lissaman, “Energy effectiveness of arbitrary arrays of wind turbines”, *Journal of Energy* **3**, 323–328 (1979).
- ¹³T. Faxen, “Wake interaction in an array of windmills - theory and preliminary results”, **1**, 6 (1978).
- ¹⁴J. Ainslie, “Calculating the flowfield in the wake of wind turbines”, *Journal of Wind Engineering and Industrial Aerodynamics* **27**, 213–224 (1988).
- ¹⁵L. Vermeer, J. Sørensen, and A. Crespo, “Wind turbine wake aerodynamics”, *Progress in Aerospace Sciences* **39**, 467–510 (2003).
- ¹⁶G. C. Larsen, H. A. Madsen, K. Thomsen, and T. J. Larsen, “Wake meandering: a pragmatic approach”, *Wind Energy* **11**, 377–395 (2008).
- ¹⁷F. Porté-Agel, M. Bastankhah, and S. Shamsoddin, “Wind-turbine and wind-farm flows: a review”, *Boundary-Layer Meteorology* **174**, 1–59 (2019).
- ¹⁸R. J. Barthelmie, S. T. Frandsen, M. N. Nielsen, S. C. Pryor, P.-E. Rethore, and H. E. Jørgensen, “Modelling and measurements of power losses and turbulence intensity in wind turbine wakes at middelgrunden offshore wind farm”, *Wind Energy* **10**, 517–528 (2007).
- ¹⁹R. J. Barthelmie and L. E. Jensen, “Evaluation of wind farm efficiency and wind turbine wakes at the nysted offshore wind farm”, *Wind Energy* **13**, 573–586 (2010).
- ²⁰P. Vølund, “Loads on a horizontal axis wind turbine operating in wake”, *Journal of Wind Engineering and Industrial Aerodynamics* **39**, 317–328 (1992).
- ²¹D. Medici and P. H. Alfredsson, “Measurements on a wind turbine wake: 3d effects and bluff body vortex shedding”, *Wind Energy* **9**, 219–236 (2006).
- ²²P. M. O. Gebraad, F. W. Teeuwisse, J. W. van Wingerden, P. A. Fleming, S. D. Ruben, J. R. Marden, and L. Y. Pao, “Wind plant power optimization through yaw control using a parametric model for wake effects—a CFD simulation study”, *Wind Energy* **19**, 95–114 (2014).
- ²³K. Johnson and N. Thomas, “Wind farm control: addressing the aerodynamic interaction among wind turbines”, in , cited By 131 (2009), pp. 2104–2109.
- ²⁴P. A. Fleming, P. M. Gebraad, S. Lee, J.-W. van Wingerden, K. Johnson, M. Churchfield, J. Michalakes, P. Spalart, and P. Moriarty, “Evaluating techniques for redirecting turbine wakes using sowfa”, *Renewable Energy* **70**, Special issue on aerodynamics of offshore wind energy systems and wakes, 211–218 (2014).

- ²⁵H. Abedi, L. Davidson, and S. Voutsinas, “Development of free vortex wake method for yaw misalignment effect on the thrust vector and generated power”, in *32nd aiaa applied aerodynamics conference* ().
- ²⁶M. Bastankhah and F. Porté-Agel, “Experimental and theoretical study of wind turbine wakes in yawed conditions”, *Journal of Fluid Mechanics* **806**, 506–541 (2016).
- ²⁷J. Bartl, F. Mühle, J. Schottler, L. Sætran, J. Peinke, M. Adaramola, and M. Hölling, “Wind tunnel experiments on wind turbine wakes in yaw: effects of inflow turbulence and shear”, *Wind Energy Science* **3**, 329–343 (2018).
- ²⁸E. Kleusberg, P. Schlatter, and D. S. Henningson, “Parametric dependencies of the yawed wind-turbine wake development”, *Wind Energy* **23**, 1367–1380 (2020).
- ²⁹L. A. Martinez-Tossas, J. Annoni, P. A. Fleming, and M. J. Churchfield, “The aerodynamics of the curled wake: a simplified model in view of flow control”, *Wind Energy Science* **4**, 127–138 (2019).
- ³⁰L. Vollmer, G. Steinfeld, D. Heinemann, and M. Kühn, “Estimating the wake deflection downstream of a wind turbine in different atmospheric stabilities: an les study”, *Wind Energy Science* **1**, 129–141 (2016).
- ³¹P. Fleming, J. Annoni, J. J. Shah, L. Wang, S. Ananthan, Z. Zhang, K. Hutchings, P. Wang, W. Chen, and L. Chen, “Field test of wake steering at an offshore wind farm”, *Wind Energy Science* **2**, 229–239 (2017).
- ³²P. Fleming, J. King, K. Dykes, E. Simley, J. Roadman, A. Scholbrock, P. Murphy, J. K. Lundquist, P. Moriarty, K. Fleming, J. van Dam, C. Bay, R. Mudafort, H. Lopez, J. Skopek, M. Scott, B. Ryan, C. Guernsey, and D. Brake, “Initial results from a field campaign of wake steering applied at a commercial wind farm – part 1”, *Wind Energy Science* **4**, 273–285 (2019).
- ³³B. Dou, T. Qu, L. Lei, and P. Zeng, “Optimization of wind turbine yaw angles in a wind farm using a three-dimensional yawed wake model”, *Energy* **209**, 118415 (2020).
- ³⁴B. P. Rak and R. Santos Pereira, “Impact of the wake deficit model on wind farm yield: a study of yaw-based control optimization”, *Journal of Wind Engineering and Industrial Aerodynamics* **220**, 104827 (2022).
- ³⁵W. Miao, C. Li, G. Pavesi, J. Yang, and X. Xie, “Investigation of wake characteristics of a yawed hawt and its impacts on the inline downstream wind turbine using unsteady cfd”, *Journal of Wind Engineering and Industrial Aerodynamics* **168**, 60–71 (2017).
- ³⁶C. L. Archer and A. Vassel-Be-Hagh, “Wake steering via yaw control in multi-turbine wind farms: recommendations based on large-eddy simulation”, *Sustainable Energy Technologies and Assessments* **33**, 34–43 (2019).
- ³⁷J. Schottler, A. Hölling, J. Peinke, and M. Hölling, “Brief communication: on the influence of vertical wind shear on the combined power output of two model wind turbines in yaw”, *Wind Energy Science* **2**, 439–442 (2017).
- ³⁸P. Stanfel, K. Johnson, C. J. Bay, and J. King, “A distributed reinforcement learning yaw control approach for wind farm energy capture maximization*”, in *2020 american control conference (acc)* (2020), pp. 4065–4070.
- ³⁹P. M. O. Gebraad and J. W. van Wingerden, “Maximum power-point tracking control for wind farms”, *Wind Energy* **18**, 429–447 (2014).
- ⁴⁰U. Ciri, M. A. Rotea, and S. Leonardi, “Effect of the turbine scale on yaw control”, *Wind Energy* **21**, 1395–1405 (2018).
- ⁴¹P. M. O. Gebraad, F. W. Teeuwisse, J. W. van Wingerden, P. A. Fleming, S. D. Ruben, J. R. Marden, and L. Y. Pao, “Wind plant power optimization through yaw control using a parametric model for wake effects—a cfd simulation study”, *Wind Energy* **19**, 95–114 (2016).
- ⁴²J. Jonkman and S. Kelsey, *Fast.farm user’s guide and theory manual*, NREL/TP-5000-78785 (National Renewable Energy Laboratory, Golden, CO, 2021).
- ⁴³J. Jonkman, S. Kelsey, P. Doubrawa, and N. Hamilton, *Fast.farm response to varying wind inflow techniques*, NREL/CP-5000-72893 (National Renewable Energy Laboratory, Golden, CO, 2019).
- ⁴⁴K. Shaler and J. Jonkman, “Fast.farm development and validation of structural load prediction against large eddy simulations”, *Wind Energy* **24**, 428–449 (2021).
- ⁴⁵K. Shaler, J. Jonkman, and N. Hamilton, “Effects of inflow spatiotemporal discretization on wake meandering and turbine structural response using FAST.farm”, *Journal of Physics: Conference Series* **1256**, 012023 (2019).
- ⁴⁶P. Doubrawa Moreira, J. Annoni, J. Jonkman, and A. Ghate, “Optimization-based calibration of fast.farm parameters against sowfa”, *10.2514/6.2018-0512* (2018).
- ⁴⁷B. Jonkman, *Turbsim user’s guide: version 1.50*, NREL/TP-500-46198 (National Renewable Energy Laboratory, Golden, CO, 2009).
- ⁴⁸J. Jonkman, S. Butterfield, W. Musial, and G. Scott, *Definition of a 5-mw reference wind turbine for offshore system development*, NREL/TP-500-38060 (National Renewable Energy Laboratory, Golden, CO, 2009).

- ⁴⁹J. Wallace, *Atmospheric science : an introductory survey* (Elsevier Academic Press, Amsterdam Boston, 2006).
- ⁵⁰R. Stull, *Practical meteorology : an algebra-based survey of atmospheric science* (Dept. of Earth, Ocean & Atmospheric Sciences, University of British Columbia, Vancouver, BC, Canada, 2017).
- ⁵¹X. Zhang, *Cfd simulation of neutral abl flows* (Risø DTU - National Laboratory for Sustainable Energy available from Risø National Laboratory, Information Service Department, City, 2009).
- ⁵²S. Emeis, *Wind energy meteorology : atmospheric physics for wind power generation* (Springer, Cham, Switzerland, 2018).
- ⁵³J. F. Manwell, J. G. McGowan, and A. L. Rogers, *Wind energy explained*, en, 2nd ed. (John Wiley & Sons, Nashville, TN, Sept. 2010).
- ⁵⁴P. Kundu, *Fluid mechanics* (Academic Press, Amsterdam, 2015).
- ⁵⁵L. Davidson, *Fluid mechanics, turbulent flow and turbulence modeling* (Chalmers University of Technology, Göteborg, 2022).
- ⁵⁶C. M. Institute, *Millennium problems*, (2022) <https://www.claymath.org/millennium-problems> (visited on 07/02/2022).
- ⁵⁷J. C. Kaimal, J. C. Wyngaard, Y. Izumi, and O. R. Coté, “Spectral characteristics of surface-layer turbulence”, *Quarterly Journal of the Royal Meteorological Society* **98**, 563–589 (1972).
- ⁵⁸S. L. Dixon, *Fluid mechanics and thermodynamics of turbomachinery* (Butterworth-Heinemann, Oxford, 2014), pp. 442–443.
- ⁵⁹F. Bianchi, *Wind turbine control systems : principles, modelling and gain scheduling design* (Springer, London, 2007).
- ⁶⁰E. Kleusberg, “Wind-turbine wakes-effects of yaw, shear and turbine interaction”, PhD thesis (KTH Royal Institute of Technology, 2019).
- ⁶¹H. Abedi, S. Sarkar, and H. Johansson, “Numerical modelling of neutral atmospheric boundary layer flow through heterogeneous forest canopies in complex terrain (a case study of a swedish wind farm)”, *Renewable Energy* **180**, 806–828 (2021).
- ⁶²B. Nebenführ and L. Davidson, “Prediction of wind-turbine fatigue loads in forest regions based on turbulent inflow fields”, *Wind Energy* **20**, 1003–1015 (2017).
- ⁶³M. Wahde, *Biologically inspired optimization methods*, en (WIT Press, Southampton, England, Aug. 2008).
- ⁶⁴J. Hertz, A. Krogh, and R. G. Palmer, *Introduction to the theory of neural computation* (CRC Press, Mar. 2018).
- ⁶⁵K. Hornik, M. Stinchcombe, and H. White, “Multilayer feedforward networks are universal approximators”, *Neural Networks* **2**, 359–366 (1989).
- ⁶⁶M. T. Hagan, H. B. Demuth, and M. H. Beale, *Neural network design (2nd edition)*, 2nd ed. (Martin Hagan, Sept. 2014).
- ⁶⁷G. H. Golub and C. F. Van Loan, *Matrix computations*, en, 3rd ed., Johns Hopkins Series in the Mathematical Sciences (Johns Hopkins University Press, Baltimore, MD, Oct. 1996).
- ⁶⁸E. Quon, *Simulated and measured wake identification and characterization*, version 2.0.4, Sept. 2019.
- ⁶⁹P. Doubrawa, L. A. Martinez-Tossas, E. Quon, P. Moriarty, and M. J. Churchfield, “Comparison of mean and dynamic wake characteristics between research-scale and full-scale wind turbines”, *Journal of Physics: Conference Series* **1037**, 072053 (2018).
- ⁷⁰M. Bastankhah and F. Porté-Agel, “A new analytical model for wind-turbine wakes”, *Renewable Energy* **70**, Special issue on aerodynamics of offshore wind energy systems and wakes, 116–123 (2014).
- ⁷¹D. P. Kingma and J. Ba, *Adam: a method for stochastic optimization*, 2014.
- ⁷²Meta AI, *Pytorch*, version 1.12.0, May 29, 2022.
- ⁷³T. Hastie, R. Tibshirani, and J. Friedman, *The elements of statistical learning* (Springer New York, 2009).
- ⁷⁴L. Yang and A. Shami, “On hyperparameter optimization of machine learning algorithms: theory and practice”, *Neurocomputing* **415**, 295–316 (2020).
- ⁷⁵S. W. Smith, *The scientist and engineer’s guide to digital signal processing* (California Technical Pub, Dec. 1997).
- ⁷⁶D. Medici, “Experimental studies of wind turbine wakes : power optimisation and meandering”, QC 20101018, PhD thesis (KTH, Mechanics, 2005), pp. ix, 46.
- ⁷⁷G. Ceballos, P. R. Ehrlich, A. D. Barnosky, A. Garcia, R. M. Pringle, and T. M. Palmer, “Accelerated modern human-induced species losses: entering the sixth mass extinction”, *Science Advances* **1**, 10.1126/sciadv.1400253 (2015).

- ⁷⁸R. Warren, O. Andrews, S. Brown, N. Forstenhaeusler, D. Gernaat, P. Goodwin, I. Harris, H. He, C. Hope, F. Gonzalez-Colon, R. Nicholls, T. Osborn, J. Price, D. Van Vuuren, and R. Wright, “Risks associated with global warming of 1.5°C or 2°C”, in Briefing note ().
- ⁷⁹D. Y. Leung and Y. Yang, “Wind energy development and its environmental impact: a review”, *Renewable and Sustainable Energy Reviews* **16**, 1031–1039 (2012).
- ⁸⁰E. B. Arnett and R. F. May, “Mitigating wind energy impacts on wildlife: approaches for multiple taxa”, [10.26077/1JEG-7R13](https://doi.org/10.26077/1JEG-7R13) (2016).
- ⁸¹B. K. Sovacool, “The avian and wildlife costs of fossil fuels and nuclear power”, *Journal of Integrative Environmental Sciences* **9**, 255–278 (2012).
- ⁸²S. L. Piano, “Ethical principles in machine learning and artificial intelligence: cases from the field and possible ways forward”, *Humanities and Social Sciences Communications* **7**, [10.1057/s41599-020-0501-9](https://doi.org/10.1057/s41599-020-0501-9) (2020).

A Figures and Tables

In this section, figures and tables relevant to the work are presented.

A.1 Method

Items referred to in the methodology section are presented in the following text.

A.1.1 Wake Tracking

To determine the radial dependence of the radial and axial wake velocity deficits (δV_r and δV_x , respectively), the waked field is sampled in a number of points, as shown in Fig. A.1. For the sampling points outside the wake contour, the wake quantities are set to zero.

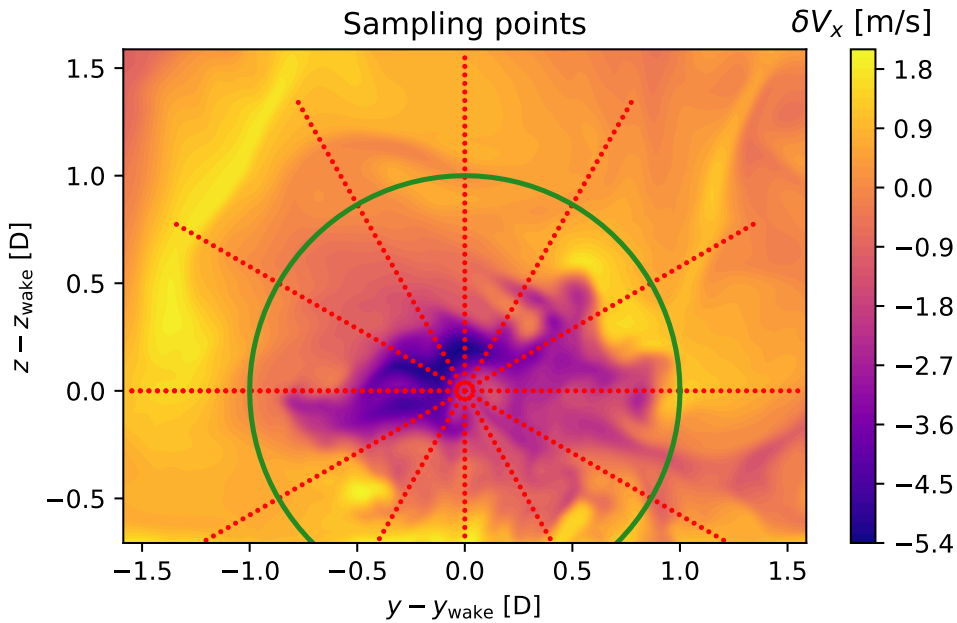


Figure A.1: The sampling points (●) and the Gaussian wake track contour (—) superimposed on the axial velocity deficit field

A.1.2 Low-Pass Filter

Figure A.2 shows the horizontal wind speed (v_{hor}) at hub height (90 m). Both the instantaneous and the low-pass filtered signal are shown together. It is suggested that the filter yields a smooth signal which is close to the reference wind speed of 8 m s^{-1} , which is desired. However, the settling time for the filter is quite long. After 1000 s, the filtered signal is quite close to the reference wind speed. This means that a FAST.Farm simulation ought to be run for roughly 1000 s before the active yaw control is activated, otherwise the wind conditions fed to the neural network will be erroneously estimated.

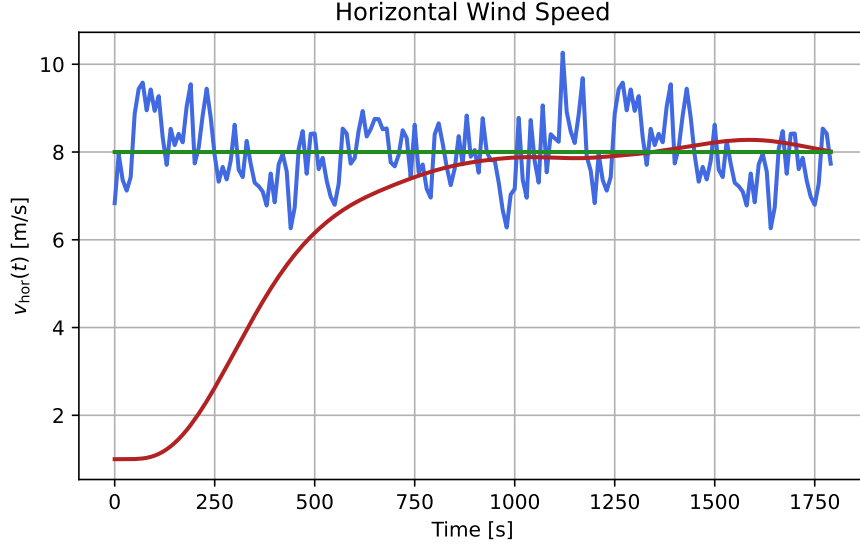


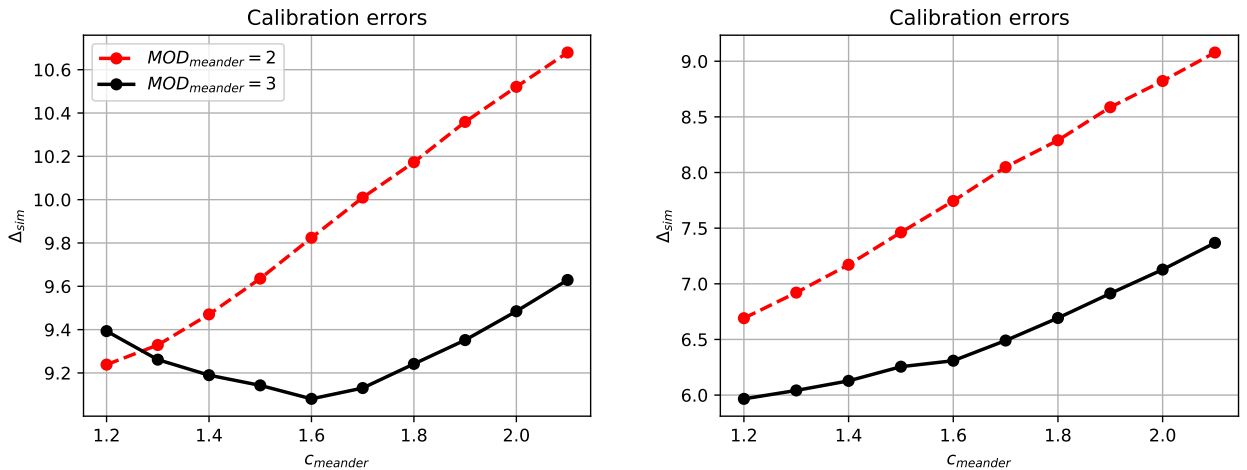
Figure A.2: The horizontal wind speed at hub height. (—): Reference wind speed of 8 ms^{-1} ; (—): Instantaneous wind speed (sample rate 0.1 Hz); (—): Low-pass filtered wind speed.

A.2 Results

Items referred to in the results section are presented here.

A.2.1 Calibration

Figure A.3a displays the calibration error (Δ_{sim}) calculated with data from the five most downwind extraction planes. It is shown that the error is more than halved, as compared to the (Δ_{sim}) in Fig. 4.2. Moreover, the optimal value of c_{meander} increases from 1.2 to 1.6. Further, Fig. A.3b displays the calibration error when the contribution from the radial velocity deficits is neglected. It is clear that neglecting $\Delta\langle\delta V_r\rangle$ yields a much smaller error, however, the optimal c_{meander} does not.



(a) The calibration error with data from only the five extraction planes between WT1 and WT2

(b) The calibration error without accounting for the error in radial velocity deficit ($\Delta\langle\delta V_r\rangle$)

Figure A.3: The calibration error (Δ_{sim}) calculated in two modified ways, namely by excluding data from five out of ten data extraction planes and by excluding one of the four wake quantities ($\Delta\langle\delta V_r\rangle$)

A.2.2 Turbulent Length and Time Scales

To assess the minimum time for the periodic TurbSim-generated inflows, the autocorrelation (B_{uu}^t) can be calculated. It is a function of time and is defined mathematically as [55]:

$$B_{uu}^t(\tau) = \frac{1}{(u'_{\text{rms}})^2} \int_0^\infty u(t)'u'(t-\tau)dt, \quad (\text{A.1})$$

where u'_{rms} is the root-mean-square of the fluctuating part of the streamwise velocity component. Figure A.4 demonstrates the autocorrelation at hub height (90 m), using the LES data. At roughly $t = 50$ s, the auto correlation goes to zero, suggesting that the minimum time of periodic inflows must at least be 50 s in order to accurately capture any repeating patterns in the wind. The period of the TurbSim-generated inflows is 1200 s, which is considerably longer than 50 s. The area under the curve of B_{uu}^t (in Fig. A.4) corresponds to

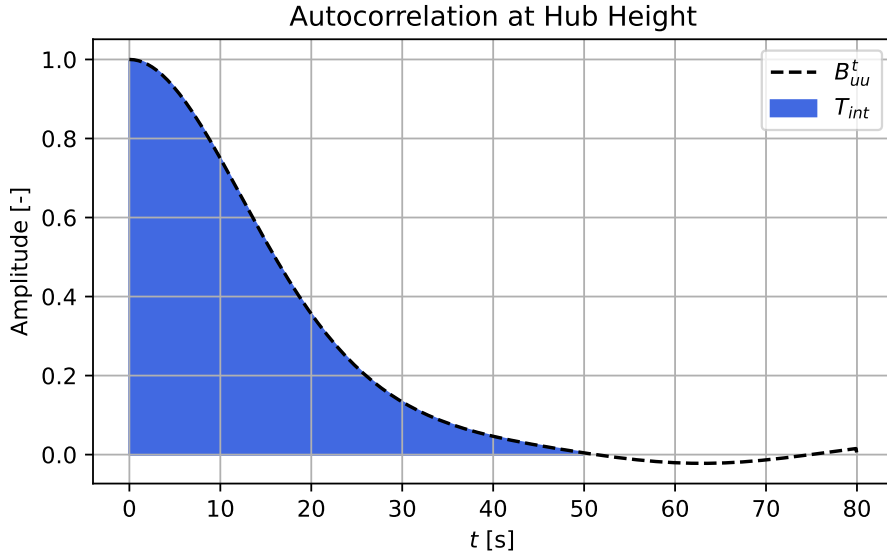


Figure A.4: The autocorrelation (B_{uu}^t) and the integral time scale (T_{int}) which is the area under the curve

the integral time scale (T_{int}) which in turn can be used to estimate the integral length scale (L_{int}), assuming Taylor’s frozen turbulence hypothesis is valid [55]. These scales are shown in Tab. A.1. The turbulent length scale is comparable to the rotor diameter of 126 m.

Table A.1: The integral time scale and length scale at hub height.

Quantity	Symbol	Value
Integral time scale	T_{int}	17.9 s
Integral length scale	L_{int}	143.2 m

A.2.3 Hyperparameter Grid Search

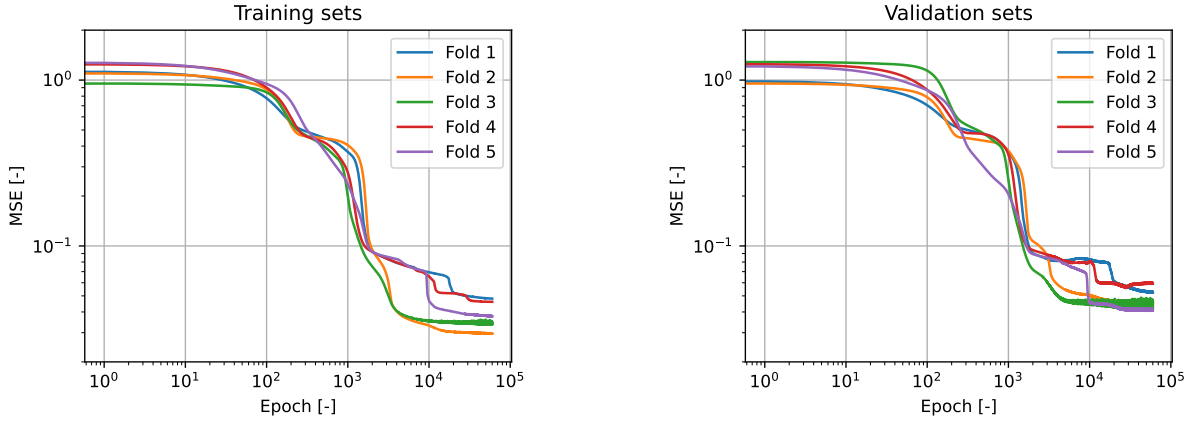
In this section, the results for the grid search for optimal artificial neural network (ANN) hyperparameters are shown. Table A.2 show the mean, minimum, and maximal mean-square validation errors for the K-Fold cross validation procedure for each of the 27 different combinations of hyperparameters. It is shown that the optimal architecture is a model with 3 hidden layers, each consisting of 3 neurons, and the optimal number of epochs is 40000. It should be noted that the optimal hyperparameters likely would be different for a more extensive grid search.

Table A.2: Mean, minimum, and maximal mean-square errors (Δ) for a number of different combinations of hyperparameters. Number of neurons per hidden layer, hidden layers, and epochs are denoted by n_{neurons} , n_{layers} , and n_{epochs} , respectively. The architecture corresponding to the lowest mean error is shown in bold.

n_{neurons}	n_{layers}	n_{epochs}	Δ_{mean}	Δ_{min}	Δ_{max}
3	1	20000	0.050	0.038	0.066
3	2	20000	0.054	0.040	0.061
3	3	20000	0.054	0.037	0.090
4	1	20000	0.052	0.041	0.076
4	2	20000	0.065	0.039	0.080
4	3	20000	0.053	0.031	0.080
5	1	20000	0.041	0.036	0.048
5	2	20000	0.048	0.035	0.062
5	3	20000	0.051	0.040	0.063
3	1	40000	0.046	0.033	0.068
3	2	40000	0.049	0.035	0.088
3	3	40000	0.039	0.028	0.053
4	1	40000	0.053	0.040	0.062
4	2	40000	0.044	0.034	0.057
4	3	40000	0.040	0.035	0.049
5	1	40000	0.044	0.031	0.068
5	2	40000	0.041	0.028	0.058
5	3	40000	0.053	0.033	0.067
3	1	80000	0.040	0.026	0.056
3	2	80000	0.041	0.031	0.063
3	3	80000	0.042	0.035	0.055
4	1	80000	0.043	0.033	0.067
4	2	80000	0.049	0.040	0.065
4	3	80000	0.042	0.030	0.053
5	1	80000	0.046	0.029	0.064
5	2	80000	0.045	0.030	0.070
5	3	80000	0.044	0.034	0.052

A.2.4 Training and Validation Process

The results for the wind farm power production, discussed in Section 4.3.2, were used as training data for the artificial neural network (ANN). With the optimal model described in Section A.2.3, a new K-Fold cross validation procedure was conducted. As shown in Fig. A.5b, the validation Mean-Square Error (MSE) becomes quite low for the five folds, and the mean value of the minimum validation errors is 0.047, averaged over the five folds. The ANN model which is ultimately chosen is the one with the lowest validation error, corresponding to an MSE of 0.041.



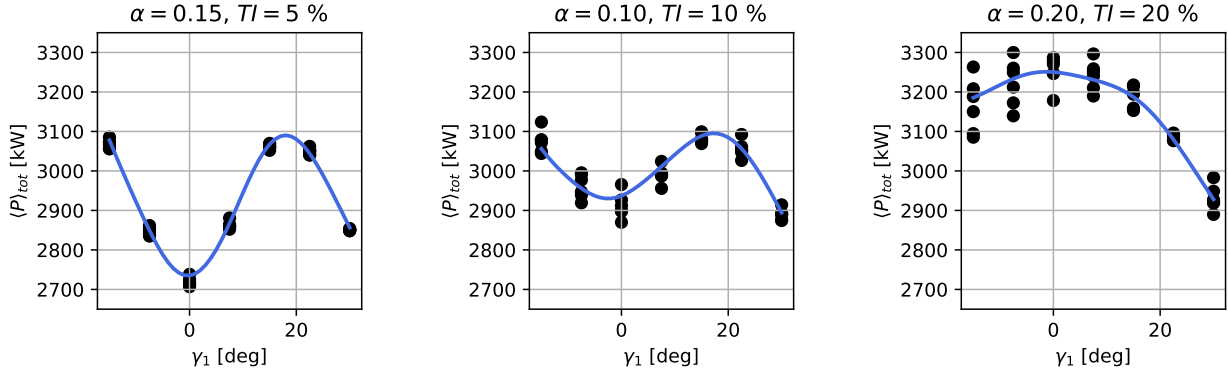
(a) The MSE for the training data

(b) The MSE for the validation data

Figure A.5: The mean squared error (MSE) as a function of epochs for the training and validation data in five holdout validation procedures

A.2.5 Neural Network Power Predictions

To visually assess the capability of the ANN, Fig. A.6 shows FAST.Farm data together with predictions of the ANN. The data is the mean wind farm power production as a function of γ_1 for three different wind conditions. It is clear that the ANN predictions match the trends in the data well, which indicate that the training of the artificial neural network is adequate.



(a) Power production for wind shear exponent $\alpha = 0.15$ and turbulence intensity $TI = 5\%$

(b) Power production for wind shear exponent $\alpha = 0.10$ and turbulence intensity $TI = 10\%$

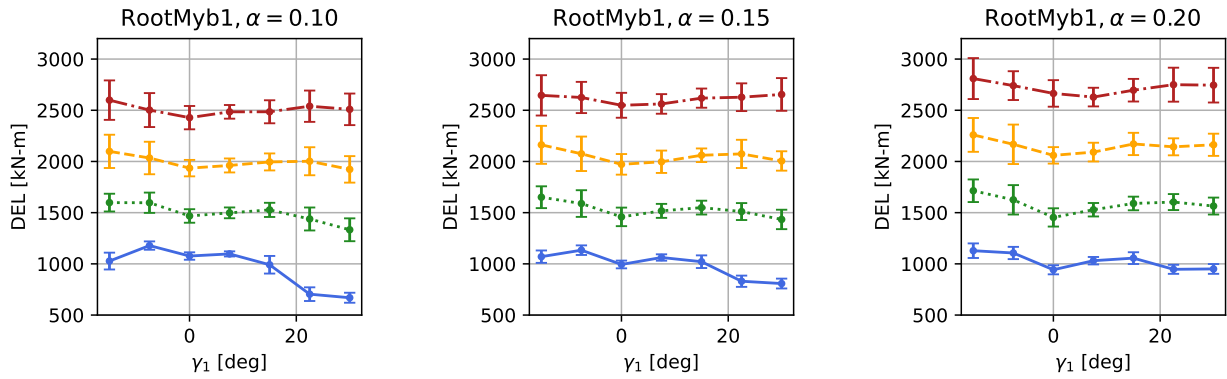
(c) Power production for wind shear exponent $\alpha = 0.20$ and turbulence intensity $TI = 20\%$

Figure A.6: Three subsets of data, first shown in Fig. 4.11, along with the prediction of the artificial neural network, showing the temporally averaged wind farm power production in three wind conditions for a range of yaw misalignments (γ_1). (●): FAST.Farm data; (—): ANN prediction.

A.2.6 Structural Loads

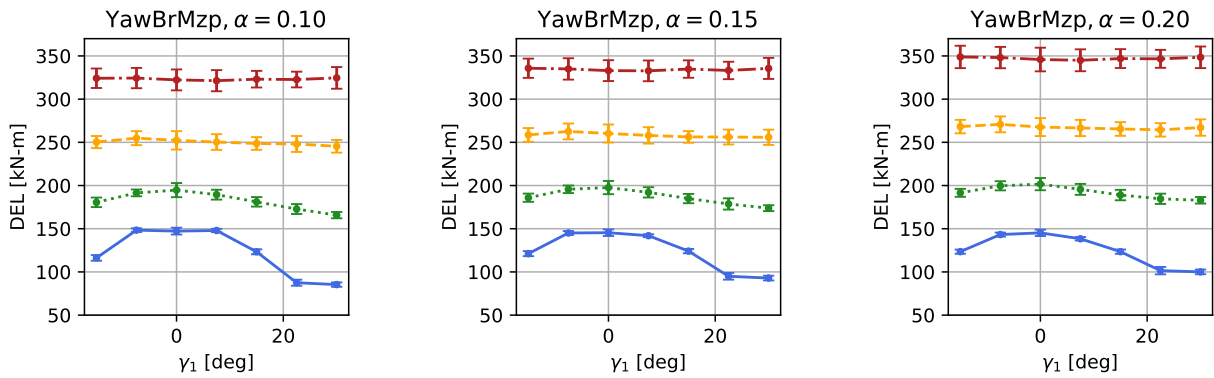
Figures A.7, A.8, and A.9 show the bending moment Damage Equivalent Loads (DELs) for the downwind turbine (WT2) with respect to the blade out-of-plane, yaw bearing, and tower base fore-aft, respectively. It can be observed that the loads, as a general rule, decrease as the upwind turbine (WT1) is yawed, such that $\gamma_1 \neq 0^\circ$. This is especially true for low turbulence intensities. For higher TI , there is less benefit to yawing WT1, as the loads for WT2 largely remain unchanged in those cases. The reason why is likely because the high

ambient turbulence render wake steering unfeasible (due to intensified wake meandering), and that the rate of wake recovery is larger.



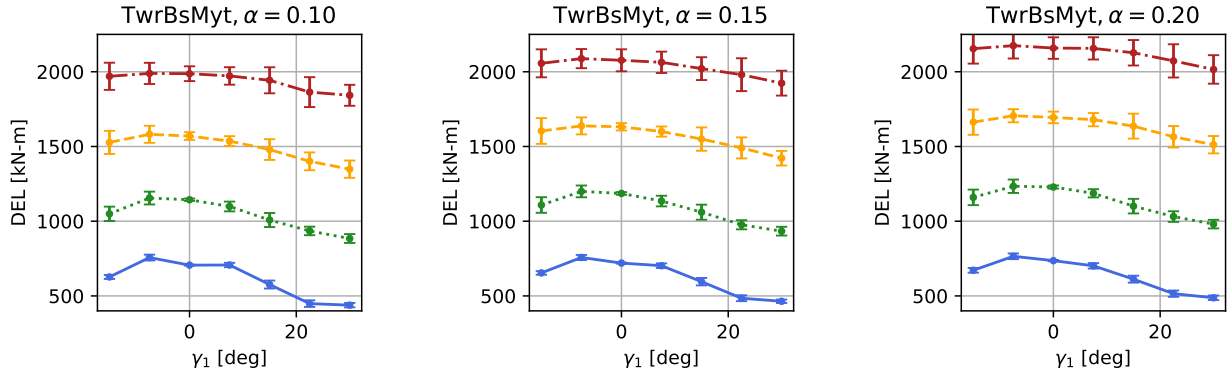
(a) Blade OOP bending moment at wind shear $\alpha = 0.1$ (b) Blade OOP bending moment at wind shear $\alpha = 0.15$ (c) Blade OOP bending moment at wind shear $\alpha = 0.2$

Figure A.7: The blade out-of-plane (OOP) bending moment DEL for WT2 as functions of the upwind turbine's yaw (γ_1) for different wind shear exponents (α) and turbulence intensities (TI). (—): TI = 5%; (····): TI = 10%; (---): TI = 15%; (-.-.-): TI = 20%;



(a) Yaw bearing moment at wind shear $\alpha = 0.1$ (b) Yaw bearing moment at wind shear $\alpha = 0.15$ (c) Yaw bearing moment at wind shear $\alpha = 0.2$

Figure A.8: The yaw bearing moment DEL for WT2 as a function of the upwind turbine's yaw (γ_1) for different wind shear exponents (α) and turbulence intensities (TI). (—): TI = 5%; (····): TI = 10%; (---): TI = 15%; (-.-.-): TI = 20%;



(a) Tower base fore-aft moment at wind shear $\alpha = 0.1$ (b) Tower base fore-aft moment at wind shear $\alpha = 0.15$ (c) Tower base fore-aft moment at wind shear $\alpha = 0.2$

Figure A.9: The tower base fore-aft moment DEL for WT2 as a function of the upwind turbine's yaw (γ_1) for different wind shear exponents (α) and turbulence intensities (TI). (—): $TI = 5\%$; (····): $TI = 10\%$; (---): $TI = 15\%$; (-·-·): $TI = 20\%$;

A.2.7 Wind Shear Exponent and Bulk Velocity

The bulk velocity (u_{bulk}) is a spatially averaged velocity which can be used to easily calculate the mass flow rate through e.g. the rotor. Its mathematical definition is

$$u_{\text{bulk}} = \frac{1}{|b-a|} \int_a^b u(z) dz, \quad (\text{A.2})$$

where, in this case, $a = 27\text{ m}$ and $b = 153\text{ m}$ are the vertical bounds of the rotor area. u is the streamwise velocity component. Using the power law in Eq. (2.3) to predict the wind profile, the bulk velocity can be found as a function of the wind shear exponent (α), which is displayed by Fig. A.10. It is clear that u_{bulk} decreases slightly when α increases, which suggests that there is less power for the wind turbine to extract for high wind shear. However, this difference is quite small. There is only a 2% difference in bulk velocity for a uniform flow ($\alpha = 0$) and a heavily sheared flow ($\alpha = 0.4$).

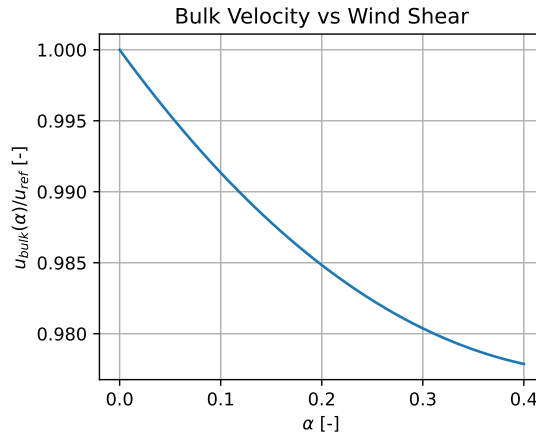


Figure A.10: The bulk velocity (u_{bulk}) as a function of the wind shear exponent (α). The graph is normalized with the reference wind speed at hub height ($u_{\text{ref}} = 8\text{ m s}^{-1}$).

B Mathematical Derivations

In this section, various mathematical derivations relevant to the work are introduced.

B.1 Atmospheric Stability

The stability of the atmosphere can be expressed mathematically. Assuming a fluid element is taken adiabatically to a standard pressure (p_0), its attained temperature (θ) is called the potential temperature. For a perfect gas, the actual temperature (T) can be related to θ according to [54]:

$$T = \theta \left(\frac{p}{p_0} \right)^{(\gamma-1)/\gamma}, \quad (\text{B.1})$$

where p and γ denotes the pressure and the adiabatic index, respectively. Differentiating with respect to height (z) and taking the logarithm of Eq. (B.1) yields

$$\frac{1}{T} \frac{dT}{dz} = \frac{1}{\theta} \frac{d\theta}{dz} + \frac{\gamma-1}{\gamma} \frac{1}{p} \frac{dp}{dz}. \quad (\text{B.2})$$

The hydrostatic rule, describing the drop in pressure with height, is defined as

$$\frac{dp}{dz} = -\rho g, \quad (\text{B.3})$$

where g and ρ is the gravity of Earth and fluid density, respectively. The perfect gas law is defined as

$$p = \rho R T, \quad (\text{B.4})$$

where R is the specific gas constant, which can be related to the specific heat capacity at constant pressure (c_p) and constant volume (c_v) according to $R = c_p - c_v$. Moreover, the adiabatic constant is defined as $\gamma = c_p/c_v$. Plugging Eqs. (B.3) (B.4) into Eq. (B.2), and multiplying with T gives:

$$\frac{T}{\theta} \frac{d\theta}{dz} = \frac{dT}{dz} + \frac{\gamma-1}{\gamma} \frac{1}{\rho(c_p - c_v)} \cdot \rho g = \frac{dT}{dz} + \frac{g}{c_p} = \Gamma - \Gamma_a, \quad (\text{B.5})$$

where $\Gamma \equiv dT/dz$ and $\Gamma_a = -g/c_p$ denotes the lapse rate and adiabatic lapse rate, respectively. The lapse rate is the vertical temperature gradient, and the adiabatic lapse rate is the largest rate that the temperature can decrease with height without causing instability [54]. Typically, $\Gamma_a = -g/c_p \approx -10^\circ\text{C km}^{-1}$ for air at normal atmospheric pressure and temperature conditions. From Eq. (B.5) it is understood that if $\Gamma = \Gamma_a$, the potential temperature gradient is zero, hence θ and the entropy must be uniform with height. Using the lapse rate, the atmospheric stability can be related to the potential temperature gradient according to

$$\begin{cases} \frac{d\theta}{dz} > 0 & (\text{stable}), \\ \frac{d\theta}{dz} = 0 & (\text{neutral}), \\ \frac{d\theta}{dz} < 0 & (\text{unstable}). \end{cases} \quad (\text{B.6})$$

The potential density (ρ_θ) is the density attained by a fluid particle taken to p_0 isentropically. This quantity may give a more intuitive sense of the atmospheric stability than the potential temperature. The density can be related to the potential density according to

$$\rho = \rho_\theta \left(\frac{p}{p_0} \right)^{1/\gamma}. \quad (\text{B.7})$$

Taking the logarithm of and differentiating (with respect to z) Eq. (B.7) yields

$$\frac{1}{\rho} \frac{d\rho}{dz} = \frac{1}{\rho_\theta} \frac{d\rho_\theta}{dz} + \frac{1}{\gamma} \left(\frac{1}{p} \frac{dp}{dz} \right). \quad (\text{B.8})$$

Equations (B.3), (B.4), (B.5), and (B.8) together yields a relation between the potential temperature and potential density according to

$$-\frac{1}{\rho_\theta} \frac{d\rho_\theta}{dz} = \frac{\Gamma - \Gamma_a}{T} = \frac{1}{\theta} \frac{d\theta}{dz}. \quad (\text{B.9})$$

Hence, by the same logic as for the potential temperature, it is understood that the atmospheric boundary layer is stable, unstable, or neutrally stable if $d\rho_\theta/dz$ is negative, positive or zero, respectively.

B.2 Betz' Limit

Betz limit is a a useful result which can be derived from the Actuator Disc Model (ADM), which is covered in Section 2.3.1. Betz limit sets a theoretical upper bound on what ratio of the available energy in the wind can be extracted. It will be derived here.

The axial force (F_n) exerted on the disc can be related to the drop in momentum across the disc such that

$$F_n = \dot{m}(u_\infty - u_{-\infty}) = \rho A_D u_D (u_\infty - u_{-\infty}), \quad (\text{B.10})$$

where \dot{m} , and A_D denotes the mass flow rate, and the cross-sectional area of the stream tube at the rotor, respectively. The streamwise velocity far upstream, far downstream, and at the rotor are denoted by u_∞ , $u_{-\infty}$, and u_D , respectively. The axial force can also be expressed in the pressure drop across the disc, as illustrated in Fig. 2.4b, hence

$$F_n = A_D (p_D^+ - p_D^-), \quad (\text{B.11})$$

where p_D^+ and p_D^- denotes the pressure just up- and down-stream of the rotor, respectively.

Bernoulli's equation describes the balance of static and dynamic pressure along a streamline. By neglecting effects of gravity or treating the flow as horizontal, Bernoulli's equation can be expressed as

$$p_0 + \frac{1}{2} \rho u_\infty^2 = p_D^+ + \frac{1}{2} \rho u_D^2 \quad (\text{B.12})$$

$$p_0 + \frac{1}{2} \rho u_{-\infty}^2 = p_D^- + \frac{1}{2} \rho u_D^2, \quad (\text{B.13})$$

where ρ and p_0 denotes density of air and the ambient pressure, which is retained far upstream and far downstream (as indicated by the pressure curve in Fig. 2.4b), where the presence of the disc is not felt by the flow. Subtracting Eq. (B.13) from Eq. (B.12) yields an expression for $p_D^+ - p_D^-$. Plugging that expression into Eq. (B.11) and equating it to Eq. (B.10) yields

$$\rho A_D u_D (u_\infty - u_{-\infty}) = A_D \left(\frac{1}{2} \rho u_\infty^2 - \frac{1}{2} \rho u_{-\infty}^2 \right). \quad (\text{B.14})$$

Dividing Eq. (B.14) by $\rho A_D (u_\infty - u_{-\infty})$ and rearranging gives

$$u_{-\infty} = 2u_D - u_\infty. \quad (\text{B.15})$$

Furthermore, a useful quantity is the axial flow induction factor (\bar{a}) defined implicitly as

$$u_D = u_\infty (1 - \bar{a}). \quad (\text{B.16})$$

The power (P) extracted by the turbine can be expressed as a function of \bar{a} according to [58]:

$$P = F_n u_D = \dot{m}(u_\infty - u_{-\infty}) u_D = \rho A_D u_D^2 (2u_\infty - 2u_D) = \rho A_D u_\infty^3 2\bar{a}(1 - \bar{a})^2, \quad (\text{B.17})$$

where Eqs. (B.15) and (B.16) were used in the derivation of P . A few familiar results are given by the expression of P . The extracted power increases cubically with the free stream velocity (u_∞) and the swept area increases power capture.

The kinetic power that is available in an undisturbed flow (P_0) passing the through the area A_D is given by

$$P_0 = \frac{1}{2} \rho A_D u_\infty^3. \quad (\text{B.18})$$

To finally derive Betz limit, a power coefficient is defined as

$$C_P = P/P_0 = 4\bar{a}(1 - \bar{a})^2, \quad (\text{B.19})$$

which take a maximum value of $C_{P,max} = 16/27 \approx 59\%$ when $\bar{a} = 1/3$ [58]. Thus, the ADM has been used to derive Betz limit, which suggests that a wind turbine can not extract more than 59% of the kinetic power in the wind.

C Ethical considerations

There are benefits to improving the performance of wind farms (which is the aim of this work) as this could hasten the transition away from the fossil fuels dependency of the contemporary society. The emissions of fossil fuels drive climate change which have great consequences, such as the accelerated rate of species extinction, a rate which is already at historically high levels [2, 3, 77]. Further, the estimated future cost of climate change is staggering, even for a 1.5 °C warmer world (in accordance with the Paris Agreement) [78]. Hence, ecological and economical damage can be mitigated if technological advancements are made within the renewable energy sector.

However, wind power is not only beneficial. Wind turbines can cause noise which affects the well-being of nearby residents negatively [79]. Moreover, the wind turbines can be perceived as a visual intrusion, which is a reoccurring reason Swedish municipalities have objected to proposed wind farms. Further, its negative effects on animal wildlife include: loss of habitat; deaths of birds and bats due to collision with the wind turbine blades; noise, which has been observed to change the behaviour of marine wildlife. There are ways to mitigate these harms. Regarding its impact on avian life, its harmful impact can be reduced by planning and various technical solutions which relies on stopping the wind turbines if birds are nearby [80]. However, its impact should be put in context. Compared to nuclear and coal, wind power is responsible for a considerably lower amount of avian deaths per unit energy produced [81]. Lastly, any improvement in power production (which is the aim of this work), which could lower the total number of deployed wind turbines, could therefore decrease the mentioned negative impacts of wind power.

The ethical aspects of realizing this project are less distinct than those of deploying physical wind turbines. The numerical approach of this work means that there are few apparent direct consequences, but one risk is associated with the use of the computational cluster which will be utilized during this project. The cluster is a limited resource. The simulations for this project need to be planned carefully as to not deny the cluster from other concurrent projects in need of it. An ethical dilemma associated with machine learning is the submission of decision-making to hidden processes (inherent to artificial neural networks) [82]. In this particular case, the predictions of the neural network inform the decisions of the active yaw control, but people are not directly affected by the employment of the neural network. Therefore, the use of the neural network is arguably ethically neutral.